Научном већу Института за физику

Београд, 11. октобар 2018. год.

Предмет: реизбор у звање истраживач-сарадник

Молба

       Молим да ми се одобри покретање реизбора у звање истраживач сарадник због неискоришћеног права на мировање звања током породиљског одсуствовања и ради добијања додатног времена потребног за завршавање доктората.

У прилогу достављам:

- мишљење руководиоца пројекта
- биографију
- списак научних радова
- фотокопије научних радова
- потврду о упису на докторске академске студије
- потврду о завршеним основним академским студијама
- преглед научне активности
- решење о претходном избору
- решење о породиљском одсуству и нези детета

у Београду,
11. октобра 2018. год.

Бојана Бокић

Мишљење руководиоца пројекта

Молим научно веће Института за физику

да покрене поступак за реизбор Бојане Бокић у звање истраживач сарадник. Бојана Бокић је уписана на Докторске академске студије на Физичком факултету, Универзитета у Београду, смер Квантна оптика и ласери. Учествовала је у изради пет радова у међународним часописима. Ангажована је на пројекту ОИ 171038 Министарства просвете, науке и технолошког развоја "Холографске методе генерисања специфичних таласних фронтова за ефикасну контролу квантних кохерентних ефеката у интеракцији атома и ласера", као и на билатералном са Немачком, под називом „Пропагација и локализација светлости у системима са комплексним фотоничним решеткама". Резултати које је постигла Бојана Бокић, показују да поседује неопходне способности за израду докторске дисертације, као и да се активно бави научно-истраживачким радом. Овим наведеним, мислим да задовољава све неопходне услове Министарства просвете, науке и технолошког развоја за реизбор у звање истраживач сарадник.

Предлог чланова комисије

За чланове комисије у поступку реизбора у звање истраживач сарадник предлажем:

1) др Дејан Пантелић, научни саветник Института за физику у Београду
2) др Бранислав Јеленковић, научни саветник Института за физику у Београду
3) др Сузана Петровић, виши научни сарадник Института за нуклеарне науке "Винча"

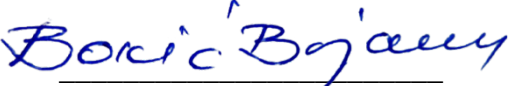<div align="right">

Руководилац пројекта

_____
Проф. др Дејан Пантелић

</div>

у Београду,
11.10.2018. год.

Биографија

Бојана Бокић је рођена у Београду 05.07.1981. године. У Неготину је завршила основну школу и гимназију, природно-математички смер. 2008. године дипломира (основне академске студије) на Електротехничком факултету, Универзитета у Београду, смер Наноелектроника, оптоелектроника и ласерска техника, са просечном оценом 7,94 и стиче звање дипломираног инжењера електротехнике. Дипломски рад је одбранила на тему *Примена ласера у медицини – Дијагностичке технике*. 2010. завршава Мастер академске студије на Електротехничком факултету, Универзитета у Београду, на студијском програму Дипломске академске студије Електротехника и рачунарство – модул Биомедицински и еколошки инжењеринг са просечном оценом 9,86 и радом на тему *Примена ласера и других снопних техника у дијагностичке и терапеутске сврхе у биомедицини*. Од 1. октобра 2010. је запослена у Центру за фотонику Института за физику, као истраживач-приправник, са ангажовањем на пројекту Министарства просвете, науке и технолошког развоја, под називом "Холографске методе генерисања специфичних таласних фронтова за ефикасну контролу квантних кохерентних ефеката у интеракцији атома и ласера" под руководством проф. др Дејана Пантелића. Од 2011. године је уписана на Докторске академске студије на Физичком факултету, Универзитета у Београду, смер Квантна оптика и ласери. 2013. и 2014. била је ангажована и на билатералном пројекту са Немачком под називом „Пропагација и локализација светлости у системима са комплексним фотоничним решеткама" под руководством проф. др Драгане Јовић Савић. Бојана Бокић је до сада публиковала пет радова у часописима категорије М21 и један у часопису М23 категорије.

у Београду,
11.10.2018. год.

_____
Бојана Бокић

Списак објављених радова

Рад у водећем међународном часопису (М21):

1. D. Pantelić, S. Ćurčić, S. Savić-Šević, A. Korać, A. Kovačević, B. Ćurčić, and **B. Bokić**, "High angular and spectral selectivity of purple emperor (Lepidoptera: *Apatura iris* and *A. ilia*) butterfly wings," Optics Express **19**, 5817 (2011)

2. Nemanja M. Lučić, **Bojana M. Bokić**, Dušan Ž. Grujić, Dejan V. Pantelić, Branislav M. Jelenković, Aleksandra Piper, Dragana M. Jović, Dejan V. Timotijević, „Defect-guided Airy beams in optically induced waveguide arrays", Physical Review A **88**, br. 6. (2013)

3. Falko Diebel, **Bojana M. Bokić**, Martin Boguslawski, Aleksandra Piper, Dejan V. Timotijević, Dragana M. Jović, Cornelia Denz, „Control of Airy-beam self-acceleration by photonic lattices", Physical Review A **90** br. 3 (2014)

4. Falko Diebel, **Bojana M. Bokić**, Dejan V. Timotijević, Dragana M. Jović Savić, Cornelia Denz, " Soliton formation by decelerating interacting Airy beams", Optics Express **23**, br. 19, str. 24351-24361. (2015)

5. Aleksander G. Kovačević, Suzana M. Petrović, **Bojana M. Bokić**, Biljana M. Gaković, Miloš T. Bokorov, Borislav Z. Vasić, Radoš B. Gajić, Milan S. Trtica, Branislav M. Jelenković, „Surface nanopatterning of Al/Ti multilayer thin films and Al single layer by a low-fluence UV femtosecond laser beam", Applied Surface Science **326**, str. 91-98 (2015)

Рад у међународном часопису (М23):

1. Monika M. Živković, Milesa Ž. Srećković, Tomislav M. Stojić, **Bojana M. Bokić**, „Influence of electromagnetic and nuclear radiation in medicine for therapy and diagnosis through processes, facts and statistical analysis", Nuclear Technology and Radiation Protection **32**, br.1, pp. 91-98. (2017)

Саопштење са међународног скупа штампано у целини (М33):

1. **Bojana M. Bokić**, Falko Diebel, Dejan V. Timotijević, Aleksandra Piper, Martin Boguslawski, Dragana M. Jović, Cornelia Denz, „Airy beams propagation in optically induced photonic lattices", *Nonlinear Optics And Its Applications VIII; And Quantum Optics III, vol. 9136 (SPIE)*, Brussels, Belgium, April 14-16, (2014).

Саопштење са међународног скупа штампано у изводу (М34):

1. M. Srećković, Ž. Tomić, Z. Fidanovski, S. Ostojić, P. Jovanić, Lj. Vulićević, A. Bugarinović, and **B. Bokić**, "The correlation between the initial ceramic particles and final products", *1st Conference of the Serbian Ceramic Society*, Belgrade, Serbia, March 17-18. (2011)

2. Nemanja M. Lučić, **Bojana M. Bokić**, Dušan Ž. Grujić, Dejan V. Pantelić, Branislav M. Jelenković, Darko M. Vasiljević, Dejan V. Timotijević, Aleksandra Piper, Dragana M. Jović, „Defect controlled Airy beam acceleration in optically induced waveguide arrays", *PHOTONICA 2013*, *IV international School and Conference on Photonics*, Beograd, Srbija, Avgust 26-30. (2013)

3. Nemanja M. Lučić, **Bojana M. Bokić**, Dušan Ž. Grujić, Dejan V. Pantelić, Branislav M. Jelenković, Aleksandra Piper, Dragana M. Jović, Dejan V. Timotijević, „Guiding of Airy Beams with Optically Induced Waveguide Arrays in the Nonlinear Crystal", *16th International Conference On Transparent Optical Networks (ICTON)*, Graz, Austria, July 06-10. (2014)

4. Nemanja M. Lučić, **Bojana M. Bokić**, Dušan Z. Grujić, Dejan V. Pantelić, Branislav M. Jelenković, Aleksandra Piper, Dragana M. Jović, Dejan V. Timotijević, „Airy beam propagation along one dimensional optically induced photonic lattice with defect ", Oasis 5th Conference and Exhibition on Optics and Electro-Optics, MEDINANO, pp. 74-74, Izrael, March 03-04. (2015)

Саопштење са скупа националног значаја штампано у изводу (М64):

1. M. Srećković, S. Polić-Radovanović, B. Timotijević, M. Timotijević, N. Borna, M. Živković, M. Dukić, and **B. Bokić**, "Laseri, palimpsest i kulturna baština," Fotonika 2010, Institut za fiziku (Beograd), 21-23. aprila 2010.

2. S. Polić-Radovanović, M. Srećković, B. Timotijević, M. Timotijević, V. Rajković, R. Radovanović, and **B. Bokić**, "The role of microscopy in the evaluation of the authenticity of the material of cultural heritage," *4th Serbian Congress for Microscopy*, Belgrade, Serbia, October 11-12. (2010)

3. **B. Bokić**, "Interakcija femtosekundnog laserskog impulsa sa materijalom - holografski pristup," Četvrta radionica fotonike (2011), Kopaonik, 2-6. marta 2011.

High angular and spectral selectivity of purple emperor (Lepidoptera: *Apatura iris* and *A. ilia*) butterfly wings

Dejan Pantelić,[1,*] Srećko Ćurčić,[2] Svetlana Savić-Šević,[1] Aleksandra Korać,[2, 3] Aleksander Kovačević,[1] Božidar Ćurčić[2] and Bojana Bokić[1]

[1]*Institute of Physics, University of Belgrade, Pregrevica 118, 11080 Zemun, Serbia*
[2]*Institute of Zoology, Faculty of Biology, University of Belgrade, Studentski Trg 16, 11000 Belgrade, Serbia*
[3]*Center for Electron Microscopy, Faculty of Biology, University of Belgrade, Studentski Trg 16, 11000 Belgrade, Serbia*
*pantelic@ipb.ac.rs

Abstract: The iridescent features of the butterfly species *Apatura iris* (Linnaeus, 1758) and *A. ilia* (Denis & Schiffermüller, 1775) were studied. We recognized the structural color of scales only on the dorsal side of both the fore and hind wings of males of both of the aforementioned butterfly species. The scale dimensions and microstructure were analyzed by a scanning electron microscope (SEM) and transmission electron microscope (TEM). The optical properties were measured and it was found that the peak reflectivity is around 380 nm, with a spectral width (full width at half maximum) of approximately 50 nm in both species. The angular selectivity is high and a purple iridescent color is observed within the angular range of only 18 degrees in both species.

©2011 Optical Society of America

OCIS codes: (050.2770) Gratings; (050.52980) Photonic crystals; (050.6624) Subwavelength structures; (160.4760) Optical properties.

References and links

1. M. Srinivasarao, "Nano-optics in the biological world: beetles, butterflies, birds, and moths," Chem. Rev. **99**(7), 1935–1962 (1999).
2. P. Vukusic, J. R. Sambles, C. R. Lawrence, and R. J. Wootton, "Quantified interference and diffraction in single *Morpho* butterfly scales," Proc. Biol. Sci. **266**(1427), 1403–1411 (1999).
3. P. Vukusic, and J. R. Sambles, "Photonic structures in biology," Nature **424**(6950), 852–855 (2003).
4. R. O. Prum, T. Quinn, and R. H. Torres, "Anatomically diverse butterfly scales all produce structural colours by coherent scattering," J. Exp. Biol. **209**(4), 748–765 (2006).
5. P. Vukusic, "Structural colour in Lepidoptera," Curr. Biol. **16**(16), R621–R623 (2006).
6. N. L. Garrett, P. Vukusic, F. Ogrin, E. Sirotkin, C. P. Winlove, and J. Moger, "Spectroscopy on the wing: naturally inspired SERS substrates for biochemical analysis," J Biophotonics **2**(3), 157–166 (2009).
7. M. D. Shawkey, N. I. Morehouse, and P. Vukusic, "A protean palette: colour materials and mixing in birds and butterflies," J. R. Soc. Interface **6**(Suppl 2), S221–S231 (2009).
8. H. Ghiradella, "Light and color on the wing: structural colors in butterflies and moths," Appl. Opt. **30**(24), 3492–3500 (1991).
9. H. Ghiradella, "Hairs, bristles, and scales," in *Microscopic Anatomy of Invertebrates, Vol. 11A: Insecta*, F.W. Harrison and M. Locke eds. (Wiley, New York, 1988).
10. H. Ghiradella, D. Aneshansley, T. Eisner, R. E. Silberglied, and H. E. Hinton, "Ultraviolet reflection of a male butterfly: interference color caused by thin-layer elaboration of wing scales," Science **178**(4066), 1214–1217 (1972).
11. L. P. Biró, K. Kertész, Z. Vértesy, G. I. Márk, Z. Bálint, V. Lousse, and J.-P. Vigneron, "Living photonic crystals: butterfly scales – nanostructure and optical properties," Mater. Sci. Eng. C **27**(5-8), 941–946 (2007).
12. Z. Han, L. Wu, Z. Qiu, and L. Ren, "Microstructure and structural color in wing scales of butterfly *Thaumantis diores*," Chin. Sci. Bull. **54**(4), 535–540 (2009).
13. M. Imafuku, Y. Hirose, and T. Takeuchi, "Wing colors of *Chrysozephyrus* butterflies (Lepidoptera; Lycaenidae): ultraviolet reflection by males," Zoolog. Sci. **19**(2), 175–183 (2002).
14. P. Vukusic, J. R. Sambles, and C. R. Lawrence, "Structurally assisted blackness in butterfly scales," Proc. Biol. Sci. **271**(Suppl 4), S237–S239 (2004).
15. P. Vukusic, and I. Hooper, "Directionally controlled fluorescence emission in butterflies," Science **310**(5751), 1151 (2005).

16. S. M. Luke, P. Vukusic, and B. Hallam, "Measuring and modelling optical scattering and the colour quality of white pierid butterfly scales," Opt. Express **17**(17), 14729–14743 (2009).
17. K. Kertész, G. Molnár, Z. Vértesy, A. A. Koós, Z. E. Horváth, G. I. Márk, L. Tapasztó, Z. Bálint, I. Tamáska, O. Deparis, J. P. Vigneron, and L. P. Biró, "Photonic band gap materials in butterfly scales: a possible source of "blueprints"," Mater. Sci. Eng. B **149**(3), 259–265 (2008).
18. Z. Vértesy, K. Kertész, Z. Bálint, G. Molnár, M. Erős, and L. P. Biró, "SEM and TEM investigations in the scales of the European nymphalid butterfly *Apatura ilia* dark and light phenotypes," in *BioPhot Meeting Abstract Book*, Levente Tapasztó ed. (Reserach Institute for Technical Physics and Materials Science, Budapest, Hungary, 2007*)*, pp. 14–15.
19. Z. Han, L. Wu, Z. Qiu, H. Guan, and L. Ren, "Structural colour in butterfly *Apatura ilia* scales and the microstructure simulation of photonic crystal," J. Bionics Eng. **5**(Supplement 1), 14–19 (2008).
20. R. E. Silberglied, "Visual communication and sexual selection among butterflies," In *The Biology of Butterflies. Symposium of the Royal Society of London, No. 11*, R. I. Vane-Wright, and P. E. Ackery eds. (Academic Press, London. 1984) pp. 207–223.
21. R. J. C. Page, "Perching and patrolling continuum at favoured hilltop sites on a ridge: a mate location strategy by the Purple Emperor butterfly *Apatura iris*," The Entomologist's Record **122**, 61–70 (2010).
22. S. Berthier, "Photonique des Morphos," (Springer-Verlag France, Paris, 2010).
23. G. A. Blackburn, "Hyperspectral remote sensing of plant pigments," J. Exp. Bot. **58**(4), 855–867 (2006).
24. M. A. Giraldo, S. Yoshioka, and D. G. Stavenga, "Far field scattering pattern of differently structured butterfly scales," J. Comp. Physiol. A Neuroethol. Sens. Neural Behav. Physiol. **194**(3), 201–207 (2008).
25. S. Yoshioka, and S. Kinoshita, "Wavelength-selective and anisotropic light-diffusing scale on the wing of the Morpho butterfly," Proc. Biol. Sci. **271**(1539), 581–587 (2004).

1. Introduction

The diurnal active members of the order Lepidoptera (butterflies) are considered to be the most attractive insects, together with representatives of the order Coleoptera (beetles). The delicate beauty of butterfly wings is a consequence of several phenomena: selective absorption by pigments, scattering, fluorescence and iridescence. The phenomenon of bright iridescence attracted much attention [1–7] and is observed in a great number of butterfly species, mostly tropical ones. Butterflies are known as the masters of mimicry (the type of camouflage which serves to avoid predators) and aposemy (warning coloration which is usually associated with an unpleasant taste to potential predators). In some species sexual dimorphism is observed, as in the two species analyzed in this paper.

Structural coloration investigations have been very popular in the last few decades and butterfly microstructure has been thoroughly investigated [8–10]. The following aspects have been studied as well: nanostructure and optical properties of wing scales [1, 11, 12], interference and diffraction in butterflies [2], ultraviolet reflection [13], structural blackness and whiteness in butterfly scales [14], fluorescence emission [15], and coherent scattering-induced structural color of scales [4]. The optical properties of butterfly scales have been thoroughly measured and modeled [16] and their nanoscale structures could encourage further developments in artificial material manufacturing [17].

The butterfly species *Apatura iris* (Linnaeus, 1758) and *A. ilia* (Denis & Schiffermüller, 1775) (Fig. 1a and b) are distributed from Europe to Eastern Asia (China). The most obvious difference between the two species is an extra eye spot on the fore wings of *A. ilia*. The males of *Apatura* spp. possess the iridescent color on the dorsal side of their wings [18, 19]. This is probably connected with intrasexual communication between males, rather than intersexual communication and attraction [20]. The structural color of males is visible in flight when the movements of the wings are noticeable within a certain range of angles. This kind of iridescent coloration represents an excellent contrast to forest canopy – a natural habitat of *Apatura* spp. Apart from structural coloration, pigment coloration is present as well.

The flight behavior of male *Apatura iris* was recently studied and it consisted mainly of perching and patrolling flights. The daily aggregation of males at favored landmark sites from approximately midday was observed as well [21].

Here we present a detailed study of two *Apatura* species with respect to their optical properties and the relationship of these properties to the microscopic structure of the wing scales.

Fig. 1. a) *Apatura iris*; b) *Apatura ilia*. Observe that *A. Ilia* has an extra eye spot on fore wings.

2. Materials and methods

2.1 Collecting data

Specimens of the species *Apatura iris* and *A. ilia* were used for optical investigations (Fig. 1). Both species were collected from the Balkan Peninsula: *A. iris* − Mt. Stara Planina, Southeastern Serbia (July 2009, leg. D. Stojanović), and *Apatura ilia* − Mt. Fruška Gora, Northern Serbia (July 2009, leg. D. Stojanović). The specimens were kept in the collection of the Institute of Zoology, Faculty of Biology, University of Belgrade, Serbia.

2.2 SEM procedure

The specimens of *Apatura iris* and *A. ilia* were rinsed with diethyl-ether to obtain a clear surface of the wings. The wings of the males were cut into rectangular shape (surface area of several mm^2). This was followed by dehydration in order to obtain dry samples, fixed on a test-bed and subsequently covered with gold. Prepared samples were analyzed by a scanning electron microscope (SEM) (JSM-6460LV, JEOL, Tokyo, Japan).

2.3 TEM procedure

Wings were cut into small pieces, fixed in 3% glutaraldehyde in 0.1M phosphate buffer (pH 7.2) and postfixed in 1% osmium tetroxide in the same buffer. The specimens were dehydrated with serial ethanol solutions of increasing concentration and embedded in Araldite (Fluka, Germany). For electron microscopic examination, the tissue blocks were trimmed and cut with diamond knives (Diatome, Switzerland) on an UC6 ultramicrotome (Leica, Austria). The thin sections were mounted on copper grids, stained with uranyl acetate and lead citrate (Ultrastain, Leica, Austria) and examined on a Philips CM 12 transmission electron microscope (TEM) (Eindhoven, the Netherlands) equipped with a Megaview III digital camera (Soft Imaging System, Münster, Germany).

2.4 Spectrometric measurements

A HR2000CG-UV-NIR Fiber spectrometer was used (Ocean Optics Inc., Dunedin, USA) to collect the reflection spectra of the investigated butterflies. Wing samples were positioned on a computer-controlled rotation platform and illuminated with a tungsten halogen lamp. Thus, we were able to record the reflection spectrum of the wings as a function of the angle of incidence. A MIRA titanium-sapphire laser with frequency doubler (Coherent Inc., USA) was used to investigate the spectral dependence of the wing scattering pattern in the blue and UV part of the spectrum. A diode-pumped Nd-YAG laser at 532 nm and diode laser at 630 nm were used as well. The wings were irradiated with a laser beam and the scattered radiation was photographed on the cylindrical screen by Canon EOS 50D camera. Rigorous coupled-wave analysis was used to calculate the spectral reflectivity.

3. Results

As in all butterfly species, the scales are positioned like roof tiles covering the entire dorsal and ventral sides of the wing (Fig. 2a). We recognized two types of scales on the dorsal side of both the fore and hind wings of *Apatura iris* and *A. ilia*. The cover scales are on top, while ground scales are situated below. We found that the cover scales are responsible for the blue iridescence of these two butterfly species (Fig. 2b) due to their much denser microscopic structure in comparison to the ground scales. We have found that iridescent scales are pigmented (see brownish scales in lower half of Fig. 2c).

a)

b)

c)
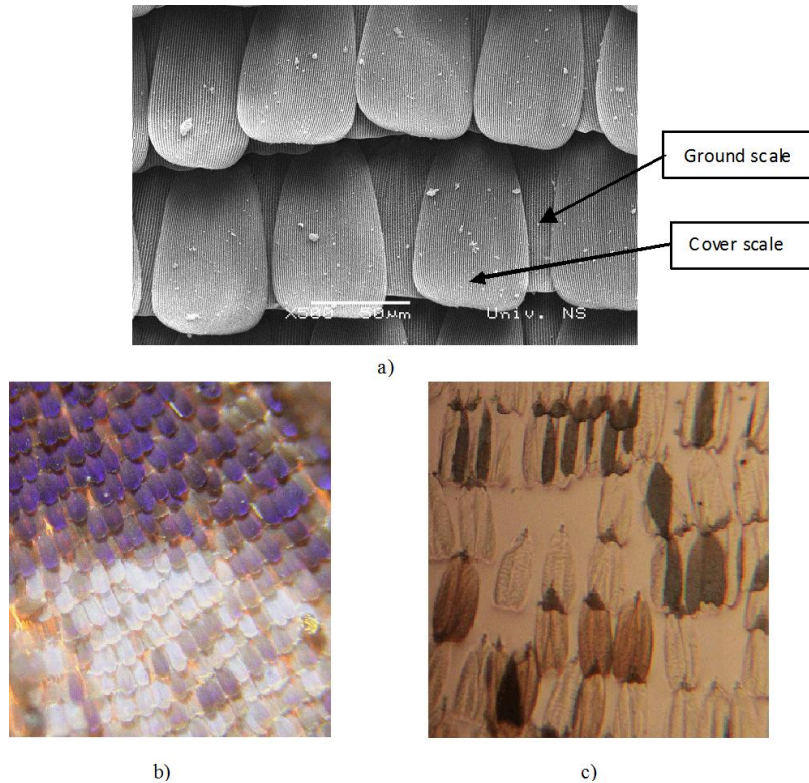
Fig. 2. *Apatura iris*: a) the cover scales on the dorsal wing side have a much denser structure in comparison to ground scales (SEM image); b) the blue iridescence of the cover scales positioned in regular rows. White scattering scales can be seen as well. The photograph is recorded in reflection; c) scattering scales have a glass-like appearance, while the iridescent scales are pigmented. Overlapping areas of glass-like scales are dark, indicating that the scattering is intensified. Microscope image is recorded in transmission.

The white areas of the dorsal wing side are also interesting. Examination of the reflective property revealed that the scales uniformly scatter light (Fig. 2b), while in transmission they look completely transparent (Fig. 2c). Scale overlapping increases the scattering, which can be seen as dark areas in upper half of Fig. 2c. We have found that there is a cumulative effect of overlapping. A single scale transmits around 90% and we measured the transmission of the overlapping scales to be about 60%.

By magnifying the iridescent butterfly scale surface of *Apatura iris* we observed long parallel ridges, each having a number of lamellas positioned one over another (see Fig. 3 for SEM images in two different views). The rows are mutually connected with orthogonally positioned cross ribs. TEM images were used to obtain the exact morphological and dimensional characteristics of each ridge and its lamellae (Fig. 4). The lamellae in cross section exhibit a multilayer structure, conifer-like, with six pairs of lateral projections which

are not widened distally and are triangularly pointed. The scale structure of *Apatura ilia* is similar, except that the ridge density is slightly higher.
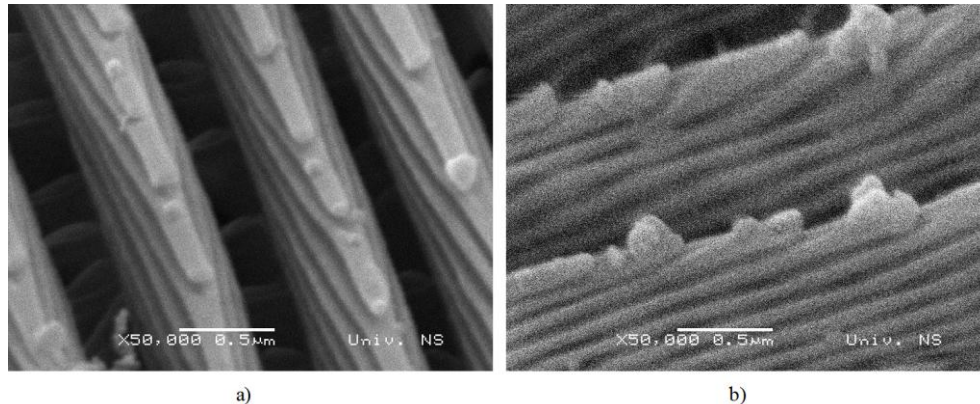

Fig. 3. SEM of the highly-magnified structure of a) *Apatura iris* cover scale in dorsal view; b) *A. iris* cover scale in dorso-lateral view. A stacked lamellar structure is apparent.

Fig. 4. TEM image of cover scale cross section of *Apatura iris*.

Electron microscope images were used to construct a geometrical model of the structure which was further utilized for theoretical analysis of the optical properties. Characteristic dimensions can be seen in Fig. 5. Ridges form a surface relief diffraction grating, with an 820 nm period and approximately the same depth (830 nm). On the other hand, the lamellae form a volume Bragg grating, with a roughly 75 nm period, with each lamella being 40 nm thick.

Butterfly wings were studied spectroscopically in relation to the illumination and observation angles. Several spectra were recorded for different angular orientations (Fig. 6a). Maximum reflectivity is observed in the UV part of the spectrum (380 nm) and does not depend on the observation angle. Spectral width is small (50 nm FWHM) compared with more visually spectacular species, such as *Morpho* butterflies [22]. There is a slight spectral shift (in the order of 10-20 nm) as a function of the angle of illumination. All of this apparently provides an evolutionary advantage when the butterfly reflectivity spectra (with UV maximum) are compared with the canopy spectra (with almost no reflectivity in UV region, a peak at 550 nm, and a plateau in the IR region) [23]. UV reflectivity makes the butterfly very visible to its own species and considerably less visible to all other animals, especially potential predators. The intensity of reflected light at visible and IR wavelengths is much lower, making the butterfly appear dull brown from almost all directions – an excellent camouflage in forest, where *Apatura* species is living.
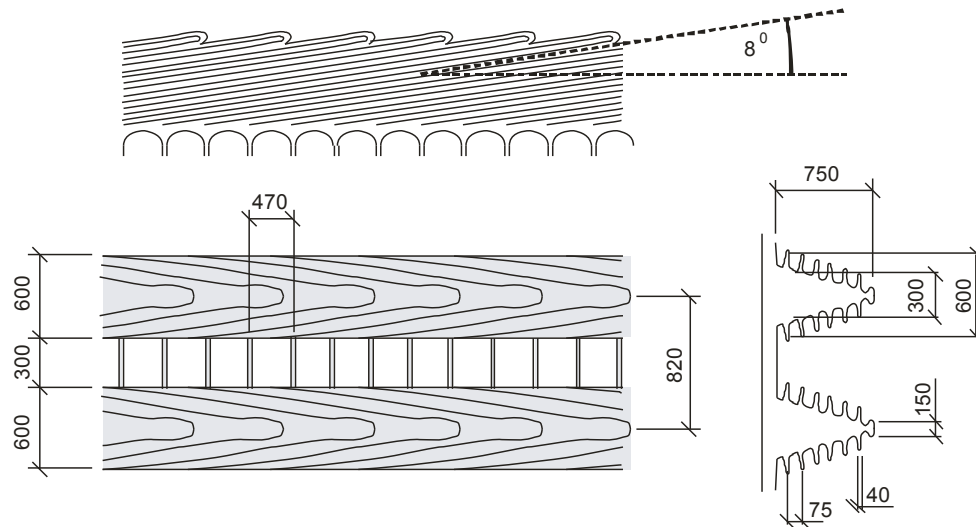
Fig. 5. Geometry of the microscopic structure of the *Apatura iris* wing scale (three orthogonal projections of the upper scale surface). All dimensions are in nanometers.

The iridescence of *Apatura iris* is observed in a rather narrow angular range (18 degrees); this is much narrower compared to other butterfly species [24]. Iridescence at 380 nm as a function of the angle of incidence is shown in Fig. 6b. Nearly identical spectral properties were observed in *Apatura ilia*.
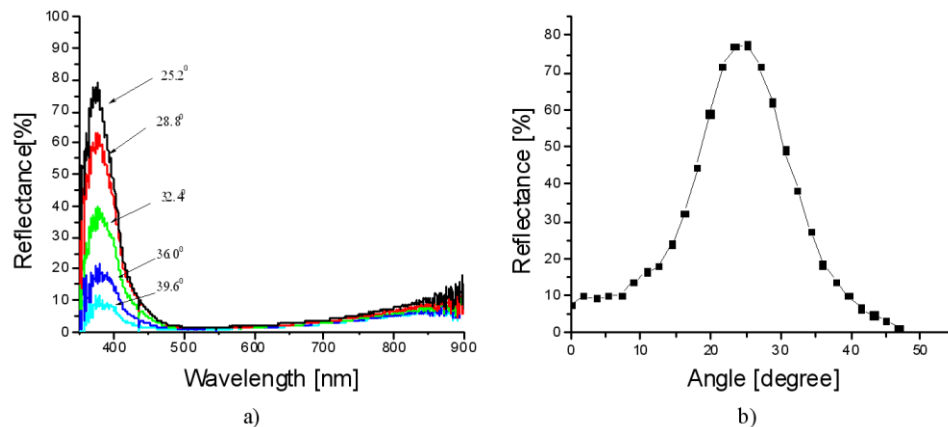

a)   b)

Fig. 6. a) Reflection spectra of the *Apatura iris* wing, with the angle of incidence as a parameter; b) iridescence at 380 nm as a function of the observation angle.

In order to observe the spatial distribution of iridescent light, we irradiated the butterfly wing with a laser beam from a tunable Ti-Sapphire laser coupled to frequency doubler. We were able to continuously tune the laser wavelength from 365 to 450 nm. A simple experimental setup is shown in Fig. 7a and 7b, and the typical spatial distribution of iridescence can be seen in Fig. 7c. It should be emphasized that the images were recorded by virtue of the natural fluorescence of the paper screen. In order to obtain an improved spatial distribution we applied pseudo-coloring of the recorded images.
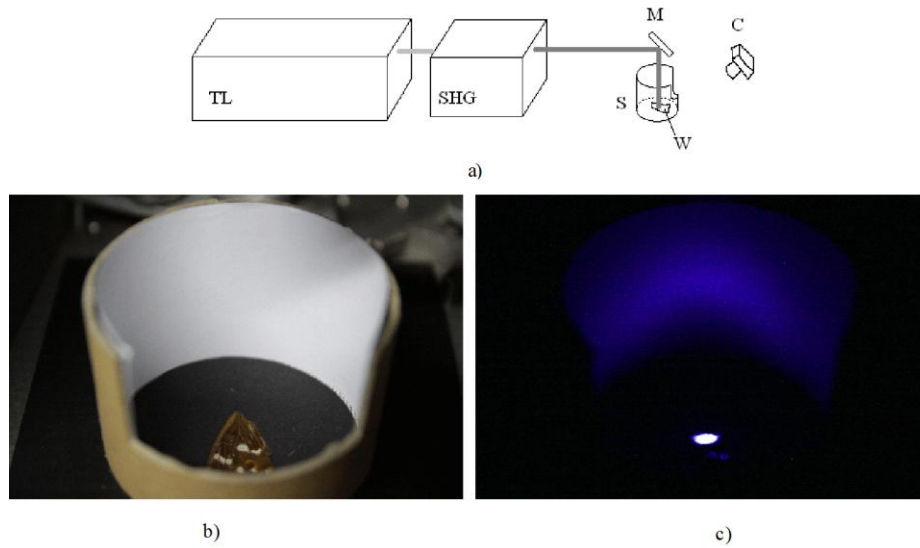
Fig. 7. a) Experimental setup used for the detection of the spatial distribution of *Apatura iris* wing iridescence (TL – titanium sapphire laser, SHG – frequency doubler, C – CCD camera, S – reflective cylinder, W – butterfly wing, M – mirror); b) a butterfly wing inside a reflective cylinder c) typical pattern of iridescence.
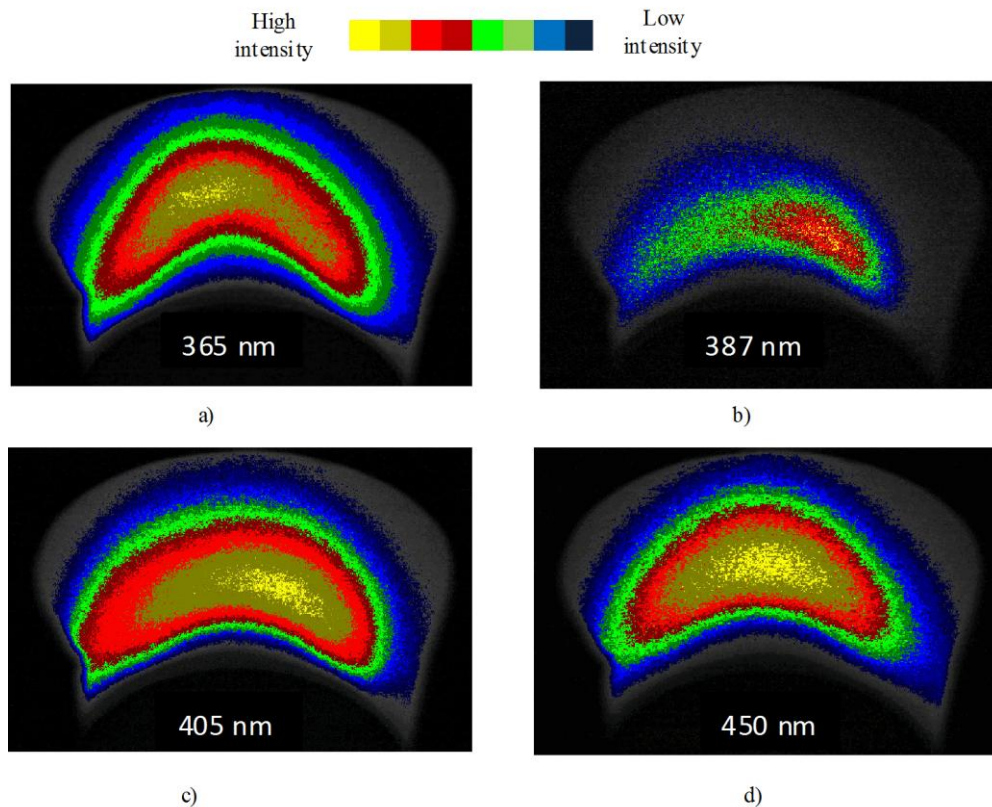

Fig. 8. Pseudo-colored images of iridescence recorded at: a) 365 nm; b) 387 nm; c) 405 nm; d) 450 nm. Patterns were recorded using a Ti-sapphire laser with frequency doubler. Light intensities are color coded according to the bar at the top of the figure.

Four images recorded at 365, 387, 405 and 450 nm are shown in Figs. 8a-8d. In comparison to other wavelengths, the spatial distribution at 387 nm is much narrower, indicating that at this particular wavelength the radiation is very directional. At 532 nm the directionality of scattered radiation is almost completely lost, as can be seen in Fig. 9, which was recorded by a diode-pumped Nd-YAG laser at 532 nm.
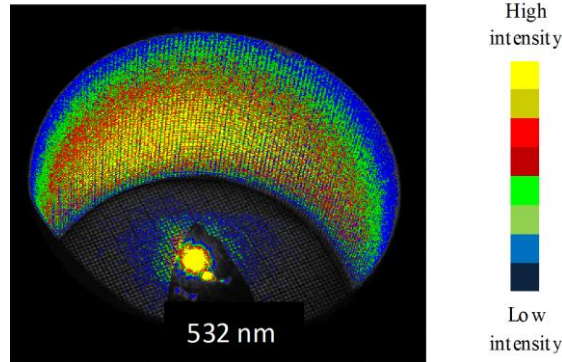

Fig. 9. Radiation at 532 nm is almost uniformly scattered at the wing of *Apatura iris*. The pattern was recorded by Nd-YAG laser. Light intensities are color coded – yellow representing the highest intensity, and blue the lowest.

4. Discussion

The results presented in this study show that the iridescence of *Apatura* spp. butterflies is spectrally and directionally constrained. With respect to the butterfly body, the radiation is directed as shown in Fig. 10 in three orthogonal projections. This particular feature is a consequence of the mutual orientations of lamellae with respect to the scale, and the scale with respect to the wing membrane (Fig. 11). There is a critical angle of incidence ($\gamma + 2\alpha + 2\beta = \pi/2$) when the radiation is Bragg-reflected along the wing surface. At a greater angle, the radiation cannot be further reflected (i.e., it is directed inside the material). In the case of *Apatura* butterflies, the angle α of the scale is large (~20°), as can be verified by the strong shadow cast by each scale in Figs. 2a and 2b.
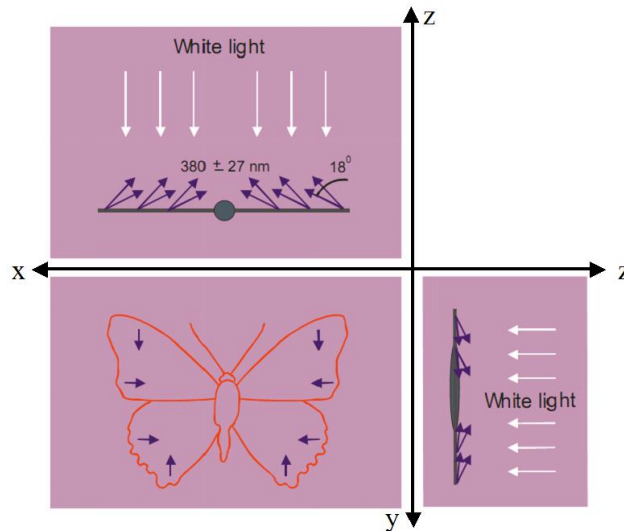

Fig. 10. Directions in which the blue iridescence can be observed (purple arrows). The butterfly is schematically presented in three orthogonal projections.
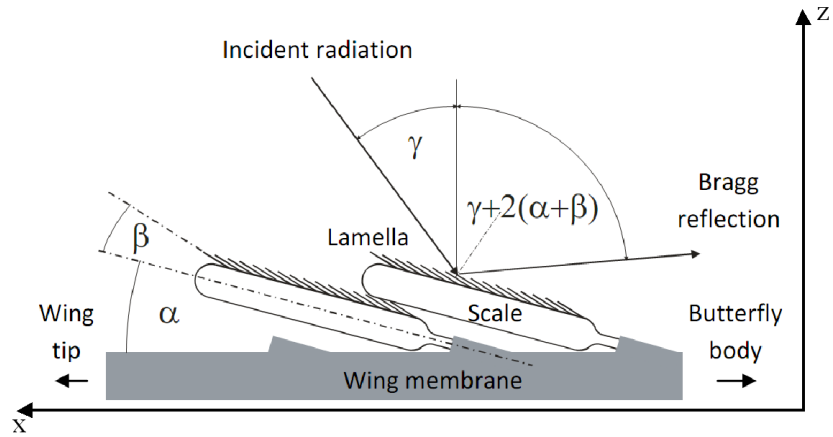
Fig. 11. Directionality of *Apatura* butterfly wing iridescence is a consequence of inclination of both lamellae (angle β) and the scale as a whole (angle α). γ is the angle of incidence of light with respect to the wing membrane. Axes x and z are in agreement with Fig. 10.
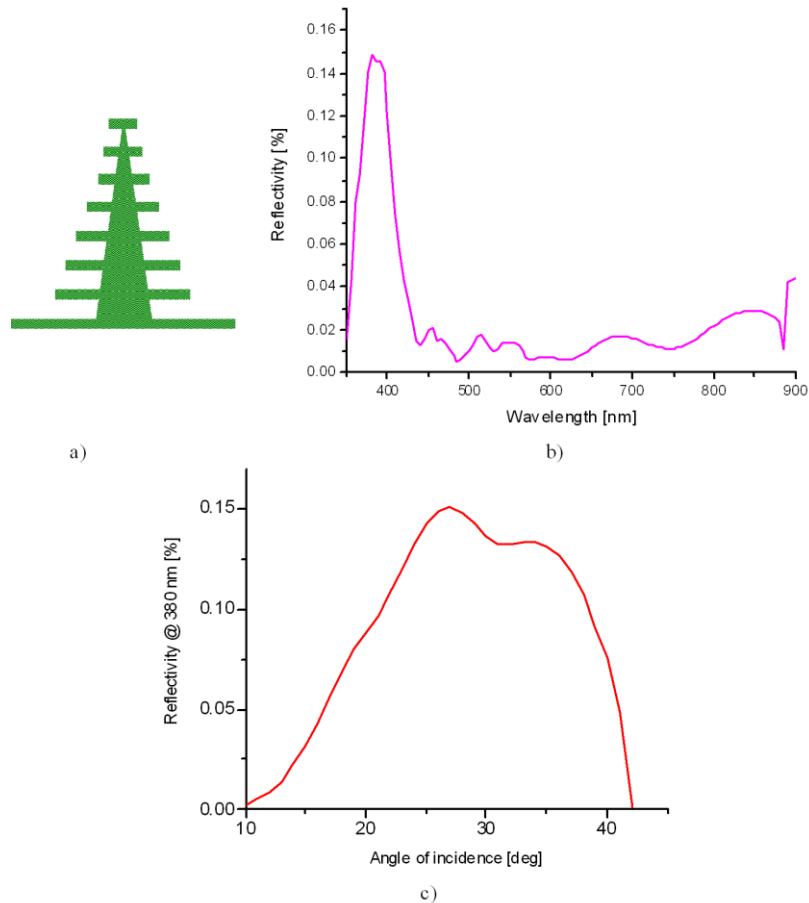

Fig. 12. a) Geometry of the butterfly cover scale in cross section, used for the calculation of the spectral reflectivity of *Apatura* spp.; b) spectral reflectivity as obtained by exact analysis using rigorous coupled-wave analysis; c) angular dependence of iridescence at 380 nm.

The spectral selectivity of the *Apatura* spp. scale was analyzed using rigorous coupled-wave analysis using simplified geometry as shown in Fig. 12a. We were able to correctly reproduce the spectral reflectivity (as shown in Fig. 12b) using dimensions presented in Fig. 5 and the refractive index of 1.56 for chitin [25]. Angular dependence of iridescence was calculated too and presented in Fig. 12c. Theoretical results slightly depart from experimental data, but this is due to idealized nature of calculation. In reality the butterfly grating is stochastically distorted, and the effect is averaged among many scales, inside illuminated wing area.

This phenomenon is in contrast with the reflection of *Morpho* butterfly wings, which direct radiation sideways and in a broad angular range. Also, the spectral maximum of iridescence shifts significantly with the angle of observation [22]. The difference between *Morpho* spp. and *Apatura* spp. is due to the different orientations of butterfly scales with respect to wing membrane. In *Morpho* butterflies the scales are almost parallel to the membrane (for example, *Morpho aega*), while in the *Apatura* species the scales are strongly inclined. On the nanoscopic level, ridges on the *Apatura* scale are not as dense as in *Morpho* butterflies. Even though the number of lamellas is almost the same in *Morpho helenor* [22] and *Apatura*, their cross sectional profile (as seen in TEM) is quite different. All these factors lead to radically different optical properties - *Apatura* iridescence is spectrally very pure, and the angular pattern is narrow.

5. Conclusions

Apatura ilia and *Apatura iris* are visually quite similar. *Apatura ilia* males have an iridescent purple color on the wings that dorsally arise from a fully ordered 3D structure, and a yellowish-brown color produced by pigments on the wings ventrally. On the other hand the males of *A. iris* have the same purple iridescent color on the dorsal side of the wings and a brownish color on the ventral side.

The photonic-type nanostructures consisting of chitin, occurring in the butterfly wing scales of the male individuals of the species *Apatura iris* and *A. ilia*, were investigated by both scanning and transmission electron microscopy and reflectance spectroscopy. A tunable laser was used to analyze the variation of spatial distribution of iridescence.

As in all butterfly species, the architecture of the scales is complex. They possess numerous alternating air and cuticle layers responsible for iridescence. From an optical point of view, both analyzed species behave similarly. Maximum reflectivity is observed in the UV region of the spectrum for both species and depends to a certain extent on the observation angle. We have found that the scale iridescence is remarkably narrow, both spectrally and angularly, in the studied butterfly species. This is the consequence of the interplay between scale structure and inclination with respect to the wing membrane. Iridescence is observed in a rather narrow angular range (18 degrees for both analyzed *Apatura* species while it is much greater in other butterfly species previously studied). The spectral width of the iridescence is small (around 50 nm FWHM for both analyzed *Apatura* species and is much greater in tropical *Morpho* butterflies).

Defect-guided Airy beams in optically induced waveguide arrays

N. M. Lučić,[1,2] B. M. Bokić,[2] D. Ž. Grujić,[2] D. V. Pantelić,[2] B. M. Jelenković,[2] A. Piper,[2] D. M. Jović,[2] and D. V. Timotijević[2]

[1]*Faculty of Electrical Engineering, University of Belgrade, 73 Bulevar kralja Aleksandra, 11120 Belgrade, Serbia*
[2]*Institute of Physics, University of Belgrade, P.O. Box 68, 11001 Belgrade, Serbia*

We demonstrate both theoretically and experimentally that a finite Airy beam changes its trajectory and shape in optically induced waveguide arrays consisting of different kinds of defects. The propagation dynamics and beam acceleration are controlled with positive and negative defects, and appropriate refractive index change. An additional class of discrete beams and Airy defect modes are demonstrated.

I. INTRODUCTION

Self-accelerating Airy beams were first demonstrated in quantum mechanics [1] as a dispersion-free solution of the Schrödinger equation. By means of an important link between quantum mechanics and paraxial wave optics, Airy beams have been recently transferred into an optical field [2,3]. They remain invariant along parabolic trajectories and attract a great deal of interest because of their unique properties, including transverse acceleration [4,5], nondiffraction [6,7], and self-reconstruction [8,9]. Such features make these beams useful for applications ranging from guiding and manipulation of microparticles [5] and producing curved plasma channels [10] to dynamically routing surface plasmon polaritons [11,12] and frequency generation [13].

One reason for interest in these beams is their potential application in nonlinear optics regimes: nonlinear interaction of light with some material and a study of accelerating beam dynamics inside nonlinear media. The behavior of Airy beams propagating from a nonlinear medium to a linear medium was studied in Ref. [14]. Formation of self-trapped accelerating optical beams is demonstrated with different self-focusing nonlinearities [15], ranging from Kerr and saturable to quadratic [16,17], and also with an optically induced refractive-index gradient [18]. Recent experimental realization of electron Airy beams [19] opens a novel ways of manipulating Airy beams with various magnetic or electric potentials. Although nondiffracting beams are not stationary solutions of the Schrödinger equation with introduction of uniform waveguide arrays, their modified counterparts are shown to exist and remain nondiffracting [20]. Similarly asymptotic preservation of a free accelerating property is observed [21] with Airy beam introduced in uniform waveguide arrays. This gave us motivation to study the impact of defects in waveguide arrays on uniform waveguide array counterparts of Airy beams.

In this paper, we investigate and analyze both theoretically and experimentally the active control of self-accelerating Airy beams with an optically induced waveguide array consisting of different kinds of defects. Various laser-written waveguide arrays are produced in Fe:LiNbO$_3$ crystal, with periodic refractive index change and appropriate defect guides. We consider how the positive and negative defects [22] influence the beam self-bending as well as reduction of the beam acceleration. In general, we find that with a modification of the refractive index change, Airy beam acceleration can be reduced to the discrete beams. However, close to the defect guides, the beam

dynamics changes completely: the beams experience a strong repulsion from the negative defect, while in the presence of the positive defect they form simple localized waves.

II. EXPERIMENTAL REALIZATION AND THEORETICAL MODELING OF AIRY BEAM PROPAGATION IN WAVEGUIDE ARRAYS

We use an iron-doped (0.05%) Fe:LiNbO$_3$ crystal with $0.5 \times 3 \times 10$ mm^3 dimensions. Waveguides are fabricated using the laser-writing system at a laser wavelength of 473 nm, which induces an appropriate structure change in the material [see the schematic diagram in Fig. 1(a)]. By moving the sample with respect to the perpendicular laser beam, a continuous modification of the refractive index is obtained enabling light guiding. The beam is focused by the $50\times$ microscope objective with a numerical aperture (NA) of 0.55. Our sample has waveguides of approximately 10 μm width, with spacing between the centers of the adjacent waveguides of $d = 20$ μm. We fabricate various one-dimensional waveguiding systems with a refractive index change of $\Delta n \sim 1 \times 10^{-4}$, while two of the guides are fabricated with either a lower (negative defect) or higher refractive index change (positive defect), achieved by a variation of the writing velocity. Experimental setup for the investigation of Airy beam propagation in such waveguide arrays is shown in Fig. 1(b). For the creation of the Airy beam, an initial Gaussian beam from a 532 nm laser is projected through a cubic phase mask onto a spatial light modulator (SLM). The beam is then Fourier transformed and the 8 μW input Airy beam, roughly 10 μm wide in the main lobe, is launched to the front face of the crystal. The output intensity pattern, appearing at the end face of the crystal, is real time observed by means of a charge-coupled-device (CCD) camera. The intensity pattern evolution along the propagation direction (z axis) through the crystal is obtained with another CCD camera mounted above the sample, parallel to the x-z crystal plane. The camera records scattered light from the crystal, with the integration time of about 2 min.

To theoretically model Airy beam propagation in a waveguide array, along the propagation distance z, we consider the nonlinear Schrödinger equation

$$i\frac{\partial E}{\partial z} = -\frac{1}{2}\frac{\partial^2 E}{\partial x^2} - V(x)E, \tag{1}$$

where E is a slowly varying envelope, $V(x) = n_s - \Delta n \cos^2(\pi x/d)$ is the periodic refractive-index profile of the
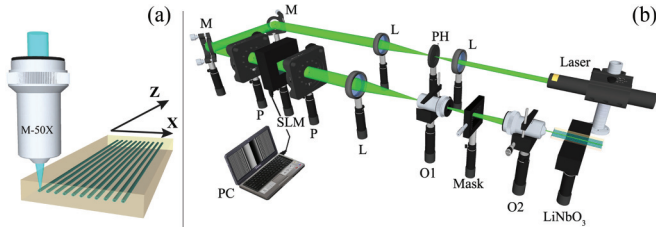
FIG. 1. (Color online) Experimental setup for an investigation of Airy beam propagation effects in waveguide arrays. (a) Scheme of the laser-writing waveguide arrays process in LiNbO$_3$ crystal. (b) Schematic of the experimental setup. Light from a 532 nm laser is expanded and phase modulated by a spatial light modulator (SLM). The beam is Fourier transformed and input into an LiNbO$_3$ crystal, and imaged into a CCD camera. L-lens, PH- pinhole, M-mirror, O-objective, PC-computer.

array with the lattice period d, n_s is a bulk material refractive index, and Δn is the optically induced refractive index change.

We investigate the propagation dynamics of Airy beams in optically induced waveguide arrays, with emphasis on the competition between the acceleration and self-bending propagation properties of Airy beams, and the trend of waveguide arrays to form discrete wave filaments. The propagation characteristics of Airy beams in waveguide arrays with and without defects are considered both theoretically and experimentally. We compare our experimental results to numerical simulations, carried out by the split-step Fourier method with the parameters of our experiment. All theoretical results are confirmed experimentally. First, to compare appropriate effects we test the Airy beam propagation in our crystal with no waveguide arrays fabricated. There is a typical Airy beam bending with a transverse displacement at the output, with no diffraction evident in the main lobe, observed both experimentally [Figs. 2(a) and 2(b)] and theoretically Fig. 2(c), after 10 mm of propagation.

Next, keeping all conditions unchanged, the Airy beam is launched in the waveguide arrays fabricated in our crystal, with the main lobe positioned in one waveguide (an incident waveguide). When refractive index change is optically induced, the Airy beam, which remains self-similar during propagation and has a ballistic trajectory, can interact with the neighboring waveguides. One can see that the bending of the main lobe of the Airy beam is weaker [Figs. 2(d)–2(f)], in comparison with the uniform case [Figs. 2(a)–2(c)]. Also, the presence of the waveguide arrays leads to a creating beam that propagates similar to the discrete waves. With appropriate refractive index change the output position of the Airy beam moves downward, indicating suppressed acceleration of the Airy beam, and it forms the various kinds of discrete structures. A series of numerical investigations are also performed to manipulate Airy beam acceleration with different refractive index change (see Sec. IV, Figs. 4 and 5).

III. DEFECT-CONTROLLED AIRY BEAM ACCELERATION

We also study the influence of various defect guides on the Airy beam propagation, and active control and manipulation of the beam acceleration with such defects. We show that the balance between self-acceleration properties and defect plays an important role in the evolution of the Airy beam. Our results are shown in Fig. 3, obtained with the same Airy beam as before, but using two different classes of waveguide arrays: containing a single defect with a lower refractive index defect guide (negative defect) and with a higher refractive index defect guide (positive defect). In both cases the main Airy lobe is positioned into the defect guides, at the input. First, we consider waveguide arrays with negative defects and observe strong beam repulsion from such defects [Figs. 3(a)–3(c)]. But, shifting the main lobe position to the waveguide close to the defect channel, one can observe a typical discrete surface waves (not shown). However, the Airy beam propagation is drastically changed in the presence of a positive defect guide so the formation of simple localized waves is possible with appropriate positive defects [Figs. 3(d)–3(f)].
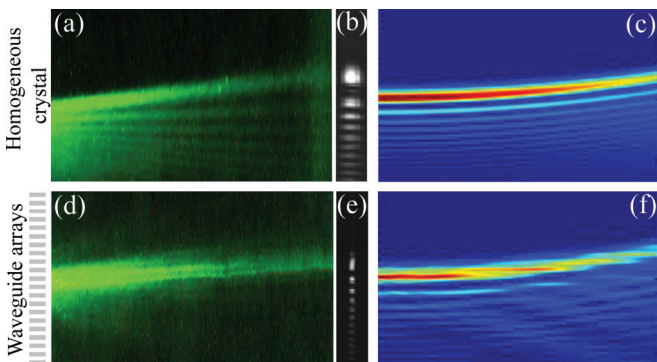

FIG. 2. (Color online) Airy beam propagation in homogeneous LiNbO$_3$ crystal (top row) and waveguide arrays optically induced in the same crystal (bottom row). Intensity plots of Airy beam structures in longitudinal direction during the propagation: (a), (d) experiment; (c), (f) theory. (b), (e) Corresponding intensity distributions at the back face of the crystal. Physical parameters: the crystal length $L = 10$ mm, lattice constant $d = 20$ μm, width of the main Airy lobe 10 μm.
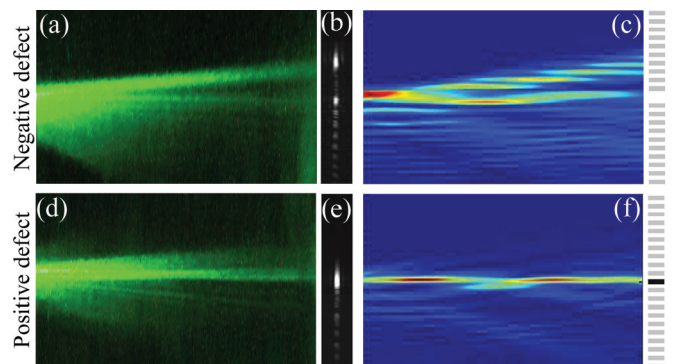
FIG. 3. (Color online) Airy beam propagation in waveguide arrays with negative (top row) and positive (bottom row) defects. Intensity plots of Airy beam structures in longitudinal direction during the propagation: (a), (d) experiment; (c), (f) theory. (b), (e) Corresponding intensity distributions at the back face of the crystal. Defect refractive index change is 0 for negative and 2Δn for positive defect. Other parameters are as in Fig. 1.
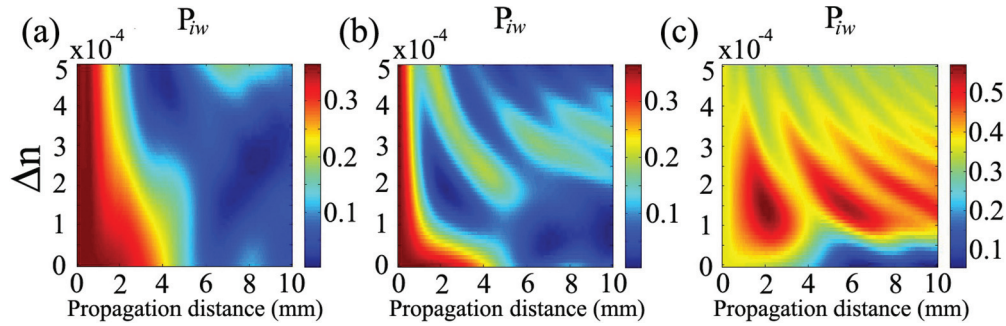
FIG. 4. (Color online) Dependence of the percentage of the Airy beam power in the incident waveguide (P_{iw}) on refractive index change Δn and propagation distance for (a) waveguide array, (b) negative defect, and (c) positive defect. Physical parameters are as in Fig. 3.

IV. DEPENDENCE OF AIRY BEAM PROPAGATION ON THE REFRACTIVE INDEX CHANGE

Finally, we study numerically the dynamics of Airy beam propagation in waveguide arrays with various refractive index changes Δn. Again, we compare three cases with positive and negative defects and with no defects. We show that beams exhibit shape-preserving acceleration inside a low refractive index change, but discrete diffraction and formation of various discrete beams occur with an increasing refractive index change, and very rich beam dynamics and amplitude modulations are seen with further increasing of Δn. We monitor a percentage of the Airy beam power in incident waveguide (P_{iw}), as the ratio between the power of the beam in the incident waveguide (or defect channel in the case with defect waveguides) and the total power of the Airy beam,

FIG. 5. (Color online) Airy beam propagation dynamics in different waveguide arrays. Typical intensity distributions of Airy beam structures in longitudinal direction during the propagation for waveguide arrays with (a), (d) no defects; (b), (e) negative defect; and (c), (f) positive defect. (a)–(c) $\Delta n = 3 \times 10^{-4}$; (d)–(f) $\Delta n = 5 \times 10^{-4}$. (g) Airy beam power in incident waveguide (P_{iw}) at the crystal exit as a function of refractive index change Δn. A vertical dotted line shows experimental refractive index change. Physical parameters are as in Fig. 4.

at appropriate propagation distance. A dependence of P_{iw} on the refractive index change Δn and propagation distance is presented in Fig. 4 for all three cases: (a) waveguide array, (b) negative defect, and (c) positive defect. Figure 4 clearly demonstrates the impact of waveguide arrays on the formation of discrete beams [Fig. 4(a)]. Also, it demonstrates the impact of the defect inclusion on the acceleration beams, the shape-preserving nature of these beams, and the refractive index change caused with the defect inclusion [Figs. 4(b) and 4(c)]. One can see that discrete beam diffraction is more visible in the case of waveguide arrays without defects. However, an energy localization in the incident waveguide is more pronounced in the waveguide arrays with the negative defect [Fig. 4(b)], and the most with the positive defect [Fig. 4(c)].

Figure 5 presents some typical examples of the Airy beam propagation along the longitudinal direction for Δn higher than in our experimental sample. Intensity distributions for two values of refractive index change are shown: $\Delta n = 3 \times 10^{-4}$ (first row) and $\Delta n = 5 \times 10^{-4}$ (second row) for waveguide arrays [Figs. 5(a) and 5(d)], negative defects [Figs. 5(b) and 5(e)], and positive defects [Figs. 5(c) and 5(f)]. In the case without defects, discrete beam formation starts at shorter propagation distance while the refractive index change is increased. With the negative defect guide, increasing Δn, amplitude modulations take place, and they are more pronounced with higher Δn. The beam repulsion from defect guide is also visible. At last, inclusion of a positive defect leads to a more localized energy in the defect guide, but also with some kind of amplitude modulations for higher refractive index change. We monitor Airy beam power in the incident waveguide (P_{iw}) at the crystal exit as a function of refractive index change Δn [Fig. 5(g)]. For waveguide arrays with no defects, P_{iw} after 10 mm propagation distance is slightly changed, decreases with lower, but increases with higher Δn. In the case of a negative defect, P_{iw} has maximal values at $\Delta n \sim 3 \times 10^{-4}$. The percentage of the Airy beam power in incident waveguide is higher for positive defect guides, and for parameters we used in our investigation it has maximum at $\Delta n \sim 1.3 \times 10^{-4}$. Also, we investigate defect guides with different refractive index change, as well as different defect size (not shown). Our analysis provides a very good tool for manipulation and controlling of Airy beam acceleration and self-ending properties, as well as appropriate conditions for the formation of discrete, surface or localized waves produced using Airy beams.
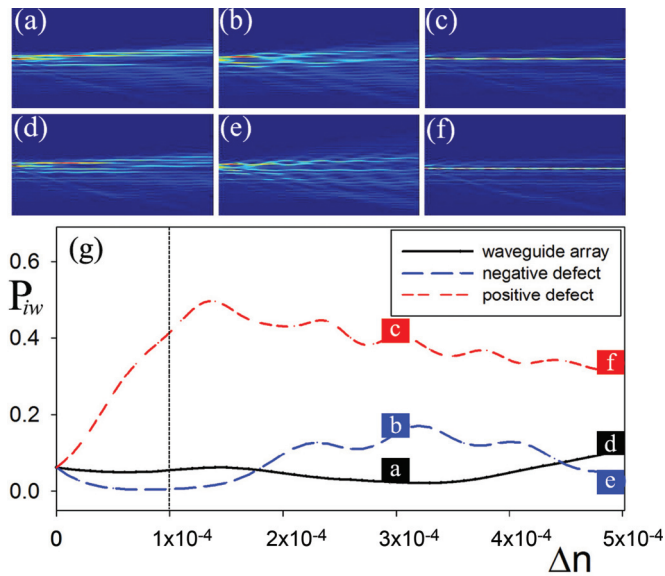
V. CONCLUSIONS

In summary, we have demonstrated the propagation dynamics of Airy beams in optically induced waveguide arrays. We have analyzed experimentally and numerically how various waveguides modify acceleration and self-bending properties of such beams, resulting in the discrete beams or Airy defect mode formation. We have demonstrated that the presence of various defect types, their sizes, as well as the refractive index change could drastically change the initial Airy beam shape. The experimental results fully agree with the theoretical analysis. A similar method can be used for control of other accelerating beams, such as parabolic beams. While we performed all our analysis in one-dimensional waveguide arrays, all our findings should also hold in two-dimensional photonic lattices.

[1] M. Berry and N. Balazs, Am. J. Phys. **47**, 264 (1979).

[2] G. A. Siviloglou and D. N. Christodoulides, Opt. Lett. **32**, 979 (2007).

[3] G. A. Siviloglou, J. Broky, A. Dogariu, and D. N. Christodoulides, Phys. Rev. Lett. **99**, 213901 (2007).

[4] G. A. Siviloglou, J. Broky, A. Dogariu, and D. N. Christodoulides, Opt. Lett. **33**, 207 (2008).

[5] J. Baumgartl, M. Mazilu, and K. Dholakia, Nat. Photon. **2**, 675 (2008).

[6] I. M. Besieris and A. M. Shaarawi, Opt. Lett. **32**, 2447 (2007).

[7] A. V. Novitsky and D. V. Novitsky, Opt. Lett. **34**, 3430 (2009).

[8] J. Broky, G. A. Siviloglou, A. Dogariu, and D. N. Christodoulides, Opt. Express **16**, 12880 (2008).

[9] H. I. Sztul and R. R. Alfano, Opt. Express **16**, 9411 (2008).

[10] P. Polynkin, M. Kolesik, J. V. Moloney, G. A. Siviloglou, and D. N. Christodoulides, Science **324**, 229 (2009).

[11] P. Zhang, S. Wang, Y. Liu, X. Yin, C. Lu, Z. Chen, and X. Zhang, Opt. Lett. **36**, 3191 (2011).

[12] A. Minovich, A. E. Klein, N. Janunts, T. Pertsch, D. N. Neshev, and Y. S. Kivshar, Phys. Rev. Lett. **107**, 116802 (2011).

[13] T. Ellenbogen, N. Voloch-Bloch, A. Ganany-Padowicz, and A. Arie, Nat. Photon. **3**, 395 (2009).

[14] Y. Hu, S. Huang, P. Zhang, C. Lou, J. Xu, and Z. Chen, Opt. Lett. **35**, 3952 (2010).

[15] I. Kaminer, M. Segev, and D. N. Christodoulides, Phys. Rev. Lett. **106**, 213903 (2011).

[16] A. Lotti, D. Faccio, A. Couairon, D. G. Papazoglou, P. Panagiotopoulos, D. Abdollahpour, and S. Tzortzakis, Phys. Rev. A **84**, 021807(R) (2011).

[17] I. Dolev, I. Kaminer, A. Shapira, M. Segev, and A. Arie, Phys. Rev. Lett. **108**, 113903 (2012).

[18] Z. Ye, S. Liu, C. Lou, P. Zhang, Y. Hu, D. Song, J. Zhao, and Z. Chen, Opt. Lett. **36**, 3230 (2011).

[19] N. Voloch-Bloch, Y. Lereah, Y. Lilach, A. Gover, and A. Arie, Nature **494**, 331 (2013).

[20] O. Manela, M. Segev, and D. N. Christodoulides, Opt. Lett. **30**, 2611 (2005).

[21] R. El-Ganainy, K. G. Makris, M. A. Miri, D. N. Christodoulides, and Z. Chen, Phys. Rev. A **84**, 023842 (2011).

[22] F. Fedele, J. Yang, and Z. Chen, Opt. Lett. **30**, 1506 (2005).

Control of Airy-beam self-acceleration by photonic lattices

Falko Diebel,[1,*] Bojana M. Bokić,[2] Martin Boguslawski,[1] Aleksandra Piper,[2] Dejan V. Timotijević,[2] Dragana M. Jović,[2] and Cornelia Denz[1]

[1]*Institut für Angewandte Physik and Center for Nonlinear Science (CeNoS),*
Westfälische Wilhelms-Universität Münster, 48149 Münster, Germany
[2]*Institute of Physics, University of Belgrade, P.O. Box 68, 11001 Belgrade, Serbia*

We demonstrate control over the acceleration of two-dimensional Airy beams propagating in optically induced photonic lattices. Depending on the lattice strength, we observe a slowing-down and suppression of the self-acceleration of Airy beams, as well as a formation of discrete lattice beams. Moreover, we explore the effects of different artificial single-side defects on the propagation and acceleration. For positive defects, the localization of the Airy beam to the defect site is further enhanced, while for negative defects most of the power is repelled from this site.

I. INTRODUCTION

Since their discovery in 1979 by Berry and Balazs [1], the fascinating class of Airy beams has attracted huge interest in different fields of physics. Originally, Airy beams were introduced as wave functions, solving the one-dimensional Schrödinger equation for free particles. Their probability density remarkably stays nonspreading under time evolution, while being transversely accelerated to follow a parabolic trajectory. Due to the formal equivalence between the Schrödinger equation in quantum mechanics and the paraxial equation of diffraction in optics, the concepts and solutions can be transferred to optics, where Airy beams can be directly observed and explored in experiments.

The first realization of optical one- and two-dimensional Airy beams [2] initiated an active field of research, leading to a number of systematic investigations of the generation, the manipulation, and the general properties of Airy beams in linear and nonlinear regimes [3–8]. The unique nonspreading and self-accelerating features of Airy beams moreover led to a huge variety of applications, including so-called autofocusing beams [9], optical snowblowers [10], and optical routers [11]. Also the influence of inhomogeneous potentials and the presence of dielectric interfaces on the propagation of Airy beams have been studied in the past [8,12–17].

Controlling the propagation behavior of light with light itself is the key requirement to realize new all-optical guiding and switching architectures. It is well known that the presence of discrete photonic lattice structures dramatically changes the propagation dynamics of light. Thus, one promising approach towards this goal is to tailor the transverse acceleration of two-dimensional optical Airy beams using photonic lattices. Recently, defect guided Airy beams in optically induced one-dimensional waveguide arrays were observed [18]. Despite the fact that Airy beams have been subject to many research activities, the propagation of such accelerated beams inside a two-dimensional optically induced photonic lattice has only been studied numerically with an isotropic refractive index potential assumed [19].

In this paper, we investigate and analyze the propagation dynamics of self-accelerating Airy beams in two-dimensional photonic lattices including defects, both theoretically and experimentally. The lattices were fabricated by optical induction [20] in photorefractive strontium barium niobate and the refractive index modulations are numerically calculated in the anisotropic model [21]. We consider how the discrete lattice changes the shape of the Airy beam and influences its self-acceleration. The propagation dynamics and beam acceleration are controlled by varying the lattice strength. We find that increasing the refractive index modulation reduces the Airy beam acceleration and leads to the formation of discrete lattice beams. Additionally, we realize different defect lattices by embedding two types of single-site defects into the regular lattice and investigate the impact onto the Airy beam. The defects remarkably change the beam dynamics. For the negative defect the beams experience a strong repulsion, while in the presence of the positive defect they form strongly localized waves or defect modes.

II. THEORETICAL BACKGROUND AND EXPERIMENTAL SETUP

To study the propagation characteristics of Airy beams in an optical system with induced photonic lattices, we consider the scaled paraxial equation of diffraction for the electric field Ψ:

$$i\frac{\partial \Psi}{\partial \zeta} + \frac{1}{2}\left(\frac{\partial^2 \Psi}{\partial \chi^2} + \frac{\partial^2 \Psi}{\partial \nu^2}\right) + \frac{1}{2}k_0^2 w_0^2 \Delta n^2(I_{\text{indu}})\Psi = 0. \quad (1)$$

Here, $\chi = x/w_0$ and $\nu = y/w_0$ are the dimensionless transverse coordinates scaled by the characteristic length w_0. $\zeta = z/kw_0^2$ represents the dimensionless propagation distance with $k = 2\pi n/\lambda$. The photonic lattice enters this equation in terms of an intensity-dependent refractive index modulation $\Delta n^2(I_{\text{indu}})$, which is described by the full anisotropic model [21] and precisely models the optical induction process in an externally biased photorefractive crystal. Moreover, Eq. (1) is also suitable to cover nonlinear light propagation when the inducing intensity becomes a function of the field Ψ itself. In this contribution, however, we restrict ourselves to linear effects.

---

*Corresponding author: falko.diebel@uni-muenster.de

For the case of linear light propagation in homogenous media, where $\Delta n^2 = 0$, the wave equation (1) can always be separated into two parts, each depending only on one transverse coordinate, χ or ν, respectively. Consequently, also the solution Ψ separates and can be written as product in the following form: $\Psi(\chi, \nu, \zeta) = \psi(\chi, \zeta)\psi(\nu, \zeta)$, where ζ is the longitudinal coordinate. As first shown in Ref. [1], each part of the wave equation can be solved by a nondispersive one-dimensional Airy function Ai(X). Thus, the overall solution of Eq. (1) in two dimensions reads as

$$\Psi(\chi, \nu, \zeta) = \psi(\chi, \zeta)\psi(\nu, \zeta) \qquad (2)$$

with

$$\psi(X, \zeta) = \text{Ai}[X - (\zeta/2)^2]\exp[i(X\zeta/2) - i(\zeta^3/12)] \qquad (3)$$

and $X = \{\chi, \nu\}$.

The solution $\Psi(\chi, \nu, \zeta)$ describes a nonspreading, two-dimensional optical Airy beam which is transversely accelerated while propagating along the longitudinal coordinate ζ. At first glance, the acceleration of the wave packets in homogeneous media without any index gradient seems to contradict the Ehrenfest theorem, which states that the center of mass of a wave function moves with constant speed if there is no force acting. Since Ψ is not square integrable, the center of mass cannot be defined. This also implies that the wave function contains infinite energy and extends over the whole space, both being nonphysical [6,22].

We instead have to consider a truncated solution with finite extent and energy, written as $\psi(X, 0) = \text{Ai}[X]\exp[a_X X]$, with the positive decay length a_X, typically $a_X \ll 1$. It has been shown that this truncated solution still solves the wave equation (1) and that the distinguished properties of two-dimensional Airy beams are mostly preserved [23]. Although the truncated intensity pattern is now nonspreading only over a limited propagation distance, this easily covers the longitudinal range which is necessary to observe sufficient transverse displacement of the Airy beam.

The characteristics of a two-dimensional optical Airy beam propagating inside a homogeneous medium are shown experimentally in Fig. 1. The transverse intensity distributions of the Airy beam at the front and the back faces of the photorefractive crystal are shown in Figs. 1(b) and 1(c), respectively. In addition, the intensity profile is recorded for a huge set of transverse planes along the crystal to demonstrate the accelerated transverse shift of the Airy beam during propagation. A cross section through this three-dimensional intensity volume along one vertical axis is shown in Fig. 1(a). This picture reveals that the experimentally realized Airy beam follows the expected accelerated trajectory and it proves that the unavoidable truncation with $a_{\chi,\nu} \neq 0$ in the experiment only negligibly affects the beam propagation compared to the ideal case of infinite beams.

A. Optically induced photonic lattices

To experimentally realize the photonic lattices for controlling the acceleration of the Airy beam we use the technique of optical induction [20], which in the past has proved its flexibility to create various types of two- and three-dimensional photonic lattices [24–26]. Moreover, this approach provides a versatile platform to study different fundamental linear and nonlinear propagation effects, such as Anderson localization [27] or discrete lattice and vortex solitons [28,29].

The optical induction method relies on the property of photorefractive materials, e.g., strontium barium niobate (SBN), to locally change their refractive index according to the intensity distribution the crystal is illuminated with [30]. For this reason the resulting refractive index structure is directly linked to the intensity of the induction beam. In all experiments presented in this contribution we require two-dimensional photonic lattices, implying that the induction beam may be conveniently realized by choosing from the wide class of nondiffracting beams [31,32].

For the realization of photonic lattices with the optical induction technique, we use nondiffracting beams characterized by optical fields whose intensity distributions are modulated in the transverse plane and stay unchanged in the longitudinal dimension. Such beams share the property that in Fourier space all contributing field components lie on an infinitely small ring with radius k_t, defining the structure size of the transverse pattern in real space. In particular, we consider a photonic square lattice which would be constituted from superimposing four tilted plane waves. The electric field E_{ndB} then reads as

$$E_{\text{ndB}}(x, y, z) = \sum_{n=1}^{4} E_n e^{ik_t(x\cos\varphi_n + y\sin\varphi_n)}e^{ik_z z}, \qquad (4)$$

with $\varphi_n = \pi(2n+1)/4$ and $k^2 = k_t^2 + k_z^2$. To minimize the anisotropic response of the photorefractive effect, the induction beam is rotated by $45°$.

Figure 1(d) shows the recorded intensity distribution of the experimentally realized nondiffracting beam which is used to optically induce the two-dimensional square lattice. The lattice period $\Lambda = \pi/k_t \approx 25\,\mu\text{m}$ is chosen to exactly match the distance between the main and the next neighboring lobes of the Airy beam. To realize different lattice strengths Δn, we utilize that the optically induced refractive index modulation in SBN builds up with time. By illuminating the crystal with the writing beam intensity for different times we thus are able to control the depths of the index modulation. To verify that the appropriate photonic lattice is actually induced, we illuminate the front face of the crystal with a plane wave after the writing process was completed. The initially homogeneous intensity of the plane wave is redistributed by the imprinted refractive index modulation to be locally increased at regions of higher refractive index. Thus, by recording the intensity at the back face of the crystal we can visualize the written photonic structure [Fig. 1(e)] [24].

B. Experimental setup and numerical methods

All experiments were carried out using the experimental setup sketched in Fig. 1(f). The beam from a frequency-doubled, continuous wave Nd : YVO$_4$ laser emitting at a wavelength of $\lambda = 532$ nm is divided into two separate beams, each illuminating a high-resolution, programmable phase-only spatial light modulator (SLM). The first modulator (SLM1), in combination with the following two lenses and the Fourier mask, is employed to shape the nondiffracting induction beam. We address a specially calculated phase pattern to this SLM
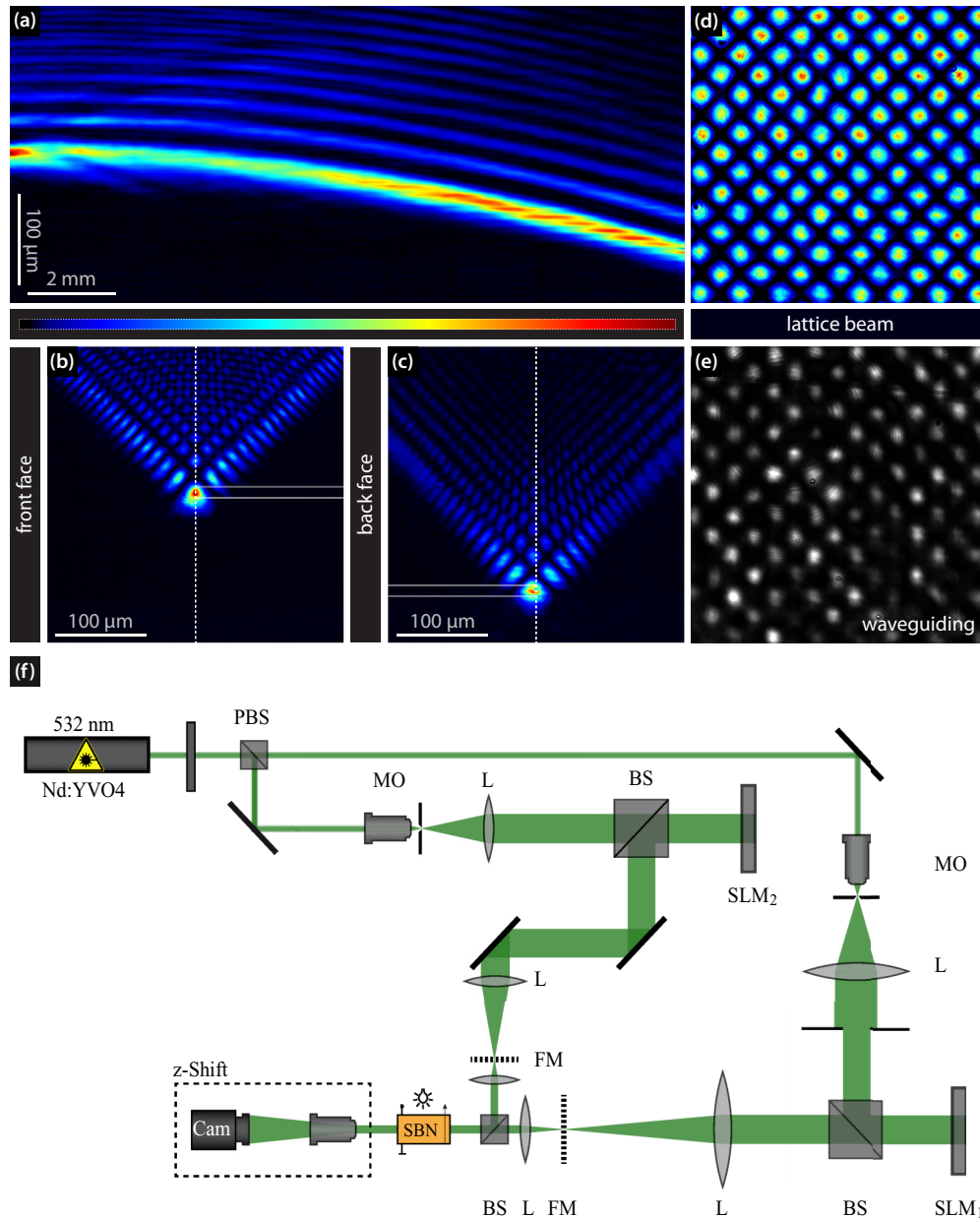
FIG. 1. (Color online) Experimental realization of two-dimensional Airy beams and photonic lattices. (a) Experimentally recorded profile during propagation, (b) intensity distribution of the Airy beam at the front face, and (c) intensity distribution at the back face. (d) Intensity pattern of the induction beam; (e) picture of the induced refractive index using wave guiding. (f) Experimental setup: (P)BS, (polarizing) beam splitter; FM, Fourier mask; L, lens; MO, microscope objective; SBN, strontium barium niobate crystal; and SLM, spatial light modulator.

which allows us to modulate the phase and the amplitude of the incident plane wave simultaneously [33]. Thereby, we obtain the complex field of the desired nondiffracting beam. Afterward, this modulated beam illuminates the 20-mm-long photorefractive $Sr_{0.60}Ba_{0.40}Nb_2O_6$ (SBN:Ce) crystal, which is externally biased with an electric dc field of $E_{ext} \approx 2000\,V/cm$ aligned along the optical c axis. To minimize the feedback of the written refractive index structure onto the induction beam itself, the induction beam is set to be ordinarily polarized with respect to the crystal's optical c axis. The high polarization anisotropy in the electro-optic coefficients of SBN:Ce [34], however, allows us to induce sufficient refractive index modulations to substantially affect the propagation of the

extraordinarily polarized Airy beam. The Airy beam is realized in the same manner by directly encoding the complex field calculated in real space with Eq. (2) onto the second modulator (SLM2). To accurately overlay the two beams in the crystal, a beam splitter is placed directly in front of the SBN crystal. In addition, by illuminating the crystal homogeneously with white light, we can erase written refractive index modulations. By means of an imaging lens and a camera mounted on a translation stage we can record the intensity distribution in different transverse planes.

We support our experiments with comprehensive numerical simulations by solving the paraxial wave equation (1), which models the light propagation in media with inhomogeneous
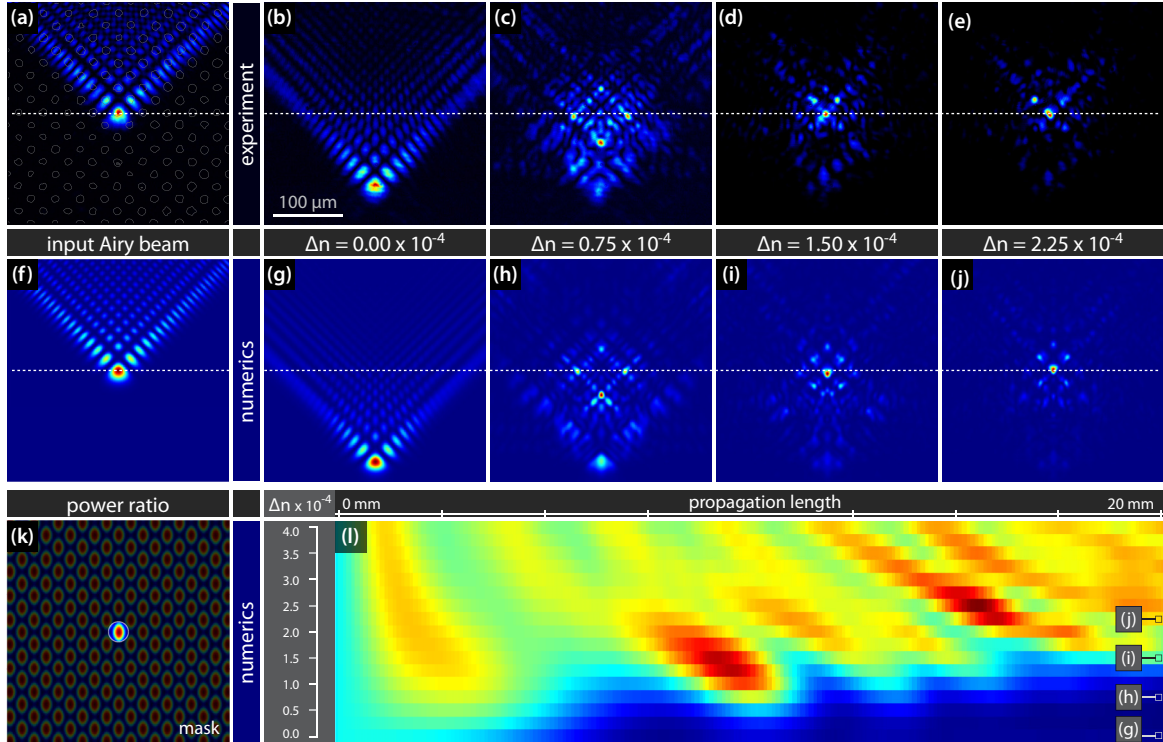
FIG. 2. (Color online) Airy beam propagation in a regular diamond lattice. (a), (f) Input Airy beams at the front crystal face in experiment and numerics [the layout of the lattice beam is indicated by open circles in panel (a)]. (b)–(e) Experimental recorded intensity distributions at the back face for different refractive index change Δn; (g)–(j) corresponding numerical results. (k) The shaded area represents the mask for the calculation of power ratio. (l) Dependance of the percentage of the Airy beam power in the incident waveguide on refractive index change Δn and propagation length z.

refractive index modulations. The resulting optically induced index modulation in the photorefractive material is represented by $\Delta n^2(I_{indu})$, which can be calculated in the full anisotropic model [21] with a relaxation method. Since only linear effects are considered, the inducing intensity I_{indu} is solely given by the intensity of the nondiffracting beam, $I_{indu} = |E_{ndB}|^2$ [cf. Eq. (4)]. Even though the paraxial wave equation stays in the linear regime, it is not solvable analytically and we need to rely on proven beam propagation methods. The propagation equation (1) is solved numerically, using a split-step Fourier method described earlier in Ref. [35,36].

III. TWO-DIMENSIONAL AIRY BEAMS IN PHOTONIC LATTICES

In this section, we investigate the influence of an optically induced photonic lattice onto the self-acceleration of two-dimensional optical Airy beams. We set our focus on the competition between the self-bending propagation of Airy beams and the waveguiding and discrete diffraction effects of the photonic lattice. Therefore, we successively increase the strength of the induced refractive index modulation and observe the effect on the beam acceleration. While increasing the lattice strength, the Airy beam more efficiently excites different linear Bloch modes of the lattice which hinders the acceleration during propagation of the undisturbed Airy beam. This results in an effectively slowed down acceleration, which for a certain value was effectively stopped completely.

Figure 2 summarizes our results with respect to the propagation of the Airy beam inside a regular photonic lattice. The top row [Figs. 2(a)–2(e)] contains our experimental results, while the corresponding numerical simulations are shown in the second row [Figs. 2(f)–2(j)]. The first two columns recap the typical transverse displacement of the Airy beam that propagated between the front face [Figs. 2(a) and 2(f)] and the back face [Figs. 2(b) and 2(g)] of the homogenous crystal. Now, the Airy beam is launched into the induced photonic lattice with the main lobe exactly located at one lattice site. As the refractive index modulation strength growths, the interaction of the Airy beam with the lattice sites becomes stronger and consequently the bending of the Airy beam is decreased. Our experimental results [Figs. 2(c)–2(e)], as well as our numerics [Figs. 2(h)–2(j)] clearly show the frustration of the self-acceleration of the Airy beam. Depending on the different lattice strengths, various kinds of discrete structures arise until the lattice finally suppresses the acceleration of the Airy beam completely. Most of the energy then stays in the lattice site, where the main lobe of the Airy beam was initially launched.

To get a more detailed insight into the propagation dynamics, we monitor the ratio between the power guided in the central waveguide and the total power of the Airy beam as a function of the lattice strength and the propagation distance. In Fig. 2(l) the numerical results for this power ratio are shown. With this reduced representation we are able to illustrate the key signature of the complex evolution of the Airy beam during the propagation for the different lattice strengths. It illustrates,

spatially resolved, how much energy is guided in the central lattice site and thus how strong the Airy beam acceleration is frustrated by the lattice. The shaded area in Fig. 2(k) represents the mask to calculate the power in the central waveguide. This graph clearly demonstrates the impact of optically induced photonic lattice on the formation of discrete structures, as well as suppression of the acceleration and bending of the Airy beam. For certain values of Δn one can see oscillations of the beam power in the central waveguide along the propagation distance. This is due to the self-bending property of Airy beams and the influence of the central waveguide not only on the main lobe but also on other lobes that overlap with this particular waveguide along the propagation. As a result, the part of their power is monitored in the central waveguide for some propagation distances. For higher refractive index modulations Δn, one can observe the localization of most of the beam power to central waveguide as the beam leaves the crystal. Again, to experimentally control the index modulation depth we take advantage of the time-dependent buildup of the induced lattice, which grows monotonously with the writing time.

In contrast to a corresponding situation of one-dimensional Airy beams propagating in a waveguide array [18], here the localization of the two-dimensional Airy beams at the output strongly depends on the strength of the photonic lattice, which also can be seen at the right edge of Fig. 2(l). This different behavior can be explained by the fact that in two dimensions each lattice site has four next neighbors (in the one-dimensional case only two). Thus, here the interaction of the Airy beam which is launched with its main lobe exactly placed at one lattice site is more pronounced.

This dependency of the beam localization on the lattice strength, for example, can be harnessed to realize a fast switch or router for Airy beams based on their polarization. The optical induction in SBN leads to an internal space charge field that modulates the refractive index via the linear electrooptic effect. Because of the strong polarization anisotropy of the electrooptic coefficients, $r_{13} \ll r_{33}$ [34], the lattice strength experienced by the Airy beam strongly depends on the polarization. Consequently, the shape as well as center of mass of the intensity distribution that leaves the photonic lattice can be controlled solely by changing the polarization of the incoming Airy beam.

We also study the transition of the Airy beam that leaves the SBN crystal with the inscribed photonic lattice to a linear medium (e.g., air) and its further propagation. It has been shown recently that only an Airy beam initially driven by a particular self-defocusing nonlinearity experiences anomalous diffraction and can maintain its shape over a long distance after exiting the nonlinear medium [37]. In our crystal with optically induced photonic lattice we could not observe that the exiting field pattern propagates robustly with the properties characteristic for Airy beams over a long distance after the crystal.

IV. AIRY BEAM PROPAGATION IN PHOTONIC LATTICE WITH DIFFERENT DEFECTS

Besides the influence of regular photonic lattices on the behavior of two-dimensional Airy beams, we investigate the propagation effects caused by defects embedded in these lattices. In particular, we consider two-dimensional

single-site defect lattices with positive or negative variable defect strengths.

To realize the different defect lattices, we use a well-localized zero-order nondiffracting Bessel beam to locally increase or decrease the refractive index modulation at one selected lattice site. It is important that the resulting defect lattice remains two-dimensional. Therefore, the lattice is induced by an effective intensity distribution resulting from an incoherent superposition of the discrete and the Bessel nondiffracting beam. This incoherent superposition is essential to get rid of the phase relation between both beams, which otherwise would lead to additional undesired intensity modulations due to interference. To avoid the coherent effects, we illuminate the crystal one after the other with the discrete and the Bessel beam, respectively. Thereby, we utilize the high dielectric response time of the SBN crystal for the used intensities that allows for switching frequencies in the order of seconds. As shown in the past, this multiplexing method is capable of fabricating a whole set of two-dimensional aperiodic structures, superlattices, and defect lattices [38–40]. In order to realize negative defects, the index modulation at one selected lattice site is decreased by switching to defocusing nonlinearity while the crystal is illuminated with the Bessel beam. This is achieved by applying the static electric field antiparallel to the optical c axis [40].

Figure 3 illustrates the basic scheme of the defect realization using multiplexed nondiffracting beams. The regular lattice is induced with the intensity distribution shown in Fig. 3(a). Simultaneously, the Bessel beam intensity shown in Fig. 3(b) increases or decreases the induced refractive index at one lattice site, depending on the direction of the applied electrical field. The resulting effective intensity distributions for the positive and negative defect lattices are shown in Figs. 3(c) and 3(d), respectively. Figures 3(e) and 3(f) show the numerically calculated refractive index modulations that result for both types of defect lattices.

Once the defect lattices are realized, we finally study how the different defects influence the Airy beam propagation and acceleration. We keep all parameters from the previous
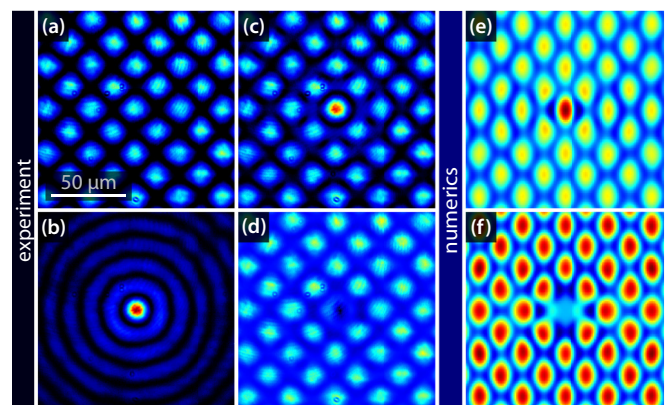

FIG. 3. (Color online) Defect generation in optically induced photonic lattice. (a) Experimental realization of the diamond lattice, (b) the Bessel beam, (c) the positive defect lattice, and (d) the negative defect lattice. Numerical realization of (e) positive and (f) negative lattice defects.
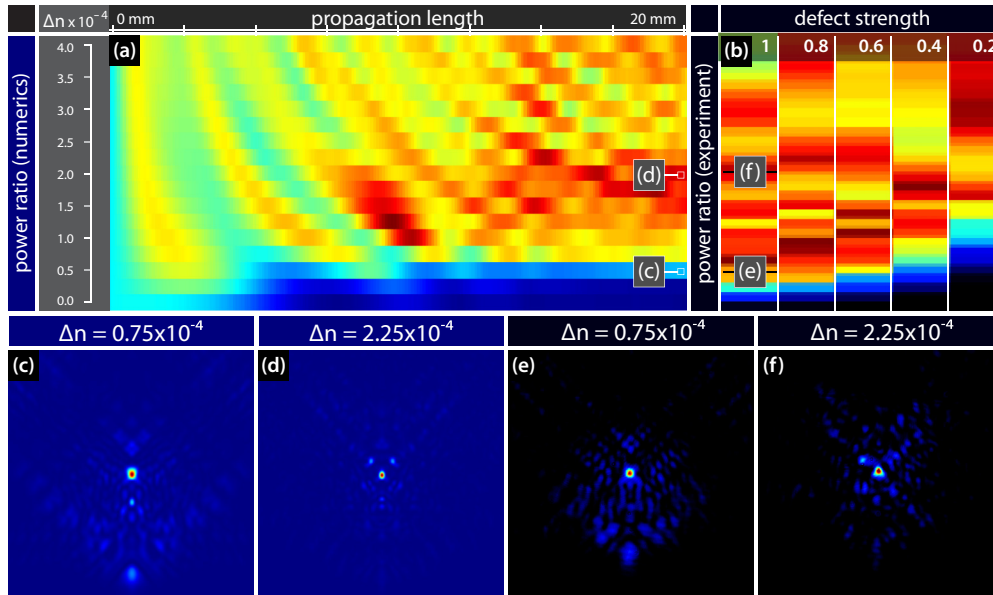
FIG. 4. (Color online) Airy beam propagation in different positive defect lattices. (a) Numerical results for the dependance of the Airy beam power propagating in defect site on refractive index change Δn and propagation length z. (b) Experimentally observed percentage of the Airy beam power propagating in the defect site as a function of the refractive index change Δn and defect strength S_d. (c), (d) Exemplary numerical results of Airy beam intensity distribution at the back crystal face. (e), (f) Experimentally recorded output intensity distributions. The letters in panels (a) and (b) indicate the corresponding intensity pictures.

experiments, but change the sign of the defect to both positive and negative. The Airy beam is positioned with its main lobe exactly located at the defect site. For the different defects, we record the intensity profiles of the propagated Airy beam at the back face of the crystal and monitor the percentage of the power guided in the central waveguide, as described previously.

In Figs. 4 and 5 we show our results for the positive and negative defects, respectively. The numerical results for the power ration as a function of the propagation distance ζ and the refractive index modulation Δn are presented as panels (a) in both figures. We picked two particular cases with $\Delta n = 0.75 \times 10^{-4}$ [panel (c)] and $\Delta n = 2.25 \times 10^{-4}$ [panel (d)] for representation and show the intensity profile at the back face
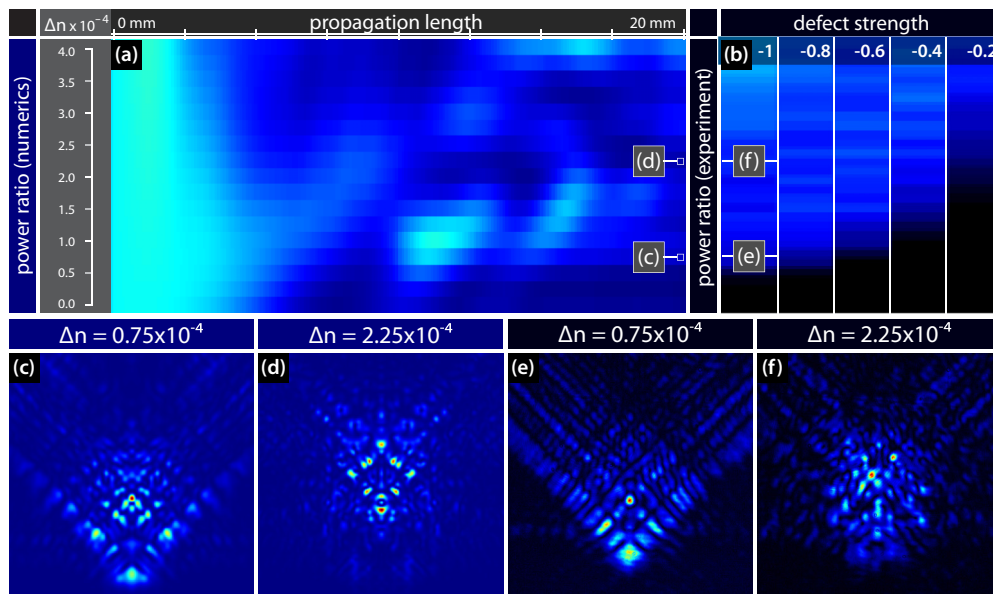
FIG. 5. (Color online) Airy beam propagation in different negative defect lattices. (a) Numerical results for the dependance of the Airy beam power propagating in defect site on refractive index change Δn and propagation length z. (b) Experimentally observed percentage of the Airy beam power propagating in the defect site as a function of the refractive index change Δn and defect strength S_d. (c), (d) Exemplary numerical results of Airy beam intensity distribution at the back crystal face. (e), (f) Experimentally recorded output intensity distributions. The letters in panels (a) and (b) indicate the corresponding intensity pictures.

of the crystal. The positions corresponding to these intensity profiles are indicated with the letters (c) and (d) in the power ratio plot (a).

Because in experiments it is not possible to record the intensity pattern inside an inhomogeneous crystal, we are restricted to the profiles at the back face. In Figs. 4(b) and 5(b) the experimentally measured power ratio at the back face is plotted as a function of the refractive index modulation and the defect strength. Therefore, we have repeated the experiments for five different defect strengths for both positive and negative defects and recorded the intensity profile at the back face. The modulus of the defect strength S_d is given by the ratio of the peak intensities of the discrete and the Bessel nondiffracting beam, while the sign is determined by the direction of the applied electric field. In the experiment, we also select the two representative lattice strengths Δn to show the intensity profile at the output of the crystal [panels (e) and (f)]. Again, their positions in the experimental power ratio plot (b) are indicated with the letters (e) and (f).

These results illustrate the strong dependence of the propagation and acceleration properties of the Airy beam on the lattice depths, as well as the defect strength. The positive defect [Fig. 4(a)] strongly enhances the localization of the Airy beam, while for the negative defect [Fig. 5(a)] the power guided in the defect site is significantly reduced and finally completely repelled. A similar behavior was reported earlier for one-dimensional Airy beams propagating in a waveguide array with defects [18], and it was predicted that it qualitatively agrees with the results in two dimensions.

V. CONCLUSION

In summary, we have demonstrated the control over the propagation dynamics of two-dimensional Airy beams in optically induced photonic lattices. We have shown, both theoretically and experimentally, that depending on the depths of the induced lattice, the acceleration and the bending of the Airy beam are strongly affected. For increasing refractive index contrast, different discrete patterns arise and for a certain value the acceleration of the beam is effectively stopped. Moreover, we demonstrated the influence of various single-side defects on the propagation dynamics of the Airy beam. The defect strength as well as the lattice depth dramatically change the initial Airy beam shape and its self-bending. For positive defects, the localization is remarkably increased, while for negative defects, the situation is changed to transport nearly no power along the defect site. All presented experimental results fully agree with the supporting numerical simulations. Our results can readily be generalized to other kinds of optically induced lattices and defect types, including more complex or even three-dimensional lattices. Also other classes of self-accelerated optical beams can be controlled using the presented ideas and methods.

[1] M. V. Berry and N. L. Balazs, Am. J. Phys. **47**, 264 (1979).

[2] G. A. Siviloglou, J. Broky, A. Dogariu, and D. N. Christodoulides, Phys. Rev. Lett. **99**, 213901 (2007).

[3] T. Ellenbogen, N. Voloch-Bloch, A. Ganany-Padowicz, and A. Arie, Nat. Photonics **3**, 395 (2009).

[4] D. Abdollahpour, S. Suntsov, D. G. Papazoglou, and S. Tzortzakis, Phys. Rev. Lett. **105**, 253901 (2010).

[5] A. Chong, W. H. Renninger, D. N. Christodoulides, and F. W. Wise, Nat. Photon. **4**, 103 (2010).

[6] G. A. Siviloglou, J. Broky, A. Dogariu, and D. N. Christodoulides, Opt. Lett. **33**, 207 (2008).

[7] Y. Hu, P. Zhang, C. Lou, S. Huang, J. Xu, and Z. Chen, Opt. Lett. **35**, 2260 (2010).

[8] W. Liu, D. N. Neshev, I. V. Shadrivov, A. E. Miroshnichenko, and Y. S. Kivshar, Opt. Lett. **36**, 1164 (2011).

[9] N. K. Efremidis and D. N. Christodoulides, Opt. Lett. **35**, 4045 (2010).

[10] J. Baumgartl, M. Mazilu, and K. Dholakia, Nat. Photon. **2**, 675 (2008).

[11] P. Rose, F. Diebel, M. Boguslawski, and C. Denz, Appl. Phys. Lett. **102**, 101101 (2013).

[12] N. K. Efremidis, Opt. Lett. **36**, 3006 (2011).

[13] Z. Ye, S. Liu, C. Lou, P. Zhang, Y. Hu, D. Song, J. Zhao, and Z. Chen, Opt. Lett. **36**, 3230 (2011).

[14] S. Chávez-Cerda, U. Ruiz, V. Arrizón, and H. M. Moya-Cessa, Opt. Express **19**, 16448 (2011).

[15] N. K. Efremidis and I. D. Chremmos, Opt. Lett. **37**, 1277 (2012).

[16] I. D. Chremmos and N. K. Efremidis, Phys. Rev. A **85**, 063830 (2012).

[17] I. D. Chremmos and N. K. Efremidis, J. Opt. Soc. Am. A **29**, 861 (2012).

[18] N. M. Lučić, B. M. Bokić, D. Ž. Grujić, D. V. Pantelić, B. M. Jelenković, A. Piper, D. M. Jović, and D. V. Timotijević, Phys. Rev. A **88**, 63815 (2013).

[19] A. Piper, D. V. Timotijević, and D. M. Jović, Phys. Scr. **T157**, 014023 (2013).

[20] N. K. Efremidis, S. Sears, D. N. Christodoulides, J. W. Fleischer, and M. Segev, Phys. Rev. E **66**, 046602 (2002).

[21] A. A. Zozulya and D. Z. Anderson, Phys. Rev. A **51**, 1520 (1995).

[22] I. M. Besieris and A. M. Shaarawi, Opt. Lett. **32**, 2447 (2007).

[23] G. A. Siviloglou and D. N. Christodoulides, Opt. Lett. **32**, 979 (2007).

[24] B. Terhalle, D. Träger, L. Tang, J. Imbrock, and C. Denz, Phys. Rev. E **74**, 057601 (2006).

[25] P. Rose, M. Boguslawski, and C. Denz, New J. Phys. **14**, 033018 (2012).

[26] J. Xavier, P. Rose, B. Terhalle, J. Joseph, and C. Denz, Opt. Lett. **34**, 2625 (2009).

[27] T. Schwartz, G. Bartal, S. Fishman, and M. Segev, Nature (London) **446**, 52 (2007).

[28] J. W. Fleischer, M. Segev, N. K. Efremidis, and D. N. Christodoulides, Nature (London) **422**, 147 (2003).

[29] B. Terhalle, T. Richter, A. S. Desyatnikov, D. N. Neshev, W. Krolikowski, F. Kaiser, C. Denz, and Y. S. Kivshar, Phys. Rev. Lett. **101**, 013903 (2008).

[30] N. V. Kukhtarev, V. B. Markov, S. G. Odulov, M. S. Soskin, and V. L. Vinetskii, Ferroelectrics **22**, 949 (1978).

[31] J. Durnin, J. J. Miceli, and J. H. Eberly, Phys. Rev. Lett. **58**, 1499 (1987).

[32] Z. Bouchal, Czechoslov. J. Phys. **53**, 537 (2003).

[33] J. A. Davis, D. M. Cottrell, J. Campos, M. J. Yzuel, and I. Moreno, Appl. Opt. **38**, 5004 (1999).

[34] U. B. Dörfler, R. Piechatzek, T. Woike, M. K. Imlau, V. Wirth, L. Bohatý, T. Volk, R. Pankrath, and M. Wöhlecke, Appl. Phys. B: Lasers Opt. **68**, 843 (1999).

[35] M. R. Belić, J. Leonardy, D. V. Timotijević, and F. Kaiser, J. Opt. Soc. Am. B **12**, 1602 (1995).

[36] M. R. Belić, M. S. Petrović, D. M. Jović, A. Strinić, D. Arsenović, K. Motzek, F. Kaiser, P. Jander, C. Denz, M. Tlidi, and P. Mandel, Opt. Express **12**, 708 (2004).

[37] Y. Hu, S. Huang, P. Zhang, C. Lou, J. Xu, and Z. Chen, Opt. Lett. **35**, 3952 (2010).

[38] F. Diebel, D. Leykam, M. Boguslawski, P. Rose, C. Denz, and A. Desyatnikov, Appl. Phys. Lett. **104**, 261111 (2014).

[39] M. Boguslawski, A. Kelberer, P. Rose, and C. Denz, Opt. Express **20**, 27331 (2012).

[40] M. Boguslawski, A. Kelberer, P. Rose, and C. Denz, Opt. Lett. **37**, 797 (2012).

Soliton formation by decelerating interacting Airy beams

Falko Diebel[1,*]**, Bojana M. Bokić**[2]**, Dejan V. Timotijević**[2]**,**
Dragana M. Jović Savić[2]**, and Cornelia Denz**[1]

[1]*Institut für Angewandte Physik and Center for Nonlinear Science (CeNoS),*
Westfälische Wilhelms-Universität Münster, 48149 Münster, Germany
[2]*Institute of Physics, University of Belgrade , P.O. Box 68, 11080 Belgrade, Serbia*

[*]*falko.diebel@uni-muenster.de*

Abstract: We demonstrate a new type of soliton formation arising from the interaction of multiple two-dimensional Airy beams in a nonlinear medium. While in linear regime, interference effects of two or four spatially displaced Airy beams leads to accelerated intensity structures that can be used for optical induction of novel light guiding refractive index structures, the nonlinear cross-interaction between the Airy beams decelerate their bending and enables the formation of straight propagating solitary states. Our experimental results represent an intriguing combination of two fundamental effects, accelerated optical beams and nonlinearity, together enable novel mechanisms of soliton formation that will find applications in all-optical light localization and switching architectures. Our experimental results are supported by corresponding numerical simulations.

OCIS codes: (190.4420) Nonlinear optics, transverse effects in; (190.6135) Spatial solitons; (350.5500) Propagation; (190.5330) Photorefractive optics; (140.3300) Laser beam shaping; (070.6120) Spatial light modulators

---

References and links

1. M. V. Berry and N. L. Balazs, "Nonspreading wave packets," Am. J. Phys. **47**, 264 (1979).
2. G. A. Siviloglou and D. N. Christodoulides, "Accelerating finite energy Airy beams," Opt. Lett. **32**, 979 (2007).
3. G. A. Siviloglou, J. Broky, A. Dogariu, and D. N. Christodoulides, "Observation of Accelerating Airy Beams," Phys. Rev. Lett. **99**, 213901 (2007).
4. J. Broky, G. A. Siviloglou, A. Dogariu, and D. N. Christodoulides, "Self-healing properties of optical Airy beams." Opt. Express **16**, 12880 (2008).
5. J. Baumgartl, M. Mazilu, and K. Dholakia, "Optically mediated particle clearing using Airy wavepackets," Nat. Photonics **2**, 675 (2008).
6. M. A. Bandres, I. Kaminer, M. S. Mills, B. M. Rodríguez-Lara, E. Greenfield, M. Segev, and D. N. Christodoulides, "Accelerating optical beams," Opt. Photonics News **24**, 30 (2013).
7. A. Mathis, F. Courvoisier, L. Froehly, L. Furfaro, M. Jacquot, P. A. Lacourt, and J. M. Dudley, "Micromachining along a curve: Femtosecond laser micromachining of curved profiles in diamond and silicon using accelerating beams," Appl. Phys. Lett. **101**, 99 (2012).
8. P. Polynkin, M. Kolesik, J. V. Moloney, G. A. Siviloglou, and D. N. Christodoulides, "Curved plasma channel generation using ultraintense Airy beams." Science **324**, 229 (2009).
9. A. Chong, W. H. Renninger, D. N. Christodoulides, and F. W. Wise, "Airy-Bessel wave packets as versatile linear light bullets," Nat. Photonics **4**, 103 (2010).
10. N. K. N. Efremidis, "Airy trajectory engineering in dynamic linear index potentials," Opt. Lett. **36**, 3006 (2011).
11. N. K. N. Efremidis, "Accelerating beam propagation in refractive-index potentials," Phys. Rev. A **89**, 023841 (2014).
12. K. G. Makris, I. Kaminer, R. El-Ganainy, N. K. N. Efremidis, Z. Chen, M. Segev, and D. N. Christodoulides, "Accelerating diffraction-free beams in photonic lattices," Opt. Lett. **39**, 2129 (2014).

13. S. Chávez-Cerda, U. Ruiz, V. Arrizón, and H. M. Moya-Cessa, "Generation of Airy solitary-like wave beams by acceleration control in inhomogeneous media." Opt. Express **19**, 16448 (2011).
14. N. M. Lučić, B. M. Bokić, D. v. Grujić, D. V. Pantelić, B. M. Jelenković, A. Piper, D. M. Jović, and D. V. Timotijević, "Defect-guided Airy beams in optically induced waveguide arrays," Phys. Rev. A **88**, 63815 (2013).
15. F. Diebel, B. M. Bokić, M. Boguslawski, A. Piper, D. V. Timotijević, D. M. Jović, and C. Denz, "Control of Airy-beam self-acceleration by photonic lattices," Phys. Rev. A **90**, 033802 (2014).
16. P. Rose, F. Diebel, M. Boguslawski, and C. Denz, "Airy beam induced optical routing," Appl. Phys. Lett. **102**, 101101 (2013).
17. R. Bekenstein and M. Segev, "Self-accelerating optical beams in highly nonlocal nonlinear media," Opt. Express **19**, 23706 (2011).
18. Y. Hu, S. Huang, P. Zhang, C. Lou, J. Xu, and Z. Chen, "Persistence and breakdown of Airy beams driven by an initial nonlinearity." Opt. Lett. **35**, 3952 (2010).
19. Y. Hu, G. A. Siviloglou, P. Zhang, N. K. N. Efremidis, D. N. Christodoulides, and Z. Chen, *Nonlinear Photonics and Novel Optical Phenomena*, vol. 170 of *Springer Series in Optical Sciences* (Springer New York, New York, NY, 2012).
20. R. Driben, V. V. Konotop, and T. Meier, "Coupled Airy breathers," Opt. Lett. **39**, 5523 (2014).
21. Y. S. Kivshar and G. P. Agrawal, *Optical Solitons: From Fibers to Photonic Crystals* (Academic Press, San Diego, 2003).
22. C. Denz, M. Schwab, and C. Weilnau, *Transverse-Pattern Formation in Photorefractive Optics*, vol. 188 of *Springer Tracts in Modern Physics* (Springer, Berlin, 2003).
23. F. Lederer, G. I. Stegeman, D. N. Christodoulides, G. Assanto, M. Segev, and Y. Silberberg, "Discrete solitons in optics," Phys. Rep. **463**, 1–126 (2008).
24. B. Terhalle, T. Richter, A. S. Desyatnikov, D. N. Neshev, W. Królikowski, F. Kaiser, C. Denz, and Y. S. Kivshar, "Observation of Multivortex Solitons in Photonic Lattices," Phys. Rev. Lett. **101**, 013903 (2008).
25. F. Diebel, D. Leykam, M. Boguslawski, P. Rose, C. Denz, and A. S. Desyatnikov, "All-optical switching in optically induced nonlinear waveguide couplers," Appl. Phys. Lett. **104**, 261111 (2014).
26. Y. Zhang, M. R. Belić, Z. Wu, H. Zheng, K. Lu, Y. Li, and Y. Zhang, "Soliton pair generation in the interactions of Airy and nonlinear accelerating beams." Opt. Lett. **38**, 4585 (2013).
27. Y. Y. Zhang, M. R. Belić, H. Zheng, H. Chen, C. Li, and Y. Li, "Interactions of Airy beams , nonlinear accelerating beams , and induced solitons in Kerr and saturable nonlinear media," Opt. Express **22**, 3791 (2014).
28. I. M. Allayarov, and E. N. Tsoy, "Dynamics of Airy beams in nonlinear media," Phys. Rev. A **90**, 023852 (2014).
29. A. A. Zozulya and D. Z. Anderson, "Propagation of an optical beam in a photorefractive medium in the presence of a photogalvanic nonlinearity or an externally applied electric field," Phys. Rev. A **51**, 1520 (1995).
30. J. A. Davis, D. M. Cottrell, J. Campos, M. J. Yzuel, and I. Moreno, "Encoding Amplitude Information onto Phase-Only Filters," Appl. Opt. **38**, 5004 (1999).
31. U. B. Dörfler, R. Piechatzek, T. Woike, M. K. Imlau, V. Wirth, L. Bohatý, T. Volk, R. Pankrath, and M. Wöhlecke, "A holographic method for the determination of all linear electrooptic coefficients applied to Ce-doped strontium-barium-niobate," Appl. Phys. B Lasers Opt. **68**, 843 (1999).
32. N. K. N. Efremidis and D. N. Christodoulides, "Abruptly autofocusing waves," Opt. Lett. **35**, 4045 (2010).
33. D. G. Papazoglou, N. K. Efremidis, D. N. Christodoulides, and S. Tzortzakis, "Observation of abruptly autofocusing waves." Opt. Lett. **36**, 1842 (2011).
34. W. Królikowski, C. Denz, A. Stepken, M. Saffman, and B. Luther-Davies, "Interaction of spatial photorefractive solitons," Quantum Semiclassical Opt. J. Eur. Opt. Soc. Part B **10**, 823 (1998).

1. Introduction and motivation

Airy wave packets, first predicted by Berry and Balazs [1] as free-particle solutions of the Schrödinger equation are remarkable objects within the framework of quantum mechanics. The envelope of these wave packets is described by Airy functions, centered around a parabolic trajectory. Their unique ability to freely accelerate during propagation – even in the absence of any external potential – stands out the Airy wave from any other known solution. Airy wave packets were also predicted [2], and then realized [3] in the optical domain. Their special self-healing properties – self-restoration of their canonical form after passing small obstacles – were demonstrated theoretically and experimentally [4]. The unique ballistic-like and self-accelerating properties of the Airy beam made it ideally suited for various applications ranging from particle and cell micromanipulation, optical snow-blowers [5, 6], laser micromachining [7] and self-bending plasma channels [8] to ultrafast self-accelerating pulses [9].

While the potential of tailored light fields, especially Airy beams, is well recognized in these

fields, they are also of significant importance for advances in discrete and nonlinear modern photonics. On the one hand, the influence of inhomogeneous refractive index potentials on Airy beams has been investigated theoretically to design the beam caustics [10, 11, 12], on the other hand it was experimentally demonstrated that a linear refractive index gradient or a photonic lattice can be used to control and compensate the Airy beam self-acceleration [13, 14, 15]. Another inventive idea shifts the perspective and uses two-dimensional Airy beams itself to optically induce light guiding structures for optical routing and switching of signals [16].

By considering nonlinearity a new degree of freedom is added to the system which leads to interesting new effects of Airy beam propagation investigated in several theoretical and experimental studies [17, 18, 19, 20]. One of the most fundamental effect in nonlinear systems is the existence of spatial solitons which represents localized structures that always preserve their shape by the balance between diffraction and nonlinear self-focusing. In optics, they have extensively been studies in various systems, including bulk nonlinear media or discrete systems [21, 22, 23], where fundamental solitons or even vortex solitons [24, 25] have been found. The interesting question now is if solitons or solitary structures can arise from the interaction of initially accelerated beams such as Airy beams. Very recently, first numerical studies have started to explore the interaction between two one-dimensional Airy beams in an isotropic idealized nonlinear model [26, 27, 28].

In this paper, we investigate the nonlinear interaction of two-dimensional Airy beams experimentally, as well as numerically. Therefore, we introduce advanced experimental methods to synthesize multiple accelerated Airy beams with fully controllable parameters and observe the nonlinear dynamics of this compound optical field in a photorefractive nonlinear crystal, an ideal experimental testbed for nonlinear light-matter interaction. We demonstrate that these interactions lead to solitary structures that arise from nonlinear interaction of two or four involved accelerated Airy beams. Depending on the beam intensity and on different phase configurations of the synthesized beams (in phase or out of phase), either one solitary solution or a pair is observed that propagates almost stable with small intensity modulations (breathing). Moreover, we demonstrate how the synthesized beams propagate in the linear regime, where interference leads to interesting intensity modulations, including tight-focus structures. To precisely describe all our experimental observations in a theoretical framework, we extend and generalize existing concepts to handle multiple Airy beams, as well as nonlinear propagation in the more realistic anisotropic photorefractive model.

2. Theoretical model and numerical methods

To study the propagation characteristics of Airy beams in a nonlinear optical system with intensity dependent refractive index modulations, we consider the scaled paraxial equation of diffraction for the envelope A of the optical field:

$$i\frac{\partial A}{\partial \zeta} + \frac{1}{2}\left(\frac{\partial^2 A}{\partial \chi^2} + \frac{\partial^2 A}{\partial v^2}\right) + \frac{1}{2}k_0^2 w_0^2 \Delta n^2(I)A = 0. \tag{1}$$

Here, $\chi = x/w_0$ and $v = y/w_0$ are the dimensionless transverse coordinates scaled by the characteristic length w_0. $\zeta = z/kw_0^2$ represents the dimensionless propagation distance with $k = 2\pi n/\lambda$.

In this equation, the nonlinearity is given by an intensity-dependent refractive index modulation $\Delta n^2(I)$, with $I \propto |A|^2$, which is caused by the nonlinear response of a photorefractive medium. Theoretically, it is well described by the electro-optic effect combined with the band transport model, which in our case can be approximated by the full anisotropic model for the

optically induced space charge potential ϕ, [29]

$$\nabla^2\phi + \nabla\ln(1+I)\cdot\nabla\phi = E_{\text{ext}}\frac{\partial}{\partial x}\ln(1+I) + \frac{k_{\text{B}}T}{e}\left(\nabla^2\ln(1+I) + (\nabla\ln(1+I))^2\right),\quad (2)$$

where the refractive index modulation results from the electro-optic effect as $\Delta n^2 = n_0^4 r_{\text{eff}}\partial_x\phi$, and r_{reff} is the effective electro-optic coefficient.

This model precisely describes the optical induction process in a photorefractive nonlinear medium with applied electric field E_{ext} along the crystal's c-axis and accounts for the orientation anisotropy caused by the resulting directed transport of charge carriers. Moreover, this model is capable to describe the effect of charge carrier diffusion in the internal space charge field. This effects plays an important role for non-zero temperatures T and non-zero dark conductivity of the crystal, and leads to effects such as nonlinear soliton steering in bulk nonlinear media.

2.1. Two-dimensional Airy beams

In the linear regime, where $\Delta n(I) = 0$ holds, the wave equation can be solved by two-dimensional truncated Airy beam solutions that reads as

$$\psi(\chi,v,\zeta) = A_0\varphi(\chi,\zeta)\varphi(v,\zeta), \tag{3}$$

with

$$\varphi(X,\zeta) = \text{Ai}\left[X - \frac{\zeta^2}{4} + ia_X\zeta\right]$$
$$\exp\left[\frac{i}{12}\left(6a_X^2\zeta - 12ia_XX + 6ia_X\zeta^2 + 6X\zeta - \zeta^3\right)\right], \text{ with } X = \{\chi,v\} \tag{4}$$

Here, $\text{Ai}(X)$ is the Airy function, A_0 the amplitude and a_X a positive decay length that truncates the solution to become physically relevant. In the focal plane ($\zeta = 0$) the one-dimensional Airy functions reads as $\varphi(X,0) = \text{Ai}[X]\exp[a_XX]$, where the exponential decay clearly can be seen. Without this truncations the solution will extended over the whole space and contains infinite energy. These truncated solutions still solves the wave equation (1) and the distinguished properties of Airy beams are mostly preserved [2]

2.2. Numerical methods

Due to the inhomogeneous refractive index modulation $\Delta n^2(I_{\text{indu}})$, which here is caused by the nonlocal, anisotropic photorefractive nonlinearity, the paraxial wave equation (1) cannot be solved analytically. Thus, we have implemented comprehensive numerical methods to solve this equation and model the light propagation in nonlinear media. The propagation equation (1) is evaluated numerically, using split-step Fourier methods. In the nonlinear regime, the inducing intensity $I_{\text{indu}} = |A|^2$ is given by the intensity of the propagating wave field itself (cf. (1)). Therefore, it is crucial to calculate the optically induced refractive index modulation for each propagation step. This index modulation, represented by $\Delta n^2(I_{\text{indu}})$, is calculated in full anisotropic model [29] using a relaxation method.

3. Experimental realization of interacting Airy beams in photorefractive media

All the experiments presented here are performed using the setup sketched in Fig. 1(a). The light from a frequency-doubled Nd:YVO$_4$ laser continuously emitting light at a wavelength of $\lambda = 532\,\text{nm}$ is expanded and illuminates a programmable, high-resolution phase-only spatial light modulator (SLM). The plane wave that enters the modulator experiences a spatial phase
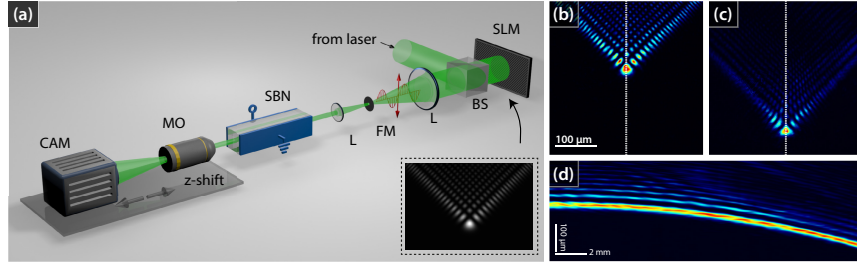
Fig. 1. Experimental setup and single Airy beam characteristics. (a) Experimental setup (SLM: Spatial light modulator, BS: beam splitter, FM: Fourier mask, SBN: strontium barium niobate crystal, MO: microscope objective). (b–d) Linear propagation of a single two-dimensional Airy beam through the homogeneous crystal. (b),(d): Intensity at the input and output face of the crystal, (c) cross-section during propagation.

modulation, which in combination with two following lenses and a Fourier filter leads to any desired complex light field at the input face of the nonlinear photorefractive medium. Therefore, we address an explicitly designed phase pattern to the SLM that allows us to modulate phase and amplitude of the light field at the same time [30]. In this way, we realize different complex light fields as combination of multiple displaced two-dimensional Airy beams, whose field distributions are calculated with (3).

This structured beam then illuminates the 20 mm long photorefractive $Sr_{0.60}Ba_{0.40}Nb_2O_6$ (SBN:Ce) crystal which is externally biased with an electric dc field of $E_{ext} \approx 1000\,V\,cm^{-1}$ aligned along the optical c-axis. We take care that the input face of the crystals coincides with the plan corresponding to the SLM's surface. To maximize the nonlinear self-action of the written refractive index structure onto the beam itself – in other words the nonlinearity – the beam is set to be extraordinarily polarized with respect to the crystal's optical c-axis. The high electro-optic coefficient of SBN:Ce [31] facilitates sufficient nonlinearity to substantially change the propagation of the Airy beam. By illuminating the crystal homogeneously with white light, we can erase written refractive index modulations. This reversibility make our experimental approach highly flexible to perform series of experiments using the same nonlinear material. By means of an microscope objective and a camera mounted on a translation stage we can record the intensity distribution in different transverse planes.

4. Linear propagation of multiple Airy beams

The propagation characteristics of single Airy beams have been subject to many experimental and numerical studies in the past years, considering linear and nonlinear effects, or propagation in inhomogeneous or periodically structured media. As it is well known, for linear propagation in a homogeneous environment the Airy beams follows a parabolic trajectory while propagation. This behavior can clearly be seen from the experimentally recorded intensity profile of one single Airy beam (Figs. 1(b–d)) realized with the presented experimental setup (Fig. 1(a)). Although the main scope of this work is the interaction of multiple Airy beams, these basic result are presented to demonstrate that our experimental approach and setup allow to realize two-dimensional accelerated Airy beams with very high accuracy. These results serve as a good starting point for the following experimenters about multiple interacting Airy beams.

To systematically investigate the propagation and interaction of multiple two-dimensional Airy beams, we start our studies with considering the most fundamental case of two co-propagating Airy beams in the linear regime. The beams are coherently superimposed with an initial distance of $d \approx 50\,\mu m$ and are rotated by 180°, so that their accelerated trajectories
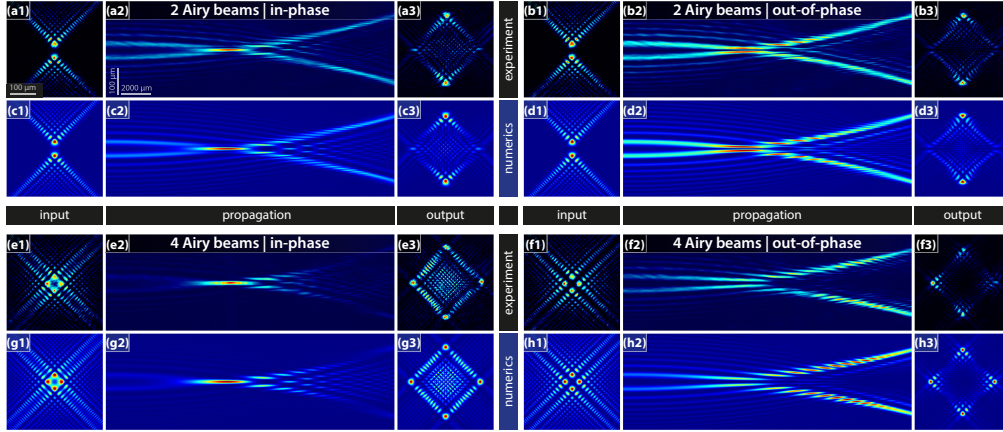
Fig. 2. Interference of multiple Airy beams in homogeneous linear medium. (a–d) Evolution of two Airy beams in experiment and numerics. (a,b) in phase, (c,d) with π phase difference. (e–h) Evolution of four Airy beams in experiment and numerics. (e,f) in phase, (g,h) with π phase difference. Each panel is normalized individually.

will intersect during propagation. The longitudinal position of this intersection point strongly depends on the curvature of the Airy beams which is determined by their size, but also depends on their initial separation. We aim to observe this defined intersection inside the volume of the 20 mm long SBN crystal. Therefore, we set the Airy beam size, measured as the distance between the main lobe and the next neighbor, to $s \approx 25\,\mu m$.

To visualize the complex evolution of the intensity distribution during propagation, we extract cross-sections through the experimentally recorded intensity volume along the coordinate in which the acceleration happens. Our experimental setup allows to retrieve this three-dimensional intensity volume by automatically recording the transverse intensity distribution in many (here 100) different planes along the crystal and stacking them. It is worth to mention that recording the intensity at planes inside the crystals is only possible if the refractive index between this plane and the camera is uniform, in other words, if the crystals in homogeneous.

The experimental results for two Airy beams are shown in Figs. 2(a),(b), with the corresponding numerical simulations in Figs. 2(c),(d). Thereby, we consider two cases where the beams are either in phase, or π out of phase. These different initial conditions result in distinguishable transverse intensity profiles during propagation due to interference. For the in-phase configuration, depicted in Figs. 2(a),(c), a well-pronounced focus is formed by constructive interference of the beams in the intersection region of both accelerated trajectories. This feature of a very high local intensity compared to the surrounding was previously emphasized as the key advantage of so-called autofocusing beams [32, 33]. For the out-of-phase case, shown in Figs. 2(b),(d), the phase difference of π between the beams at the input leads to the vertical separation by a dark line of destructive interference which is preserved during the whole propagation. In both cases, the parabolic trajectories of the two superimposed Airy beams can clearly be identified. Since so far the propagation is completely linear, the complex intensity patterns results only from interference, but the beams do not interact and influence each other. Therefore, their initial general accelerated trajectories are preserved, albeit the beams trajectories intersect.

By increasing the number of the superimposed beams, the next symmetrical configuration can be constructed with four displaced Airy beams each rotated by 90°, as shown in Figs. 2(e–h). In principle there are more possibilities to set the relative phases of the beams, but we want

to limit our studies to the following two cases: either all beams are in phase (Figs. 2(e),(g)), or neighboring beams are π out of phase (Figs. 2(f),(h)). While the transverse intensity profiles now look quite different compared to the situation where two beams are superimposed, the longitudinal cross-sections reveal a similar propagation behavior. Again, a well-pronounced high-intensity focus is formed in the region where the four in-phase Airy beams interfere constructively, while the dark line of destructive interference always separates the beams in the out-of-phase case. Due to the fact that now four beams are interfering, the relative strength of the focus for constructive interference is much higher than for two beams. The number of interfering Airy beams could be further increased while the contrast between the focal intensity and the background continuously grows to the limit achieved by radially distributed Airy beams [32].

All presented experimental results are supported by corresponding numerical simulations. For the propagation of multiple Airy beams in the linear regime the numerical results perfectly fits to the experimental measurements. Although the wave equation (1) for homogenous media ($\Delta n(I) = 0$) has analytical solution in form of truncated Airy beams which can be explicitly calculated for any distance z, we already here employ the numerical beam propagation method to prove and emphasize that the simulation methods we developed precisely describe the real experimental conditions.

5. Nonlinear interaction of multiple two-dimensional Airy beams

From the above presented results we see, that during linear propagation of multiple Airy beams interference alone already leads to interesting intensity distributions, even as the beams do not interact and influence each other. If such an interdependency mediated by a nonlinear light matter interaction is included into the theoretical models and experiments, interesting novel effects can be expected, as for example soliton formation as predicted numerically in [26, 27].

In the following, we will investigate and analyze the nonlinear propagation and interaction of multiple Airy beams experimentally in photorefractive SBN. As introduced above, the refractive index of the nonlinear crystal depends non-locally on the incident intensity distribution and leads to a self-focusing, saturable nonlinearity. This complex nonlinearity completely changes the propagation dynamics of the Airy beams and leads to fascinating new types of beam evolution that depends amongst others on the number of superimposed beams, their relative phase and intensity. The experimental and numerical results for two and four superimposed Airy beams are presented in the following sections.

5.1. Interaction of two Airy beams

We start our investigations about the nonlinear interaction with the most fundamental configuration of two displaced Airy beams. We use the same beam parameters as described above for the linear case (cf. Fig. 2). At the input, the two beams that are separated by $d \approx 50\,\mu m$ and are orientated to accelerate towards each other. Thereby, the trajectories of the undisturbed Airy beams would intersect and the beams strongly interact. In contrast to the linear experiment, we now increase the beam power, as well as the writing time to gain sufficient nonlinearity. To observe the intensity dependency of the propagation dynamics we set four different probe beam powers: $P_{in} \approx \{237,\ 475,\ 950,\ 1.425\}\,nW$ and perform the experiment for each value, while keeping all other parameters such as external field, induction time, and background illumination unchanged.

The experimental results for the in-phase beams are shown in Fig. 3(a). While increasing the probe beam power we can see the transition from the almost linear interference pattern (a1) to a well-localizes, solitary output state for higher nonlinearities (a3),(a4). This localized state origins at the intersection point of the beam trajectories, where the constructive interference
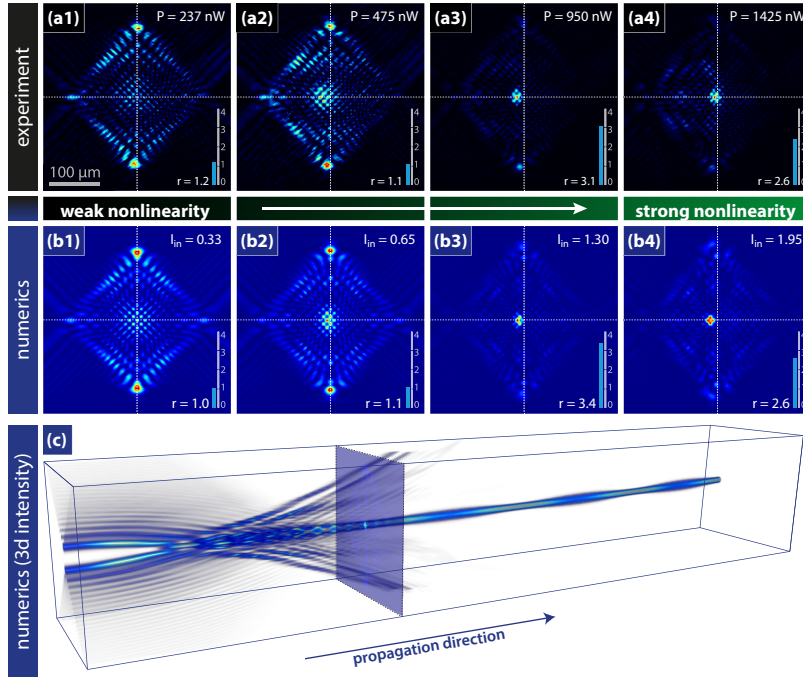
Fig. 3. Formation of solitary states from the interaction of two in-phase Airy beams. (a) Experimental results for different probe beam power. Each panel shows the intensity pattern at the output face of the SBN crystal (individually normalized). (b) Results from corresponding numerical simulations. (c) Volumetric plot of the numerically calculated three-dimensional intensity distribution (three times longer crystal) for strong nonlinearity. The position of the marked plane corresponds to the length of the used SBN crystal, $L = 20\,\text{mm}$ and to figs. (a4),(b4).

of the in-phase Airy beams leads to a strongly increased local intensity. Afterward, it propagates almost unchanged, except small breathing, due to the compensation of the diffraction by nonlinear self-focusing. The merged localized state further propagates straight obviously without any transverse momentum remaining from initial accelerated beams. The nonlinearity allows for this complex interaction between the two beams that in consequence compensates the acceleration. The peak intensity of the resulting state at the output of course is higher than the peak intensity at the input where the individual beams do not noticeably overlap. The factor $r = I_{\text{max,out}}/I_{\text{max,in}}$ (see insets in Fig. 3) represents the ratio between the maximal intensity at the output and the input, respectively. Due to the principal limitation that direct imaging through a non-homogeneous medium is not possible, only the output face of the SBN crystal is accessible for all nonlinear experiments throughout this paper. The factor r helps to compare experiments and numerics also quantitatively.

The comparison between the experimental results Fig. 3(a) and the numerical simulation presented in Figs. 3(b),(c) shows a very good overall agreement. According to the different probe beam powers in the experiment, we simulated the nonlinear propagation for different corresponding input intensities $I_{\text{in}} \approx \{0.33, 0.65, 1.30, 1.95\}$. The output profiles, as well as the intensity factor r perfectly matches the real observations in experiment. This verifies that our implemented numerical methods exactly describe the real situation and justify to employ numerical simulations to get a detailed impression what dynamics happens during nonlinear
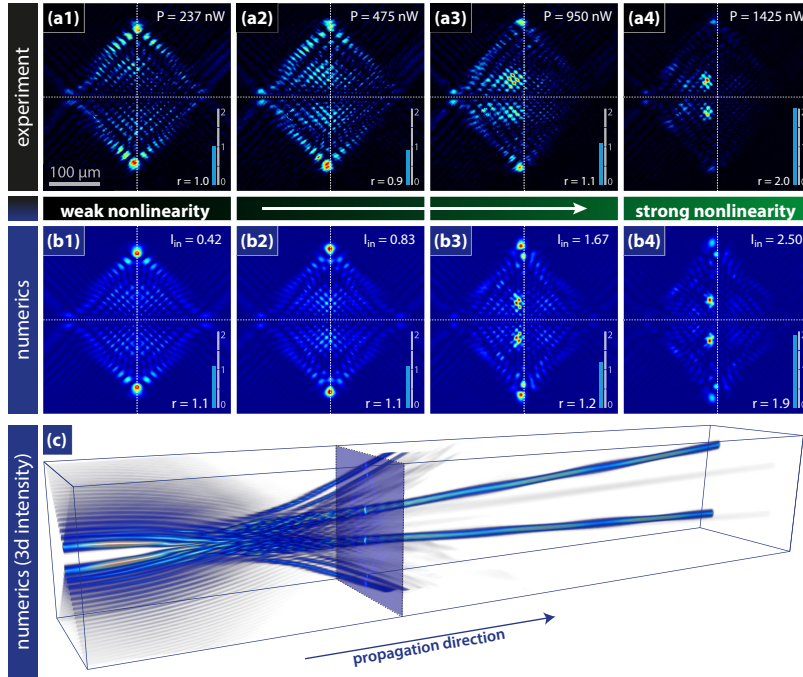
Fig. 4. Formation of solitary states from the interaction of two out-of-phase Airy beams. (a) Experimental results for different probe beam power. Each panel shows the intensity pattern at the output face of the SBN crystal (individually normalized). (b) Results from corresponding numerical simulations. (c) Volumetric plot of the numerically calculated three-dimensional intensity distribution (three times longer crystal) for strong nonlinearity. The position of the marked plane corresponds to the length of the used SBN crystal, $L = 20\,\text{mm}$ and to figs. (a4),(b4).

propagation in the SBN crystal. As mentioned above, in the experiment these data are not accessible due to principle physical reasons.

Figure 3(c) shows a volumetric rendering of the numerically retrieved intensity distribution during nonlinear propagation. The formation of the solitary state is clearly visible. While during the build-up process noticeable modulations in the shape and the intensity of the solitary state occurs (i.a. due to the passing of the remaining side lobes of the initial Airy beams), after some propagation distance the situation stabilizes and the solitary state propagates almost unchanged, except small breathing. The marked plane in Fig. 3(c) corresponds to the length of the SBN crystal and the pictures shown in Figs. 3(a),(b).

A similar localization behavior was also found numerically for simpler idealized isotropic Kerr, and saturable Kerr nonlinearities [27]. For the presented experimental and numerical results in a realistic photorefractive SBN crystal, the situation is much more complicated, due to the anisotropic, saturable and drift-dominated nonlinearity. The slight shift of the intensity peaks in horizontal direction can be explained by additionally taking into account diffusion effects in the numerical model.

In the opposite case where the two Airy beams are π out of phase, the situation is completely changed, as can be seen from the results shown in Fig. 4. The two main lobes do not merge (c.f. Figs. 2(c),(d)) due to the separating line of destructive interference in the middle between the beams. As a consequence, two localized solitary spots build up and stably propagate as a
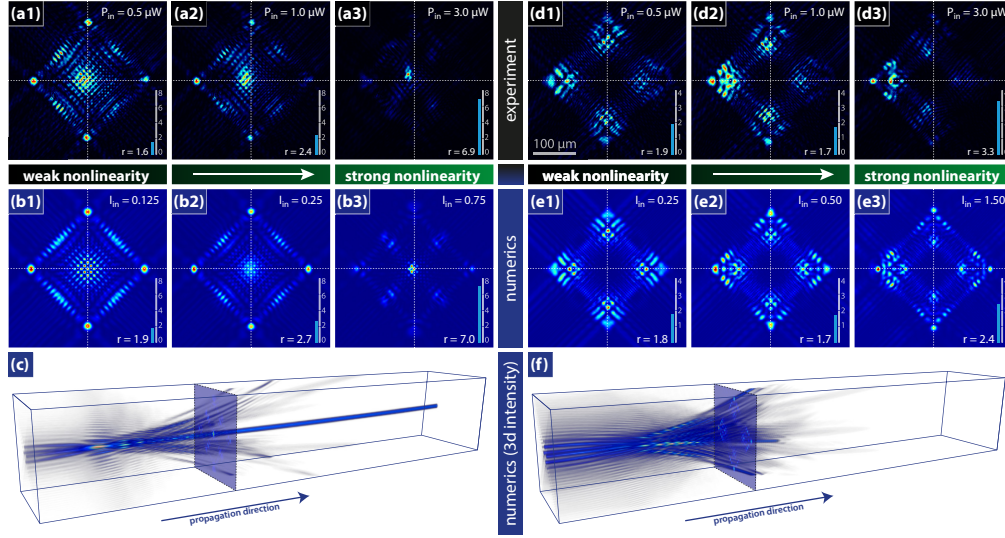
Fig. 5. Interaction of four Airy beams. (left) Formation of solitary state for the case where the beams are in phase. (right) Nonlinear propagation for π phase difference. (a),(d) Experimental results for different probe beam power. Each panel shows the intensity pattern at the output face of the SBN crystal (individually normalized). (b,e) Results from corresponding numerical simulations. (c,f) Volumetric plot of the three-dimensional intensity distribution (from numerics) for strong nonlinearity.

pair over large distances. Again, the build-up process is accompanied by intensity modulations, but after a certain distance only small breathing remains. Introduced by the initial phase difference, these two solitons also have a phase difference of π and hence repel each other, as reported for fundamental solitons [34]. Therefore, they propagate on straight lines but with a small divergence, as can bee seen in Fig. 4(c). The remaining side lobes of the initially launched Airy beams further follows their parabolic trajectory and quickly depart out of the volume.

5.2. Interaction of four Airy beams

After investigating the nonlinear processes for the fundamental case of two interacting Airy beams, we now turn towards the more advanced case where four beams are synthesized. The four Airy beams are combined in the way that their trajectories will intersect, as described above (c.f. Fig. 2). In general, four beams allow more than two different phase configuration with integer values in units of π, nevertheless we restrict ourselves to the two cases: either all beams are in phase, or with π phase difference between neighboring beams. These two cases leads to completely different results.

For the case where all beam are in phase, the results are shown in Fig. 5 (left). Although the transverse intensity structure at the input face of the crystal looks different since now four beams are superimposed, the general nonlinear behavior is similar to the case where two Airy beams were launched in phase (c.f. Fig. 3). With increasing nonlinearity, the intensity localizes in the middle and forms a stable solitary state that emerges from the constructive interference of the beams in the region where their trajectories intersect. The experimental results for three different beam intensities $P_{in} \approx \{0.5, 1.0, 3.0\}\,\mu W$ (Figs. 5(a)) clearly show the described formation of the solitary state as the transition from the four separated Airy main lobes (see (a1)) to the high-intensity localized state (see (a3)). Here, the ratio r between the maximal intensity at the input and the peak intensity of the built-up solitary state is much higher compared to the

two-beam case, which is understandable because four beams are merging.

The situation is completely changed for the configuration with a phase difference of π between neighboring beams. The corresponding results are shown in Fig. 5 (right). In contrast to all other presented cases, here neither a straight soliton nor a soliton-pair or cluster is forming. Owed to the phase differences, no pronounced high-intensity spot arises from interference at the intersection of the beam trajectories that could develop into a soliton. Moreover, the remaining side lobes of the four Airy beams prevent the build-up of a solitary states or clusters, like it was observed in the previous case for two beams (Fig. 4). For higher intensities, the intensity tends to localize predominantly on one side (cf. Fig. 5(d3)) and keeps traveling away from the center.

Comparing all results of the nonlinear interaction of two and four Airy beams, we could identity three different types of nonlinear dynamic. First, in all cases where the synthesized beams are in phase, the interaction leads to the formation of one single stable spatial solitary state initiated by the high intensity resulting from constructive interference of the main lobes. The second type, the formation of a solitary pair, could be observed if two beams are superimposed with a phase difference of π. For these two types the acceleration of the initial Airy beams is exactly compensated, leading to straight propagating solutions. Interestingly, there is a third type where no solitary structures appears, even for the same intensities and nonlinearities. This could be observed if four Airy beams are superimposed with π phase difference, as it was done in the last example. For this configuration the nonlinear dynamic shows symmetry-breaking behavior that depends critically on small perturbations and asymmetries in the system. The directed diffusion of charge carriers inside the photorefractive SBN crystals causes such an asymmetry, that is also responsible for the horizontal shift of the other solitary solutions, as reported above.

Conclusion

In summary, we have presented the first experimental and numerical study about nonlinear interaction of multiple two-dimensional Airy beams. As the most important result, we could demonstrate the build-up of solitary structures from the nonlinear interaction of multiple accelerated beams. By investigating the nonlinear dynamic of the superimposed Airy beams for different configurations (numbers of beams, phase relations), we could demonstrate the intensity-dependent formation of straight propagating solitary states or pairs. These fundamental results could be achieved using a highly-developed experimental platform to perform nonlinear experiments which allows us to precisely shape the input beam as requested and reproducibly control all relevant parameters, such as input beam power, external electric field, and illumination time. Our experimental results and methods enable further investigations about the interaction of other types of tailored optical beams (e.g. nondiffracting beams) and moreover could find applications in modern optical information processing architectures as a basis for light guiding and switching approaches.

Funding information
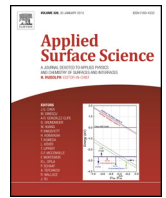
Surface nanopatterning of Al/Ti multilayer thin films and Al single layer by a low-fluence UV femtosecond laser beam

Aleksander G. Kovačević [a],[*], Suzana Petrović [b], Bojana Bokić [a], Biljana Gaković [b], Miloš T. Bokorov [c], Borislav Vasić [a], Radoš Gajić [a], Milan Trtica [b], Branislav M. Jelenković [a]

[a] Institute of Physics, University of Belgrade, Pregrevica 118, 11080 Beograd, Serbia
[b] Institute of Nuclear Sciences "Vinča", University of Belgrade, PO Box 522, 11001 Belgrade, Serbia
[c] Center for Electron Microscopy, University of Novi Sad, Trg Dositeja Obradovića 2, 21000 Novi Sad, Serbia

ARTICLE INFO

ABSTRACT

The effects of UV femtosecond laser beam with 76 MHz repetition rate on two types of thin films on Si substrate – the Al single layer thin film, and the multilayered thin film consisted of five Al/Ti bilayers (total thickness 130 nm) – were studied. The surface modification of the target was done by low fluences and different irradiation times, not exceeding ∼300 s. Nanopatterns in the form of femtosecond-laser induced periodic surface structures (fs-LIPSS) with periodicity of <315 nm and height of ∼45 nm were registered upon irradiation of the thin films. It was shown that: (i) the fs-LIPSS evolve from ruffles similar to high spatial frequency LIPSS (HSFL) into a low spatial frequency LIPSS (LSFL) if a certain threshold of the fluence is met, (ii) the number of LSFL increases with the exposition time and (iii) the LSFL remain stable even after long exposure times. We achieved high-quality highly-controllable fabrication of periodic structures on the surface of nanosized multilayer films with high-repetition-rate low-fluence femtosecond laser pulses. Compared to the Al single layer, the presence of the Ti underlayer in the Al/Ti multilayer thin film enabled more efficient heat transmittance through the Al/Ti interface away from the interaction zone which caused the reduction of the ablation effects leading to the formation of more regular LIPSS. The different outcomes of interactions with multi and single layer thin films lead to the conclusion that the behavior of the LIPSS is due to thin film structure.

© 2014 Elsevier B.V. All rights reserved.

1. Introduction

The occurrence of periodic structures on material surfaces induced by pulsed laser irradiation (LIPSS) has been attracting attention due to potential and interesting applications [1–10]. Various materials have been used, ranging from metals and semiconductors to dielectrics and compounds, as well as from bulk to thin films. Moreover, lasers with different operation modes and beam parameters have been used [1,2,4,11–14]. Two types of periodic structures generally occur, high spatial frequency LIPSS (HSFL) and low spatial frequency LIPSS (LSFL) [15,16].

In the femtosecond range, near infrared (NIR) irradiation (around 800 nm) with fluences >100 mJ/cm^2 is commonly used with the tendency that produced periodic structures disintegrate after a great number of pulses [4,7,9]. For many metals, the absorption for normal incidence is low in the infrared (IR) and NIR, rising in the visible (VIS) and being high in the ultraviolet (UV) part of the spectrum. However, by showing low absorption (high reflectivity) in the UV, Al surpasses all the others, posing challenging difficulties for laser-induced surface modifications [17–20]. Using UV beams would in return lead to the formation of periodic structures of lower spatial period [16], which gives more opportunity for finer nanopattening. The interaction of femtosecond laser beam with surfaces leads to the adsorption of the oxygen and nitrogen from the atmosphere, which changes the surface properties [21].

Formation of periodic nanostructures influences the tribological properties of the surfaces [22]. Aluminum-titanium (Al/Ti) multilayer thin films have been attractive for structural coatings in mechanical applications, due to their extraordinary wearing behavior and corrosion resistance. Adding a Ti to Al alloy can lead to the formation of a fine scale, equiaxed grain structure, which reduces hot tearing, increases feeding to eliminate shrinkage porosity and thus improves the mechanical properties [23]. The fs-beam nanostructuring of Al surface has been present in

the literature [24–27]. The interaction of femtosecond laser beam with Al/Ti multilayer structures on silicon has not been sufficiently described in literature, especially for low laser intensities, below the ablation threshold. Therefore, it is expected that exposing the Al/Ti multilayer to fs beam would change the tribological and chemical properties of the surface. We have irradiated the Al/Ti multilayer and Al single layer thin films with femtosecond UV (390 nm) laser pulses of low single pulse fluence (<100 mJ/cm^2) and demonstrated the emergence of femtosecond-laser induced periodic surface structures (fs-LIPSS) on the top surface of the multilayered structure. The evolution of initial nanoroughness to the LSFL has been interpreted and the causes of the LSFL formation have been suggested. The difference in surface modifications after fs laser interactions with Al/Ti multilayered and Al single layered thin films has been demonstrated.

2. Experimental setup

We have irradiated two types of targets. The target/specimen of the first type was comprised of the silicon (1 0 0) wafer on which five Al/Ti bilayers were deposited reaching the total thickness of ~130 nm (each layer of ~13 nm). The second type was Al single layer of ~130 nm of thickness on the wafer of same type. The depositions were performed by the Balzers Sputron II apparatus using 1.3 keV argon ions and with 99.9% of Al and Ti targets purity.

The irradiations were performed in air with focused femtosecond laser beam under normal incidence at the top layer (Al). The beam was generated by the Coherent Mira 900 Ti:Sapphire system, frequency-doubled by the Inrad 5-050 ultrafast harmonic

generation system (as a second-harmonic generator, SHG), and its wavelength monitored with the Ocean Optics HR2000CG-UV-NIR fiber-optic spectrometer (Fig. 1). The beam properties at the target were: wavelength 390 nm, pulse duration ~150 fs, repetition rate 76 MHz (corresponding to ~13 ns of interpulse time), power of 160–260 mW, linear polarization in the horizontal plane, Gaussian-like elliptic profile. The exposition times were between 1 and 300 s.

The results have been analyzed by scanning electron microscopy (SEM): the JEOL JSM 6560 LV system with the Oxford Instruments EDS analyzer (typical spatial resolution ~2 μm^3) and atomic force microscopy (AFM) by the NT-MDT NTEGRA Prima system in the tapping mode with NSG01 probes (tip curvature radius 6 nm).

3. Results and discussion

Selected results of the surface changes after laser irradiation (SEM micrographs) are presented in Figs. 2–5. Changing the beam power resulted in the single pulse fluence range between 8.6 and 14 mJ/cm^2. The irradiation time was between 1 and 300 s.

In Fig. 2(a), the illuminated area (IA) on Al/Ti multilayer thin film sample generated by the beam of single pulse fluence 14 mJ/cm^2 during 1 s of exposition time is shown. This corresponds to effective delivered power per spot of 1.06 MW/cm^2. The time between two consecutive pulses (the interpulse time) was ~13 ns for all cases of irradiation. The elliptically-shaped modified area (MA) of dimensions 2.07 μm × 3.40 μm stands out from the surroundings by its ruffles (the form of regrouping of the surface material), i.e. a noise in which a certain periodicity can be recognized similar to high HSFL [16]. For the same single pulse fluence but longer exposition
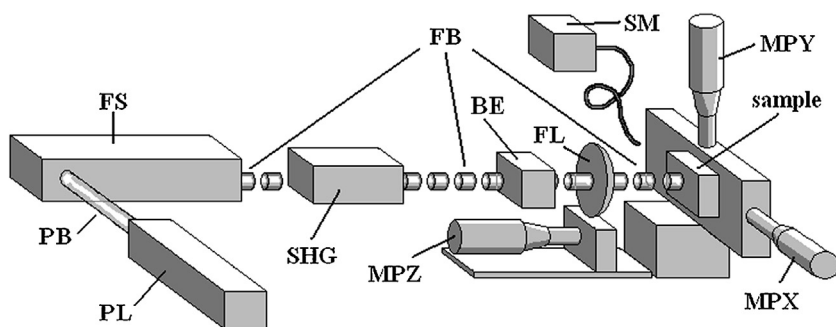
Fig. 1. Experimental setup; PL – pump laser, PB – pump beam, FS – femtosecond laser, FB – femtosecond beam, SHG – second-harmonic generator, FL – focusing lens (f = 5 mm), MPX, MPY, MPZ – micropositioners, SM – spectrometer.

Fig. 2. SEM micrograph of the spots generated on the Al/Ti sample by the beam of: (a) 14 mJ/cm^2 single pulse fluence and 1 s exposition time (effective delivered power per spot 1.06 MW/cm^2); (b) 14 mJ/cm^2 and 2 s (1.06 MW/cm^2); (c) 13.6 mJ/cm^2 and 10 s exposition time (1.03 MW/cm^2). White bar represents 1 μm.

Fig. 3. SEM micrograph of the spot on the Al thin film specimen, generated by the beam of 8.6 mJ/cm^2 single pulse fluence (effective delivered power per spot 654 kW/cm^2): (a) exposition time 1 s; (b) exposition time 4 s; (c) exposition time 10 s. White bar represents 1 μm.
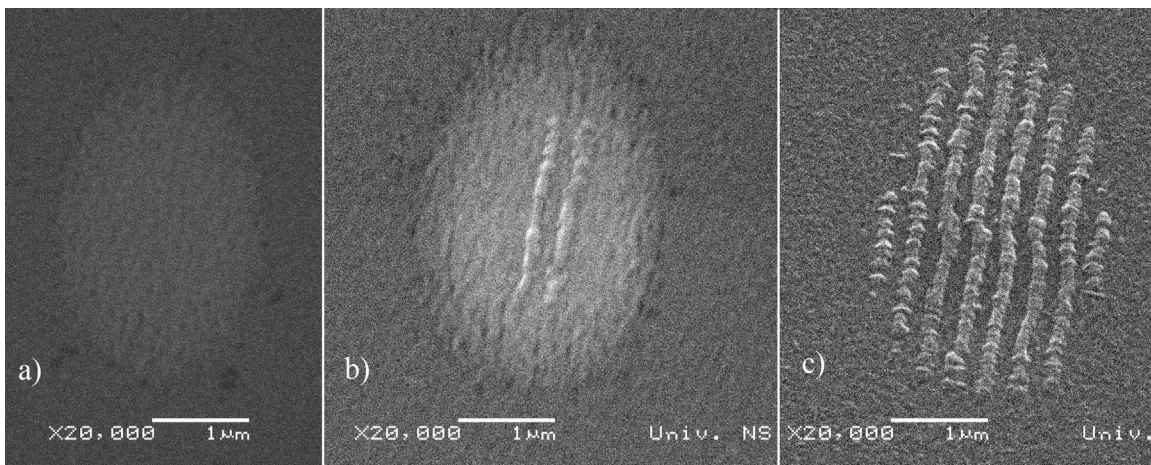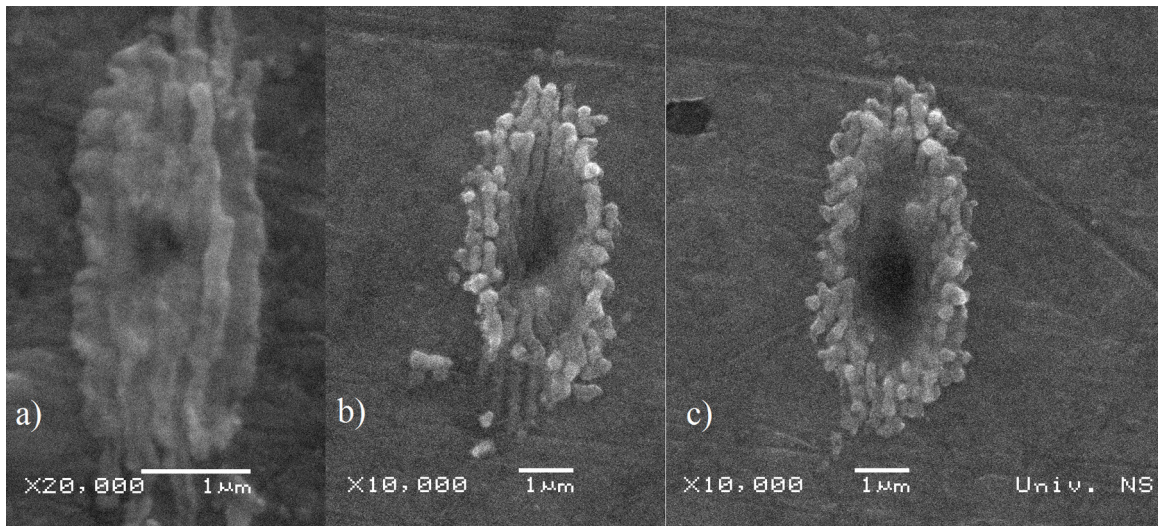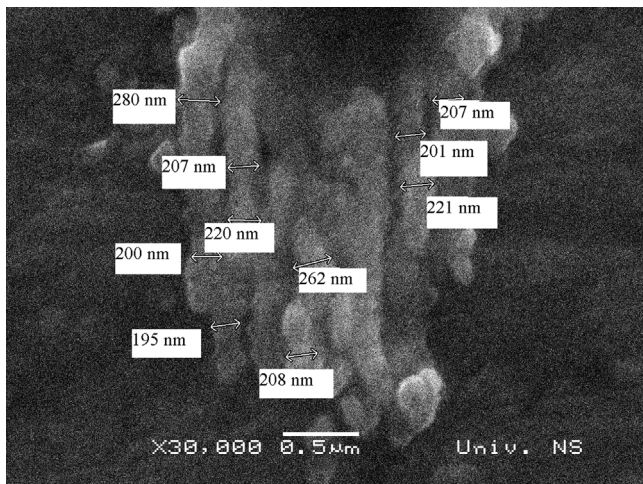

Fig. 4. SEM micrograph of the spot on the Al thin film specimen, generated by the beam of 8.6 mJ/cm^2 single pulse fluence and exposition time of 2 s (effective delivered power per spot 654 kW/cm^2). Detailed view with the dimensions of ripples. White bar represents 1 μm.

time, besides ruffles two prominent ripples were formed in the MA, as seen in Fig. 2(b). The ripples, having the shape of a string of nanoparticles, were 130 nm wide, 2 μm long and perpendicular to the direction of the beam polarization. For even longer exposition times, greater number of ripples was formed; however, the ripples remained limited inside the MA, Fig. 2(c). The periodicities of the LSFL have been determined from the extracted profile of the pixel brightness and are given in Table 1.

Having the spatial period ~320 nm close to the incident wavelength (390 nm), the ripples are the LSFL. Comparing the LSFL formed for different expositions, Fig. 2(b) and (c), both shape and

Table 1
LSFL periodicities over number of samples.

Sample	Fig.	Number of pulses	Number of LSFL stripes	Periodicity
AlTi	2(b)	152×10^6	2	(~310 ± 20) nm
AlTi	2(c)	760×10^6	8	(314 ± 20) nm
AlTi	5(a)	$\sim 23 \times 10^9$ and scanning	68–70	(320 ± 20) nm
Al	5(b)	Scanning	>50	(~350 ± 20) nm
Al	3(a)	76×10^6	5–6	(~260 ± 20) nm
Al	3(b)	304×10^6	7–8	(~262 ± 20) nm
Al	3(c)	760×10^6	6–7	(~314 ± 20) nm

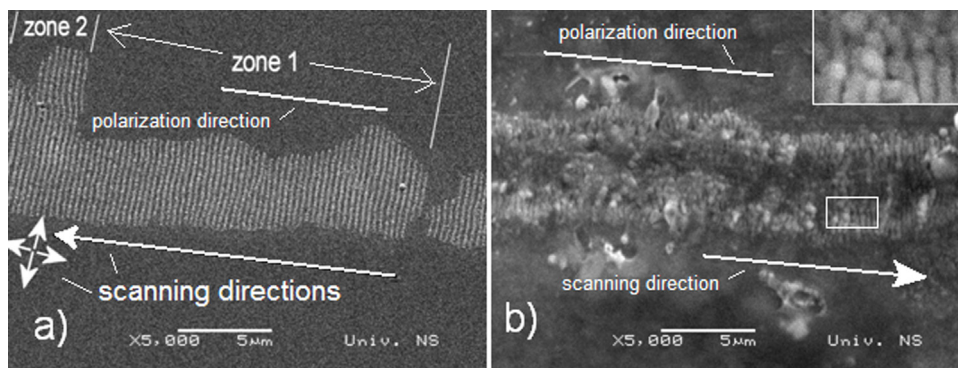**Fig. 5.** SEM micrograph of irradiated areas, white bar represents 5 μm, the samples were translated during the irradiation (arrows indicate the direction of beam traversing over the sample), exposition time ~300 s: (a) Al/Ti specimen, single pulse fluence 14 mJ/cm^2 (corresponding to 1.06 MW/cm^2); (b) Al thin film sample, 8.6 mJ/cm^2 (654 kW/cm^2). Inset in (b) shows enlarged part.

width of the LSFL seems to remain unchanged with exposition time. The ruffles are the precursor to the formation of the ripples – the strings of nanoparticles.

The specimen of the second type, the Al single layer thin film, was exposed to 8.6 mJ/cm^2 of the single pulse fluence and the same exposition times (for (a), (b) and (c), respectively) and the results are presented in Fig. 3. For 1 s of irradiation, Fig. 3(a), the material in the MA regrouped in the form of ripples. For longer exposition times, Fig. 3(b) and (c), ablation took part in the central part of the MA (dark spot) and ablated material accumulated around in the form of ripples (LSFL). The width of the ripples could be determined to ~200–220 nm and approximate spatial period to ~260–314 nm (Fig. 4). The ripples, with the direction perpendicular to the polarization direction of the beam, show lower regularity compared to the ones of the Al/Ti samples.

In order to see whether the relative movement between the laser beam and the samples influences the occurrence of the LSFL, the samples were slowly translated with estimated speed between 1 and 4 μm/s while exposed; the irradiation lasted ~300 s. For 14 mJ/cm^2 of the single pulse fluence (corresponding to 1.06 MW/cm^2), the Al/Ti sample was translated in parallel (Fig. 5(a), zone 1 arrow) and both perpendicular and parallel (Fig. 5(a), zone 2 arrows) directions in respect to the beam polarization direction. It is apparent that the arrangement of the LSFL is independent on the sample translation. This suggests that the interaction between the incident laser beam and induced surface wave [8,9], the surface plasmon polariton (SPP), together with dewetting [28,29] plays an important role in the formation of the LSFL. It should also be noted that, in spite of the long exposition times (~300 s while scanning), the disintegration of the LSFL has not occurred for the Al/Ti sample. From the extracted profile of the pixel brightness in Fig. 5(a), the spatial period of the LSFL has been determined to be (315 ± 20) nm. The sample was moved in such manner that the laser beam, after being switched on, first traversed over the sample in the direction to the left and stopped. The rightmost group of the stripes represents the position where the laser beam was shut off. Next movement of the sample positioned the beam for next ~2 μm to the left, where the sample stopped and the beam was switched on for ~300 s. While the laser beam still being switched on, the next movement with the speed of ~1–2 μm/s led the beam for next 10 μm (the long white arrow pointing to the left, Fig. 5(a)), along the polarization direction, where the sample stopped and the laser beam was left on for ~300 s. Without switching the laser beam off, the beam traversed (by sample movement) to the left (the long white arrow pointing to the left) with speed ~3–4 μm/s for next 10 μm, entered the zone 2, stopped and left for ~300 s. The discrepancies in the thickness of the ripple trace might come for the reasons of the speed instability of the sample movement. Then the beam traversed with ~2 μm/s in the direction of the small up-pointing arrow for 5 μm, then back down for ~5 μm, then to the left ~5 μm and in the end back to the right and stopped, remaining in the zone 2 for ~300 s. In all cases of the movement, the polarization direction was as shown in the Fig. 5(a), i.e. horizontal.

The implementation of the low single pulse fluences (~14 mJ/cm^2, corresponding to 1.06 MW/cm^2) enables the generation of permanent high-quality LSFL tracks (ripple trace) on the multilayer film for the length of ~20 μm, indicating the potential of LSFL fabrication, covering of large surface areas without loss of quality. This is in contrast to the case of the Al single layer sample, where obtained LSFL structure is loose and contains bifurcations (Fig. 5(b)). The sample was translated along the polarization direction (arrow in the Fig. 5(b), with the scanning speed of 5 μm/s. The LSFL are less prominent, but still noticeable – see inset in Fig. 5(b). Fig. 5 demonstrates that the regularity of LSFL is highly improved with using the multilayer configuration.

Table 2
EDS analysis (in weight %) of non-irradiated area and modified area (MA) irradiated with single pulse fluence of 14 mJ/cm^2.

Element (%)	Non-irradiated area	MA during 1 s	MA during 300 s
Si	88.6	70.72	51.33
Al	3.58	3.05	2.17
Ti	8.36	6.52	4.53
N	0	19.70	31.25
O	0	0	10.72

The influence of the femtosecond laser beam irradiation to the chemical modification of the surface has been investigated. The adsorption of N into Al surface under the irradiation of femtosecond laser pulses has been reported [21]. In Table 2, the EDS results obtained from three spots of the Al/Ti sample are presented: (1) from non-irradiated area (unmodified surface), (2) from MA irradiated with 14 mJ/cm^2 single pulse fluence during 1 s (corresponding to 1.06 MW/cm^2) – where only the HSFL-like noise appeared, and (3) from MA irradiated with 14 mJ/cm^2 single pulse fluence during 300 s (corresponding to 1.06 MW/cm^2) – where the LSFL appeared. The results after short exposures show the appearance of N, but not of O in the MA. The results of longer exposition, where the LSFL occurred, show the increased content of N and the occurrence of O in the MA. The adsorption of N is likely to occur for shorter exposition times (smaller accumulated energies), while additional oxides appear for longer exposition times (greater accumulated energies). Due to the constraints of the EDS (spatial resolution, i.e. great volume from which the information is obtained, and the detection from the deep of the interaction volume) neither oxygen nor nitrogen has been detected in non-irradiated spots. Their common presence (particularly of natural oxides) is of much lower contribution compared to irradiated spots.

The profile of structures developed on irradiated multilayer 5× (Al/Ti)/Si sample, together with 2D FFT (see Fig. 2), is shown as the AFM images in Fig. 6. The irradiation by 14 mJ/cm^2 during 2 s (corresponding to 1.06 MW/cm^2) changes the surface RMS roughness from 0.5 nm (in non-irradiated area, mirror-like surface) [23] to 6.8 nm (HSFL). The existence of the periodicity could be determined from the 2D FFT image, Fig. 6(c), where the orders are linked to periodicities of LSFL (1st order) and also to HSFL-like ruffles (2nd order), which approximate value of ~130 nm could be estimated from Fig. 6(b). Moreover, in the central part, the height of the LSFL reached a value of about (45 ± 0.5) nm above the mean. On the other hand, the irradiation during 10 s produced a clearly regular periodic topography of eight ripples (Fig. 2(c), AFM images with 2D FFT and profile in Fig. 7). The average ripple height given by the AFM in Fig. 7 is 45 nm above the mean, which is similar to the height after 2 s of irradiation (Fig. 6). This may lead to the conclusion that the height of the LSFL is not influenced by the exposition time; increasing time of laser irradiation only increases the number of the LSFL inside the MA. The SEM and AFM images indicate that each ripple has a fine granular structure (the average granule size is about 130 nm), which could be attributed to the formation and self-arranging of nanoparticles. The growth of the LSFL could also be explained by considerable nitriding and oxidation of the sample material [28,30–34] with possible forming of intermetallic mixture of Al and Ti [35].

The penetration depth, l_α, for the 390 nm laser beam in Al is about 3 nm, and in Ti is about 9.3 nm, calculated by using the formula [3] $l_\alpha = 1/\alpha = \lambda/4\pi\kappa$, for picosecond pulses [23,35,36], where λ is a laser beam wavelength, α is an absorption coefficient and κ is an extinction coefficient.

There are various explanations of the occurrence of nanostructures (ripples) on the surfaces irradiated by laser beam depending on the laser type, beam characteristics (repetition rate, wavelength, power . . .) and the target material. The generation and evolution
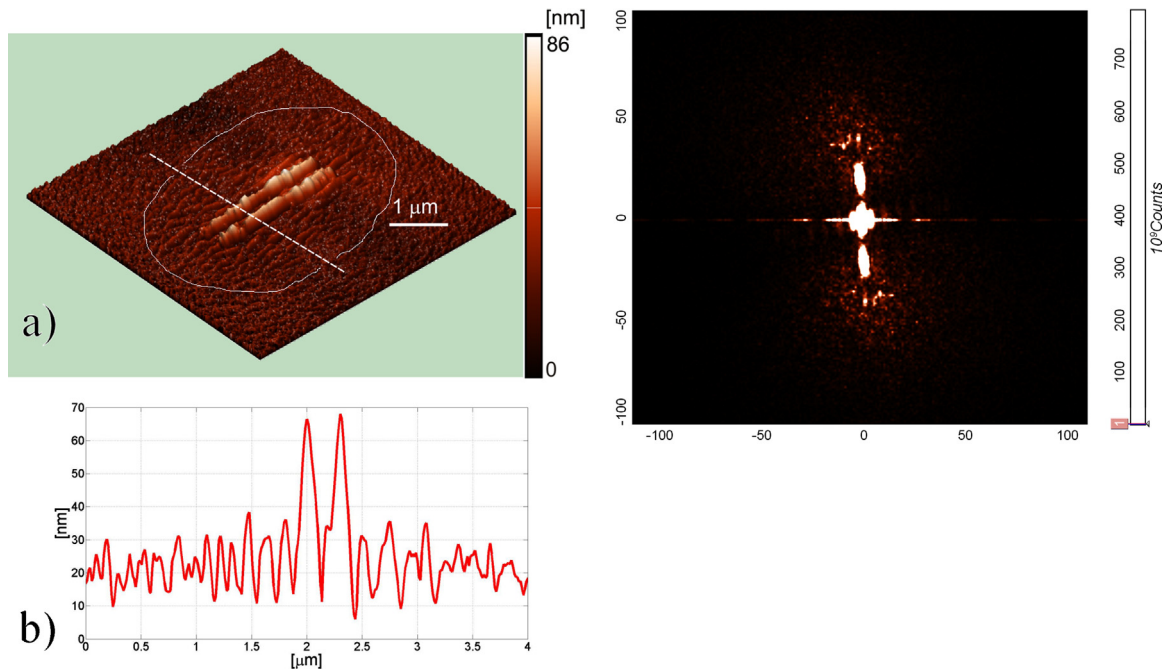
Fig. 6. (a) AFM micrograph of the irradiated spot (SEM presented in Fig. 2(b)): single pulse fluence 14 mJ/cm^2, exposition time 2 s (corresponding to 1.06 MW/cm^2); (b) profile along the dashed line, captured by AFM; (c) 2D FFT of the area shown in (a).

of the LSFL as surface ripples on metals (Pt, Ag, Au, Cu, W) under the irradiation of femtosecond beam of 160–480 mJ/cm^2 fluences and small repetition rates (1 kHz) have been reported in Refs. [7–9], showing that the incident wavelength influences the periodicity of the LSFL and that the LSFL gradually disappear in the central area of the spot for further increase of the number of shots. Our SEM analysis has shown that the beam of ∼10.3 mJ/cm^2 single pulse fluence (corresponding to 783 kW/cm^2) induced the occurrence of small-amplitude ruffles, the HSFL-like noise, on the Al/Ti samples. The beams of both 13.6 and 14 mJ/cm^2 (1.03 and 1.06 MW/cm^2, respectively) induced the occurrence of the HSFL-like noise for shorter exposition times and the LSFL for longer exposition times. It could be concluded from Fig. 7(b) that the number of the LSFL (ripples) increased with the increase of the exposition time while their width and height did not change. The damage threshold of the Al topmost layer is increased and the surface electron temperature is decreased due to the presence of the Ti underlayer. The lattice temperature is formed through the interplay between two competing mechanisms: electron–phonon (which induces heat localization) and carrier transport linked to the electron heat conductivity (which transfers heat away from the laser-exited region) [37]. The difference in electron–phonon coupling between the two materials leads to the steep change of the lattice temperature inside the inner (Ti) layer. Top layer electrons can quickly transfer energy to the next inner layer (Ti). In this way thermal energy is transmitted through the Al/Ti interface, it is then coupled to the lattice and transferred away from the interaction zone [38]. On the other hand, when the ratio between the interpulse time (∼13 ns in our case) and pulse duration (∼150 fs in our case) is more than five, more energy from the surface is available to be transferred towards the lattice before it dissipates to the bulk through transport mechanisms. For even greater ratio, mass removal and phase transition are less pronounced. This could be one of the possible causes of the material regrouping in the form of ruffles/ripples on the surface of Al/Ti system without ablation [39].

For the Al samples, the LSFL also occurred with similar spatial period close to the irradiation wavelength. However, the LSFL show much better regularity in Al/Ti samples compared to the single Al films, that is most probably linked to the presence of the Ti layers in the target. Ablated material re-deposited around the ablation zone in the form of ripples (LSFL). For longer expositions, Fig. 3(c), total accumulated energy prevented the regular formation of the ripples. If compared to the Al/Ti case, the absence of the underlayer (Ti) in the single Al layer case has the result that the temperature of the top layer lattice is not reduced and in that way the damage threshold is not increased [38].

Single pulse ablation threshold for various materials at applied wavelength depends on the surface reflectivity, which in turn depends on the number of accumulated pulses. Also, substantial heat accumulation should take place for very high repetition rate, providing decrease of the ablation/melting threshold. For the mirror-like surface the ablation threshold should be slightly higher. Following our results, the evolution of the surface morphology could be explained. The laser beam changes the initial random-ruffle state of the surface in the way that initial ruffles evolve into the HSFL-like noise. For higher fluences the HSFL amplitude is higher. If the fluence is above the threshold of ∼13 mJ/cm^2, corresponding to 988 kW/cm^2, the primary condition for the occurrence of the LSFL is met. The exposition time is the secondary condition for the LSFL generation. Thus, for the values above the threshold, the exposition time of ∼2 s (corresponding to ∼150 million pulses) is required for the generation of the LSFL (in the form of the strings of nanoparticles), which is the cumulative effect. Possible explanation is that there is a fluence threshold for the LSFL formation and – moreover – that there exists the threshold in the number of pulses, effective if the fluence threshold is reached.

Our results show that the beam induces the formation of nanoparticles and their clusters, which regroup or redeposit on the surface in the shape of the string of nanoparticles (the LSFL). The possible driving mechanism in multilayer system may be dewetting upon melting [28,29]. Also, dewetting possibly may occur only in external Al layer, and continue to lower layers. Due to heat accumulation effect, the ablation occurred in single layer configuration. Absence of the ablation in the multilayer sample could be possibly caused by dewetting. According to the measurements (Fig. 6), the LSFL are grown well above the initial surface that can be explained
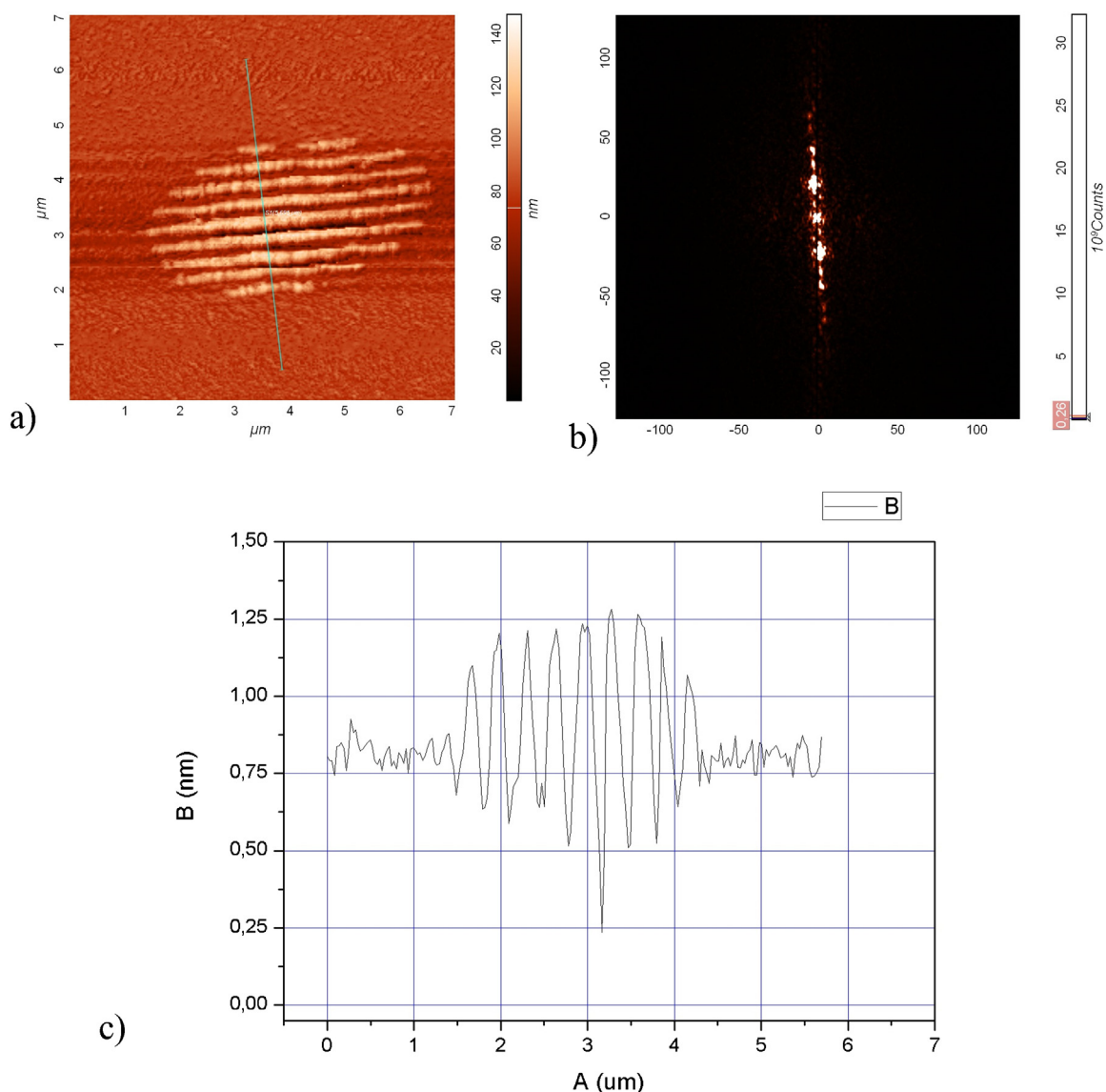
Fig. 7. (a) AFM micrograph of the irradiated spot (SEM presented in Fig. 2(c)): single pulse fluence 13.6 mJ/cm^2 and 10 s exposition time (1.03 MW/cm^2); (b) profile along the dashed line, captured by AFM; (c) 2D FFT of the area shown in (a).

by considerable nitriding and oxidation of the material in the irradiated zone (consuming material not only from the sample depth but also from atmosphere) [28]. However, dewetting is not pronounced for single Al layer system of thickness >100 nm.

The dimensions of the individual nanoparticles were in the interval from ~50 to ~150 nm. In the periphery of the MA, that is, in the boundaries of the Gaussian laser beam profile, lower fluence on the Al/Ti target generates nanoparticles of smaller dimension. In the Al single layer sample, Fig. 3(a), the nanoparticles disintegrated (due to melting) and the LSFL formed. In both the Al/Ti and Al single layer samples, the LSFL were most probably caused by the surface plasmon polariton (SPP).

The subwavelength spatial period of the LSFL seems to be dependent on the implemented wavelength. The period of 280 nm was obtained for the laser light at 400 nm, and of 542 nm for the 800 nm laser light [9]. Taking into consideration the previous investigations of the generation, evolution and disintegration of the LSFL under high fluences, low repetition rates and specific wavelengths, one could see different explanations for their occurrence, pointing to various causes, but the most probable is the interaction between the incoming beam and induced surface wave [9,12,40–41]. In spite

of using low fluences, our results are consistent with [9], which suggests similar causes of the LSFL generation. It is possible with low-fluence beam – with high repetition rates – to generate HSFL on the irradiated surface, and to induce and control their evolution to the LSFL (subwavelength fs-LIPSS). Moreover, the implementation of low fluence will preserve the LSFL from disintegration even after the great number of pulses, Fig. 5(a). The dielectric constant variation leads to the increase of the optical penetration depth [16,37]. Compared to the Al/Ti multilayer case, the optical penetration depth in the single Al layer case is lower, having higher values of heat accumulation (and absorbed energy) as a consequence. Melting and ablation is induced and more pronounced, and the ruffle/ripple structure is formed. On the other hand, in the Al/Ti multilayer case, the dielectric constant of Ti leads to different values of optical penetration depth and absorbed energy, which means that the mechanism of ruffle/ripple formation is different due to the presence of the Ti layer. Also, due to higher concentration of the laser-induced carriers in single Al layer case, the ripple structure periodicity is lower compared to the Al/Ti case. In the Al/Ti case, the observed monotonicity of the ripple period could be attributed to the constant value of the laser-induced carrier concentration [16].

Moreover, two competing forces (recoil and surface tension) would squeeze the originally produced profile and therefore decrease the period [39]. The presence of Ti underlayer would affect the squeezing, resulting in different values of the periodicity for the two cases (single layer Al and multilayer Al/Ti).

4. Conclusion

The study of surface modifications induced at two types of thin films – five (Al/Ti) bilayers (total thickness of 130 nm) on Si as well as Al single layer (130 nm thickness) on Si – by femtosecond laser beam at 390 nm and repetition rate of 76 MHz ($\sim$13 ns of interpulse time), is presented. Morphological changes of the surface were induced with single pulse fluences of 10.3–14 mJ/cm^2 in Al/Ti multilayer samples and with 8.6 mJ/cm^2 in Al single layer samples. We have shown that the fs-LIPSS occur as periodic strings of both nanoparticles and nanoparticle clusers (LSFL) and can be generated on the surface if both the fluence and the exposure time are above certain thresholds. For Al/Ti multilayered thin film, the threshold single pulse fluence is 13 mJ/cm^2 and the exposure time should be $\geq$2 s. While – at this relatively low-fluence regime – shape, height and width of the strings show no dependence on the exposure time, the number of strings of this permanent grating strictly depends on it. We can generate different numbers of lines of this permanent grating by varying the exposure time. We achieved high-quality highly-controllable production of surface periodic structures on nanosized multilayer films with high-repetition-rate low-fluence femtosecond laser pulses.

The LSFL formation could be explained by regrouping of the material under the influence of the SPP. The subwavelength spacing (periodicity) is different for the two cases, the Al single layer and the Al/Ti multilayer, due to the presence of the Ti underlayer. For Al thin film samples, the ablation occurred in the central part of the irradiation area and the material deposited around in the form of the LSFL. The regularity of the ripples (LSFL) is higher at the surface of the Al/Ti multilayer samples due to the presence of the Ti underlayer. The LSFL occurring in laser-based nanopatterning processes could be of interest – for example – in medical, tribological, photovoltaic or decorative applications.

Acknowledgments

References

[1] H.M. van Driel, J.E. Sipe, J.F. Young, Laser-induced periodic surface structure on solids: a universal phenomenon, Phys. Rev. Lett. 49 (1982) 1955–1958.

[2] J.E. Sipe, J.F. Young, J.S. Preston, H.M. van Driel, Laser-induced periodic surface structure. I. Theory, Phys. Rev. B 27 (1983) 1141–1154.

[3] D. Bauerle, Laser Processing and Chemistry, Springer, Berlin, 2000.

[4] J.F. Young, J.E. Sipe, H.M. van Driel, Laser-induced periodic surface structure. III. Fluence regimes, the role of feedback, and details of the induced topography in germanium, Phys. Rev. B 30 (1984) 2001–2015.

[5] I. Ursu, I.N. Mihăilescu, A.M. Prokhorov, V.I. Konov, V.N. Tokarev, On the role of the periodical structures induced by powerful laser irradiation of metallic surfaces in the energy coupling process, Physica B + C 132 (1985) 395–402.

[6] W. Kautek, P. Rudolph, G. Daminelli, J. Krüger, Physico-chemical aspects of femtosecond-pulse-laser-induced surface nanostructures, Appl. Phys. A 81 (2005) 65–70.

[7] J. Wang, C. Guo, Ultrafast dynamics of femtosecond laser-induced periodic surface pattern formation on metals, Appl. Phys. Lett. 87 (2005) 251914(3).

[8] A.Y. Vorobyev, V.S. Makin, C. Guo, Periodic ordering of random surface nanostructures induced by femtosecond laser pulses on metals, J. Appl. Phys. 101 (2007) 034903(4).

[9] A.Y. Vorobyev, C. Guo, Femtosecond laser-induced periodic surface structure formation on tungsten, J. Appl. Phys. 104 (2008) 063523(3).

[10] M.S. Trtica, B.B. Radak, B.M. Gakovic, D.S. Milovanovic, D. Batani, T. Desai, Surface modifications of Ti6Al4V by a picosecond Nd:YAG laser, Laser Part. Beams 27 (2009) 85–90.

[11] D. von der Linde, K. Sokolowski-Tinten, J. Bialkowski, Laser–solid interaction in the femtosecond time regime, Appl. Surf. Sci. 109–110 (1997) 1–10.

[12] J. Bonse, A. Rosenfeld, J. Krüger, Implications of transient changes of optical and surface properties of solids during femtosecond laser pulse irradiation to the formation of laser-induced periodic surface structures, Appl. Surf. Sci. 257 (2011) 5420–5423.

[13] H. Mochizuki, W. Watanabe, Y. Ozeki, K. Itoh, K. Matsuda, S. Hirono, Fabrication of diffractive optical elements inside polymers by femtosecond laser irradiation, Thin Solid Films 518 (2009) 714–718.

[14] B. Gakovic, C. Radu, M. Zamfirescu, B. Radak, M. Trtica, S. Petrovic, P. Panjan, F. Zupanic, C. Ristoscu, I.N. Mihailescu, Femtosecond laser modification of multilayered TiAlN/TiN coating, Surf. Coat. Tech. 206 (2011) 411.

[15] J. Bonse, J. Krüger, Pulse number dependence of laser-induced periodic surface structures for femtosecond laser irradiation of silicon, J. Appl. Phys. 108 (2010) 034903(5).

[16] J. Bonse, J. Krüger, S. Höhm, A. Rosenfeld, Femtosecond laser-induced periodic surface structures, J. Laser Appl. 24 (2012), 042006 (7pp).

[17] McPherson, Inc. http://www.mcphersoninc.com/reflectivity.htm.(Accessed October 1, 2014).

[18] M. Bass (Ed.), Handbook of Optics, vol. 2, second ed., McGraw-Hill, NY, 1995.

[19] J.F. Young, J.S. Preston, H.M. van Driel, J.E. Sipe, Laser-induced periodic surface structure. II. Experiments on Ge, Si, Al and brass, Phys. Rev. B 27 (1983) 1155.

[20] Alumatter, by European Aluminium Association and MATTER Project at the University of Liverpool, UK, http://aluminium.matter.org.uk/content/html/eng/default.asp?catid=197&pageid=2144416839 (Accessed: October 1, 2014).

[21] X. Li, C. Yuan, H. Yang, J. Li, W. Huang, D. Tan, Q. Hu, Morphology and composition on Al surface irradiated by femtosecond laser pulses, Appl. Surf. Sci. 256 (2010) 4344–4349.

[22] N. Yasumaru, K. Miyazaki, J. Kiuchi, Control of tribological properties of diamond-like carbon films with femtosecond-laser-induced nanostructuring, Appl. Surf. Sci. 254 (2008) 2364–2368.

[23] S.M. Petrović, D. Peruško, B. Salatić, I. Bogdanović-Radović, P. Panjan, B. Gaković, D. Pantelić, M. Trtica, B. Jelenković, Laser induced damage/ablation morphology on the 8(Al/Ti)/Si system in different ambient conditions, Opt. Laser Technol. 54 (2013) 22–29.

[24] Sh. Bashir, M.Sh. Rafique, W. Husinsky, Femtosecond laser-induced subwavelength ripples on Al, Si, CaF$_2$ and CR-39, Nucl. Instrum. Meth. B 275 (2012) 1–6.

[25] E.V. Golosov, V.I. Emel'yanov, A.A. Ionin, Yu.R. Kolobov, S.I. Kudryashov, A.E. Ligachev, Yu.N. Novoselov, L.V. Seleznev, D.V. Sinitsyn, Femtosecond laser writing of subwave one-dimensional quasiperiodic nanostructures on a titanium surface, JETP Lett. 90 (2009) 107–110.

[26] E.V. Golosov, A.A. Ionin, Yu.R. Kolobov, S.I. Kudryashov, A.E. Ligachev, S.V. Makarov, Yu.N. Novoselov, L.V. Seleznev, D.V. Sinitsyn, Formation of periodic nanostructures on aluminum surface by femtosecond laser pulses, Nanotechnol. Russ. 6 (2011) 237–243.

[27] A.Y. Vorobyev, C. Guo, Colorizing metals with femtosecond laser pulses, Appl. Phys. Lett. 92 (2008), 041914 (5pp).

[28] A. Sharma, R. Khanna, Pattern formating in unstable liquid films, Phys. Rev. Lett. 86 (1998) 3463–3466.

[29] A. Herz, D. Wang, Th. Kups, P. Schaaf, Solid-state dewetting of Au/Ni bilayers: the effect of alloying on morphology evolution, J. Appl. Phys. 116 (2014), 044307 (7pp).

[30] B.E. Deal, A.S. Grove, General relationship for the thermal oxidation of silicon, J. Appl. Phys. 36 (1965) 3770–3778.

[31] E. Sicard, C. Boulmer-Leborgne, T. Sauvage, Excimer laser induced surface nitriding of aluminium alloy, Appl. Surf. Sci. 127–129 (1998) 726–730.

[32] T. Aubert, M.B. Assouar, O. Legrani, O. Elmazria, C. Tiusan, S. Robert, Highly textured growth of AlN films on sapphire by magnetron sputtering for high temperature surface acoustic wave applications, J. Vac. Sci. Technol. A 29 (2011), 021010 (6pp).

[33] A.Gh. Bhuiyan, A. Hashimoto, A. Yamamoto, Indium nitride (InN): a review on growth, characterization, and properties, J. Appl. Phys. 94 (2003) 2779–2808.

[34] P. Schaaf, M. Han, K.-P. Lieb, E. Carpene, Laser nitriding of iron with laser pulses from femtosecond to nanosecond pulse duration, Appl. Phys. Lett. 80 (2002) 1091–1093.

[35] D. Peruško, S. Petrović, J. Kovač, Z. Stojanović, M. Panjan, M. Obradović, M. Milosavljević, Laser-induced formation of intermetallics in multi-layered Al/Ti nano-structures, J. Mater. Sci. 47 (2012) 4488–4495.

[36] D. Peruško, M. Čizmović, S. Petrović, Z. Siketić, M. Mitrić, P. Pelicon, G. Dražić, J. Kovač, V. Milinović, M. Milosavljević, Laser irradiation of nano-metric Al/Ti multilayers, Laser Phys. 23 (2013), 036005 (7pp).

[37] G. Tsibidis, Thermal response of double-layered metal films after ultrashort pulsed laser irradiation: the role of nonthermal electron dynamics, Appl. Phys. Lett. 104 (2014) 051603.

[38] A.M. Chen, H.F. Xu, Y.F. Jiang, L.Z. Sui, D.J. Ding, H. Liu, M.X. Jin, Modeling of femtosecond laser damage threshold on the two-layer metal films, Appl. Surf. Sci. 257 (2010) 1678–1683, and references therein.

[39] M. Barberoglou, G.D. Tsibidis, D. Gray, E. Magoulakis, C. Fotakis, E. Stratakis, P.A. Loukakos, The influence of ultra-fast temporal energy regulationon the morphology of Si surfaces through femtosecond doublepulse laser irradiation, Appl. Phys. A 113 (2013) 273–283.

[40] S. Sakabe, M. Hashida, S. Tokida, S. Namba, K. Okamuro, Mechanism for self-formation of periodic grating structures on a metal surface by a femtosecond laser pulse, Phys. Rev. B 79 (2009), 033409 (4pp).

[41] J. Bonse, A. Rosenfeld, J. Krüger, On the role of surface plasmonpolaritons in the formation of laser-induced periodic surface structures upon irradiation of silicon by femtosecond laser pulses, J. Appl. Phys. 106 (2009), 104910 (5pp).

M. M. Živanović, *et al.*: Influence of Electromagnetic and Nuclear Radiation ...
Nuclear Technology & Radiation Protection: Year 2017, Vol. 32, No. 1, pp. 91-98

91

INFLUENCE OF ELECTROMAGNETIC AND NUCLEAR RADIATION IN MEDICINE FOR THERAPY AND DIAGNOSIS THROUGH PROCESSES, FACTS AND STATISTICAL ANALYSIS

by

Monika M. ŽIVKOVIĆ [1,2], **Milesa Ž. SREĆKOVIĆ** [3],
Tomislav M. STOJIĆ [4], **and Bojana M. BOKIĆ** [5, 6*]

[1] Clinical Hospital Centre, Zemun, Belgrade, Serbia
[2] Medical Faculty, University of Belgrade, Belgrade, Serbia
[3] Faculty of Electrical Engineering, University of Belgrade, Belgrade, Serbia
[4] Faculty of Mechanical Engineering, University of Belgrade, Belgrade, Serbia
[5] Institute of Physics, University of Belgrade, Belgrade, Serbia
[6] Faculty of Physics, University of Belgrade, Belgrade, Serbia

Contemporary medicine (biomedicine) cannot be imagined without diagnostics and therapeutic methods based on nuclear, laser, acoustical and other processes. The application of these methods is linked to common computer support, signal processing, measuring monitoring techniques, high degree of automatization, and image analyses. The paper analysed contemporary technical issues related to neonatology, ophthalmology, based on the influence of nuclear radiation and laser beams. Some statistical processing and presentations of results obtained in the IGA KCS Hospital, Belgrade, Serbia, in curing vision of prenatal type newborns with a different degree of pathological state of retinopathy of prematurity are presented. The general conclusion is that, in spite of the good results, a multidisciplinary approach is needed for a deeper understanding of the role of lasers and laser techniques in medicine as well as possible couplings. Potential new applications of lasers important for the fields of neonatology and ophthalmology were also considered.

Key words: retinopathy of prematurity, neonatology, laser, nuclear radiation, damage, dosimetry

INTRODUCTION

Among diagnostic and therapeutic applications of electromagnetic (EM) and nuclear radiations in medicine, the basics are the mechanisms of beam interactions with material. Techniques of magnetic resonance (MR), tomography (nuclear and optical), holography with non-linear systems are the areas where the answers should be found. Not involving the mechanisms of nuclear magnetic resonance (NMR), the obtained signals and signal processing deserve specific attention, as well as the signal/noise (S/N) ratio, image generation, reconstruction, and selective excitation. Pulse sequences, the influence of microcentres moving, correction of moving through the image series, imaging flow, MR spectroscopy and system design are also of interest, too [1]. An approach to the new energy resources combines lasers and nuclear physics and techniques, as well as biology. This applies to therapy, diagnostics, for power sources through plants, bioconversion and biological sensors, as well as optical recording through bacteria. World catastrophes such as Chernobyl, accidents, Three Miles Island, Fukushima, provoke discussions about doses, caused biological effects of radiation and genetics (early and late effects). Unfortunately, new facts are provided through accidents in nuclear and laser technologies [2-14]. In tab. 1 the levels of radiobiological processes [9-13] are presented. Biological entities and hardness of organic/inorganic materials and systems are connected with doses with appropriate definition, measurements, uncertainties, as well as biological radiation effects [2-17]. Many theoretical models on various organization levels are developed. From the position of a systematic approach to the processes and modelling principles, concepts of biophysical models on molecular, genetic and cell levels are derived. Models should be compared and some investigations are in [13] regarding boundary conditions, applications and disadvantages. The probability estimation through many criteria should follow the analysis for their inves-
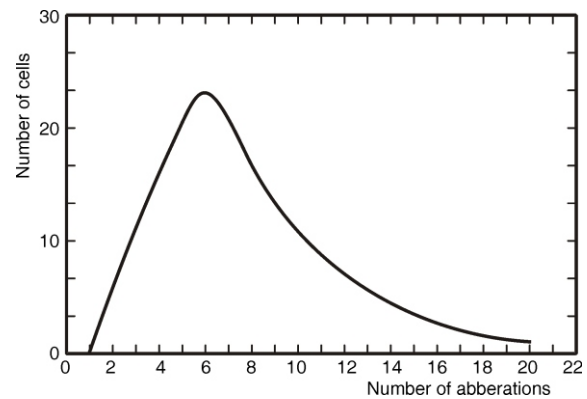
92

M. M. Živanović, *et al*.: Influence of Electromagnetic and Nuclear Radiation ...
Nuclear Technology & Radiation Protection: Year 2017, Vol. 32, No. 1, pp. 91-98

Table 1. Levels of processes in biology caused by radiation

Level	Existence time on level [s]	Processes on the presented level; possible modifications
Physical	10^{-18}-10^{-8}	Excitation, ionisation, elastic collisions-thermalization and formation of high reactivity radicals of macromolecules and short lived free radicals of water and organic molecules; no modification
Chemical	10^{-14}-10^{-4}	Reactions of free radicals mutually, with organelles – forming primary damage (DNA damages, dimerizations); modification by protector, oxygen, temperature
Biochemical (subcell)	10^{-4}-10^{5}	Reparation, interactions of damaged microcenters (mutation, aberration, modification by temperature and other agents)
Biological (cellular)	10^{3}-10^{7}	Division of cells and molecular chains, exchange of performances as a result of mutations

Figure 1. Chromosome aberration for lymphocytes irradiated: moderate neutrons (0.35 MeV; 3.3 Gr)

Figure 2. Aberrations of cells *vs*. the neutron dose (0.35 MeV (1), 0.85 MeV (2), and for γ radiations of ^{60}Co (3)

Figure 3. Frequency of changed barley seeds (type Nadya) in the case of combined radiation of gamma rays and frequency doubled ruby laser (347 nm)

tigation and experimental assessment. Theoretical approaches and results based on appropriate formalisms are of importance in the field of radiation protection and dosimetry, which are constantly competing due to new sources in radiology. Molecular biology (for structure, DNA functioning and repair processes), uses only the simplest biological effects (inactivations of phages, viruses, and gene-mutations). The explanation through complex biological processes and behaviour could rather remain without results. The cell inactivation model based on physical considerations, and later models as radiobiological ones (on the genetic level without the existence of repair processes and chromosome structures) are developed. Self-repair, interactions of damages, dynamics of the processes, stochastic energy transfer to the cells are also important topics. Micro dosimetry, the structure of the cell traces, stochastics, classification and conceptual analyses appeared as typical. Characteristics of physical models, the theory of dual effect, and modifications are compared. They include the radiobiological effects to DNA and model of cell /systems inactivation. It is important to implement physical doses, target theories and modifications. The two-component dual effect model of probability on molecular and genetic levels (*E. coli* mutations and mammals) deals with various effects (lymphocytes irradiated by neutrons). Table 1, figs. 1-2 based on results [13] show some trends in modelling and experimental irradiations of different cells and aberrations. Figure 3 presents the qualitative behaviour of different beams and radiation on plants.

Sensitivity of mammal cells to the irradiation of heavy ions depending on the viability level (or survival) of the human and animal cells, (lymphocytes, diploid fibroblasts, and kidney cells) are studied [13]. The defined threshold for survival as well as energy loss per range of ions are parameters of interest.
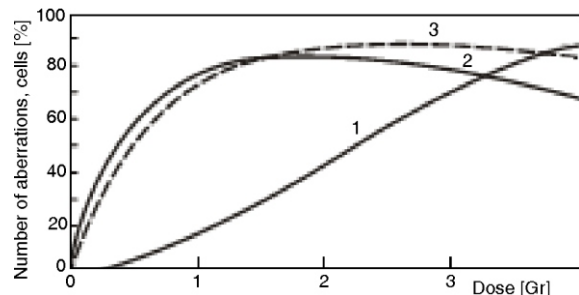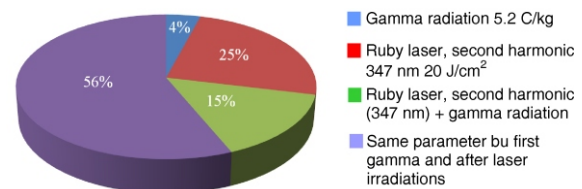
The same goes for sensitivity of the mammalian cells to the irradiation of ions, induced number of structural changes after X-ray irradiation of the tumour cell *vs*. dose. Models of: inactivation, Karposs and Foloty, repaired and unrepaired damages include/(do not include) saturation processes, viability of prokaryotes, sensibility of *E. coli* to neutrons, eukaryotes, and fatal damages. Thermal damage and critical temperatures, threshold for effects and concentration limits are important. Couplings between the nuclear power engineering, laser technique and medicine are multiple (some are connected by the laser excitations in the nuclear reactions and pumping neutrons, protons, α and β radiations). Modern problems include gamma and X-rasers (X-ray Amplification by Stimulated Emission of Radiation), or preionizations to decrease the lasing threshold, but also for disposal of various waste.

M. M. Živanović, *et al.*: Influence of Electromagnetic and Nuclear Radiation ...
Nuclear Technology & Radiation Protection: Year 2017, Vol. 32, No. 1, pp. 91-98

93

The biological damage threshold is studied for various cell types and systems. An epidemiological study and variation of estimated doses and the real damage are the subjects of a wide investigation in the theory of microdosimetric cellular radiobiological action, lymphocytes and stochastic/astochastic effects.

Considering vision, in the sense of colour prejudice in various problems, it should start from the primary eye functions and its mechanisms. Medically speaking, there are numerous links between ophthalmology, neonatology and lasers techniques. Diagnostic techniques and operatives, including biostimulative treatments with lasers penetrated into many branches of medicine and could be applied for many tissues and organs. There are two phenomena where we have to stay in one of the natural organs which is the eye: structure complexity and simple functioning, describe modern problems for techniques-medicine-protection couplings and tasks. Since the first application of lasers in medicine, the area of application has significantly expanded, in eye surgery and diagnostics. Medical terminology and diagnostics are expressed through quantitative indicators for biomaterial and generalized processes. Modern methods of coherent, linear and nonlinear optics, have to be involved in the world of medical diagnostics and monitoring. The dynamics of human and animal cells, protoplazmatic and blood circulation, tissue pathology, could be observed due to the development of photon beating and Laser Doppler Anemometry (LDA) techniques.

The paper intends to show the role of lasers in diagnostics, gynaecology and ophthalmology. Vision problems incurred in neonatal infants, require a complete diagnosis and medical history. Similar types of lasers are used both in diagnostic and operative treatments. The treatments differ in accessories, but essentially, models of interaction and diagnosis are associated with many of the general applications, where optical beams have the role of a knife (scalpel), therapy or diagnosis. Sources are beams of coherent radiation in the visible, infra red (IR), far infra red (FIR) or ultra violet (UV) portion of the EM spectra. The study of the ocular performances has come a long way from the first images of muscle tissue and Helmholtz's assumption up to the present, with computer diagnostics, polarizing microscope, Stokes parameters and Mueller matrices [12].

Besides many diagnostic techniques in ophthalmology, some of the relevant laser techniques of interest to several branches of medicine are analysed. One of them is used for the early diagnosis of glaucoma. The solutions appeared based on methods: (a) Laser Induced Fluorescence (LIF) and (b) monitoring of the Stokes parameters through ellipsometric measurement [7, 12]. Fluorescence methods were not new in medicine, however, Raman, IR and UV spectroscopies and new areas of nonlinear laser spectroscopies with tunable lasers, made precise application possible. Measurements of turbidity belong to the category of reliable, but less accurate measurements. Harmonics of the Nd^{3+}: YAG (yttrium aluminium garnet) laser are favourable for biosamples in the picosecond (ps)-region (in mastitis tissue diagnosis).

The eye system is well studied in the linear region. There is data available on absorption of the eye and its constituents, spectral sensitivity curves relative spectral brightness and eye adaptation to the light vision (photopic and scotopic). However, the variety of eye-damages existed even before the use of lasers. Damages occurred in the process of welding, by the focused radiation of the sun and sources in other portions of the EM spectrum. Nowadays most of the relevant data concerning laser (laser era) damage originate from accidents. With the first giant laser pulses, it was possible to organize the study of nonlinear effects. The first ophthalmic devices applied on to rabbits appear as new experimental material. The people working in space and next to the terrestrial accelerator devices are experiencing sparkles of light due to the environment of cosmic and gamma rays. Absorption of the photopigments in human eye receptors (cones and rods), versus different wavelengths was studied. Saturation effects were likewise found [18]. Data of the normalized absorbance of the photoreceptors, or photopigment molecules, are obtained through microphotometry methods, and further investigations explained the human feeling for colours. Main data comparison between the physics, metrics of colours, and psychological concepts can be a subject of discussion.

RETINOPATHY OF PREMATURITY INCIDENCE IN THE IGA KCS HOSPITAL

Important topics in the field of neonatology are retinopathy of prematurity (ROP) and risk factors. In the light of new methods for treating ROP, comprehensive theoretical and experimental support is needed and it requires a multidisciplinary approach. Optical methods in diagnosis and treatment, light influence on the eye systems, damage threshold, scattering and absorption processes are of interest. Lasers and fiberoptics are also unavoidable topics in ophthalmology. Laser surgery is rivalled by the cryo-surgery technique, but for the moment it seems that lasers have more advantages. The institutional procedure with questionnaires for parents before the intervention in cases of ROP can be found on the internet. Many questions exist concerning ROP progress, laser treatments, complications and measures of protection.

Laser methods and hazards

Laser surgery for cases of ROP is actually causing partial damage to the ischemic retina. We will not describe the processes on a microscopic level con-

94

M. M. Živanović, *et al.*: Influence of Electromagnetic and Nuclear Radiation ...
Nuclear Technology & Radiation Protection: Year 2017, Vol. 32, No. 1, pp. 91-98

nected to ribonucleic acid (RNA), process of peripheral retinal vascularization and other important factors. Destruction of ischemic retina can be performed with various laser types: Ar $^+$: ion (488-515 nm; 200 mW, in the appropriate regime) or semiconductor laser (IR range, 810 nm). The binocular microscope – ophthalmoscope, is the second necessary component, and the systems for beam positioning and shaping with the low power He-Ne laser. Various reference data confirms the positive outcome with the different laser types and details about advantages and disadvantages of the ROP laser treatment [19-24]. Reduced vascularisation can be observed 7 days after the intervention (photocoagulation). A detailed database should be made for both lasers and cryogenics, which is necessary for decision making and analysing the laser ROP treatment compared to other techniques. Perhaps it is important to note that for now the χ^2 test gives no significant difference method.

Regulations, ecology and laser (eye and skin damage)

The application of lasers in everyday life, biology, ecology, medicine, pharmacy and military is related to many administrative regulations worldwide that vary in different countries. In particular, principal parameters and protections are defined. Nominal Ocular Hazard Distance (NOHD) was one of the first regulated definitions. The classification of lasers varies from one state to another, however most countries share the same regulation. The lasers are classified into four groups, assuming that both the III class as well the IV class would lead to laser induced damage. Therefore many investigations of laser influence on animal eyes and plants were performed including the investigation of the impact of various environmental conditions (fog, smoke, and fume), using different chemical products. The threshold for laser damage depends on the different parameters of investigated bio-objects, (biomaterials, biotargets) and pupil size; quantitative presentation of those investigations is connected to protection and regulation for selected lasers and working regimes. Therefore relevant data of transparent, absorptive, parts of the ocular performances are needed. Absorption of EM radiation in the eye deals with four principal bands: (a) Microwaves and γ rays. (b) Far UV and FIR, (c) Near (N) UV, (d) Visible and NIR regions.

There are four categories of laser (equipment) interactions with tissue: (a) optical radiation hazards to the eye and skin, (b) chemical, (c) electrical, and (d) casual hazards [4]. Most of the Nd^{3+}: YAG laser beam energy is absorbed inside the optical structure of the eye (cornea, lens and vitreous). Note that this laser type is also used in everyday applications in ophthalmology and other branches of medicine. The retinal

effects are expected in the visible and close IR-A case (400-1400 nm). Minimal sizes of the image on the retina depend on wavelength and are limited by diffraction. Radiation in the UV or FIR portion of the spectra is absorbed in the inner part of the eye. High levels of exposure can permanently damage the cornea or lens. Medium levels of the UV beams cause serious damage, which is severe but temporary (analogue to industrial welder flash, *i. e.* photokeratitis). Description of the biological effects of radiation, according to the International Commission on Illumination (CIE), is performed in 7 spectral bands 4].

Skin damage is far less likely to occur, except in cases of high-power lasers. The skin is usually not injured by common lasers, *i. e.* low and medium power lasers. Levels of skin injuries visible and IR areas require at least a few Wcm^{-2}, and depend on the skin's surface characteristics [4]; exposure conditions are presented by dosimetry (a laser can be viewed as a thermal damage source). Radiation (200-300 nm) causes burns, the same as those caused by the sun (cancer, erythema). Electrical hazards will not be described in detail, however a source of high voltage present in lasers, can provoke electric shock resulting in electro-cauterisation. Therefore appropriate electrical and electronic standards have to be applied. Considering standards and regulations in chemistry, many highly volatile or even explosive or highly toxic materials are used in laser laboratories. During laser processing of a material (welding/cutting) much chemical evaporation is created. Standards for industrial manufacturing require adequate ventilation during the laser operation. Items connected to retina treatment risks (injuries) are: blue/UV light, retinal image, retinal burns, intensity and spectral characteristics of coherent sources.

ROP is the subject of research in many clinics worldwide, as well as in Serbia. For this type of study, trained teams, originating from various branches of expertise (beside experts in gynaecology and ophthalmology) are needed. As ROP presents a disorder of retinal blood vessel development in prematurely born infants, it can be interrupted by laser beam interactions with tissue. The process can affect the vitreous body and lead to detachment of the retina. In the most severe ROP forms, it leads to partial retinal detachment. This can cause blindness in childhood and is considered to be one of the main causes. We will consider some of the important approaches in ROP diagnostics and treatment. ROP was mentioned for the first time in 1942, and has been regularly mentioned to this day. Various methods of operation have been attempted during almost three quarters of a century. It was identified as a fibrous state process of the retina and vitreous body (retrolental fibroplasia). The correlation between these processes and prematurity of childbirth was established. The name ROP (1952.) was first mentioned in the middle of the last century. The study of

pathogenesis was enhanced through development of the animal models. The International Classification of Retinopathy Prematurity – ICROP has been formed over time. It represents an important and unifying criterion for the diagnosis and treatment of active forms of ROP. Screening, monitoring and treatment of ROP are implemented in several countries. In Serbia, since May 2003, many cases of ROP, as an active disease, have been diagnosed. In Belgrade, Serbia, the IGA KCS hospital initiated systematic ophthalmological examinations. The method of using an indirect ophthalmoscope, provided an early diagnosis of disease, and monitoring of severe forms of active retinopathy.

Parameters and stages of ROP

Various stages of the disease are described [20, 22, 25-29]. The zone of interest is divided into the central area of growth in the retina, which encompasses the macula, the highest ROP and the last area of growth. Different descriptions and classifications of the main parameters of ICROP exist. Most of them agree that the most important parameters are: severity (pathological mutation) with different stages, localization with 3 characteristic zones, prevalence – number of hours, tab. 2, and fig. 4.

RESULTS OF ANALYSIS

The results of the study of ROP should in principle be related to the frequency of prevalence and the appropriate time of observation in order to obtain the data that have sufficient statistical importance. In the analysis, several factors are included: prematurity time, birth weight (small weight at birth), hyperoxia and oxygeno therapy duration, sepsis, respiratory diseases, coherent/incoherent EM irradiation. Figure 5 represents the percentage display of the data on the numbers of births and treatments applied. Percentage data are related to several hundreds of prematurely

Table 2. Stages of retinopathy

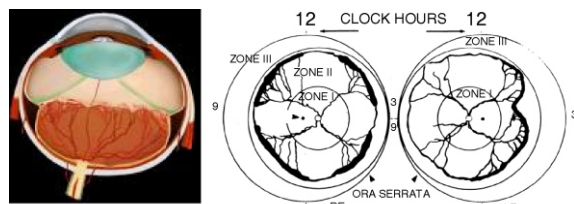| 1 stage	Normal but incomplete growth
2 stage	Medium abnormal growth
3 stage	Very abnormal growth
4 stage	Partially detached retina
5 stage	Retina with entirely detached retina

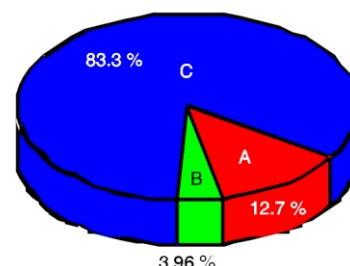**Figure 4. Typical stages of ROP and eye anatomy [30]**

Figure 5. Percentage display of early childbirth with different final outcomes – transferred to another institution, fatal and treated in the maternity hospital and allowed to go home

Table 3. Incidence of ROP related to weight at birth in 2004

Incidence of ROP	Number [%]
<999 g	3 newborns [0.52 %]
1000-1499 g	13 newborns [2.2 %]
1500-1999 g	7 newborns [1.19 %]

born infants; therefrom, the cases of ROP are present in a few percents (~4 %). Table 3 covers the number of data with respect to the weight. In figs. 6-10 the results of the study are graphically presented.

Prematurely born infants or infants with low body weight are the most indicated groups for ROP, however only a small percentage of them end up with a severe form of the disorder.

Ophthalmologic results of the examined children despite the risk for retrolental fibroplasia, were within normal limits, with no statistically significant differences compared to the reference values, $-p > 0.05$ (DF = 67, $t = 0.2371$), [21].
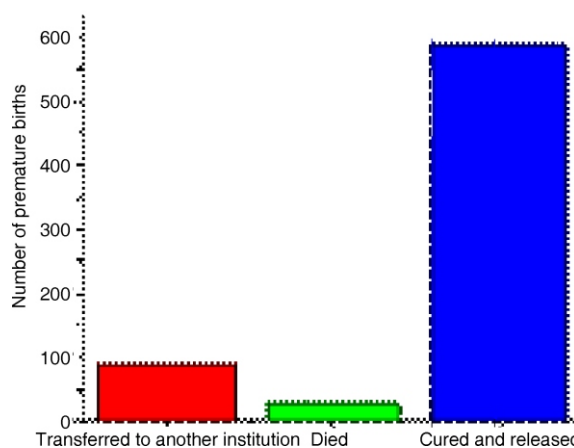

Figure 6. Number of premature births with different outcomes – transferred to another institution, fatal and treated at the maternity hospital and released home
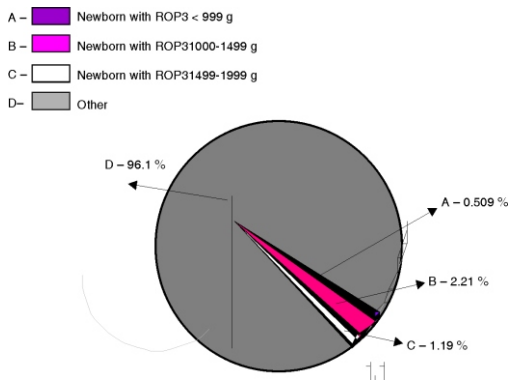
96

M. M. Živanović, et al.: Influence of Electromagnetic and Nuclear Radiation ...
Nuclear Technology & Radiation Protection: Year 2017, Vol. 32, No. 1, pp. 91-98

Figure 7. Premature births treated at the maternity hospital and discharged afterwards – percentage of patients' cases according to weight
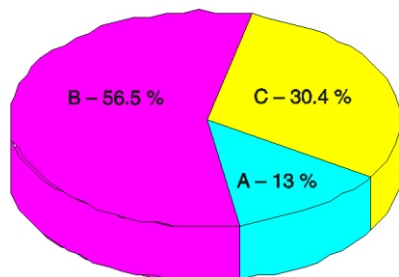

Figure 8. Incidence of ROP with respect to body weight (2004)

Table 3 and fig. 9 represent the cases of ROP developed in children who have not been exposed to an elevated concentration of O_2. They contain information on the ROP and sanitation.

Usually, the shortest O_2 therapy lasts 3 days and the maximum lasts 86 days. The average duration of therapy is 23 days.

According to the data analysis, a large number of newborns with ROP has been successfully treated. From the statistical data regarding ROP, the largest number of detected ROP cases occurred with newborns weighting between 1000 g and 1499 g. In tab. 4 it can be seen that most cases are diagnosed with asphyxia prenatal and RDS. The number of perinatal infections and pneumonia is somewhat smaller. It would be of great interest to collect data and create a database for diagnosis and laser treatment of ROP in Belgrade, Serbia.

CONCLUSIONS

Discussions about the correlation between the oxygen therapy and ROP occurrence are still present. ROP is considered to be a serious disease and here are the results of the study from the IGA KCS Hospital in
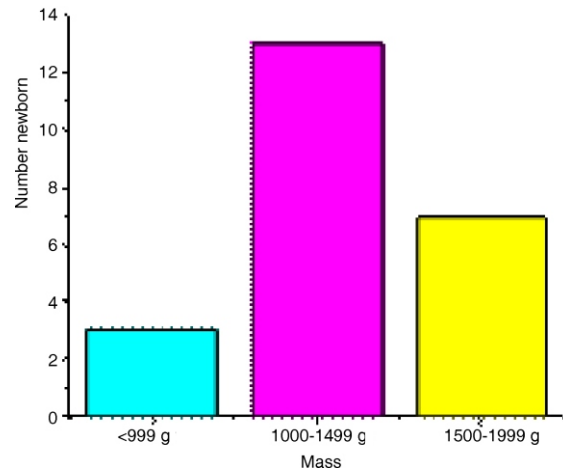

Figure 9. Number of ROP incidence depending on body weight (2004)

Table 4. Pathology and oxygen therapy for children with ROP

Pathology	Number of newborns
Asphyxia prenatal	48 children
RDS	47 children
Perinatal infections: sepsis	32 children
Candida	4 children
Pneumonia	21 children
Haemorrhagia pulm	3 children
BPD	8 children
IVH I and II	41 children
IVH III and IV	13 children
Hydrocephalus post-haem	4 children
Ventriculodilatatio	3 children

Belgrade, Serbia. One of the methods for ROP treatment are laser techniques (semiconductor lasers are also favourable).

Besides the ROP treatment, there are other laser applications in gynaecology, neonatology and ophthalmology. One of the very important applications is the analysis of milk quality for newborns. There are different methods to control the quality of milk through the measurement of turbidity (He Ne laser or with Nd^{3+}:YAG and its harmonics in the ps-region). Measurements of turbidity belong to the category of reliable, but not highly accurate. Adjusted selection with the excitation wavelength and the fluorescence method with pulse lasers, present for a long time is a more precise method for mastitis diagnosis. From the references it could be seen that the distinction could be made in the quality of milk (whether it is pathogenic or healthy). Another application of laser treatment is the rehabilitation of the mastitis affected tissue.

AUTHORS' CONTRIBUTIONS

The idea and results for the presented research were initiated and performed by M. Živković at the IG

M. M. Živanović, *et al.*: Influence of Electromagnetic and Nuclear Radiation ...
Nuclear Technology & Radiation Protection: Year 2017, Vol. 32, No. 1, pp. 91-98

97

KCS Hospital. The data processing and graphic presentation *i. e.* manuscript preparation were carried out by M. Ž. Srećković, T. M. Stojić, and B. M. Bokić. The manuscript was written by M. Živković and M. Ž. Srećković and all the authors participated in the discussion of the results presented in the final version of the paper.

REFERENCES

[1]   ***, Advanced Signal Processing Handbook, Theory and Implementation for Radar, Sonar and Medical Imaging Real-Time Systems (Ed. S. Stergiopoulos), CRC Press, Boca Raton, Fla., USA, 2001

[2]   Marjanović, N., *et al.*, Simulated Exposure of Titanium Dioxide Memristors to Ions Beams, *Nucl Technol Radiat, 25* (2010), 2, pp. 120-125

[3]   ***, LESON Learned from Accidents in Industrial Irradiation, IAEAQ, Vienna, 1996

[4]   Sliney, D. H., Wolbarsht, M. I., Safety with Lasers and Other Optical Sources, Plenum Press, New York, 1980

[5]   Chadwick, K. H., Leenhouts, H. P., The Molecular Theory of Radiation Biology, Springer, Berlin, 1961

[6]   Biological Effects of Low-Level Radiation, International Atomic Energy Agency, Vienna, 1983

[7]   Srećković, M., *et al.*, Laser in Medicine (in Serbian), Institute of Physics for Technical Faculties, Belgrade, 2010

[8]   Obaturov, G. M., Biophysical Models of Radiobiological Effects (in Russian), Moskva, Energoatom, 1987

[9]   Ullmaier, H., Schilling, W., Radiation Damage in Metallic Reactor Materials, pp. 301-in Physics of Modern Materials, Vol. 1, International Atomic Energy Agency, Vienna, 1980

[10]   Stanković, K., *et al.*, Influence of Tube Volume on Measurement Uncertainty of GM Counters, *Nucl Technol Radiat, 25* (2010),1, pp. 46-50

[11]   Overbeek, F., *et al.*, Carcinogenic Risk in Diagnostic Nuclear Medicine : Biolo Gical and epidemiological Considerations, *Eur. J. of Nucl. Med., 21* (1994), 9, pp. 997-1012

[12]   Srećković, M., *et al.*, Laser Influence and Application to Biosystems, Organisms and Cells, Lasers 2001, Proc. Lasers 2001, Mc Lean, SoQue, STS Press, 2002, pp. 323-330

[13]   Srećković, M., *et al.*, Photoinduced Processes, Radiation Interaction with Material and Damages – Material Hardness, *Nucl Technol Radiat, 30* (2015), 1, pp. 23-34

[14]   Praskalo, Ž., *et al.*, A Survey of Short-Term and Long-Term Stability of Tube Parameters in a Mammography Unit, *Nucl Technol Radiat, 29* (2014), 4, pp. 321-325

[15]   Dolićanin, Ć. B., *et al.*, Statistical Treatment of Nuclear Counting Results, *Nucl Technol Radiat, 26* (2011), 2, pp. 164-170

[16]   Djekić, S., *et al.*, Conditions of the Applicability of the Geometrical Similarity Law to Impulse Breakdown in Gases, *IEEE Trans. on Dielectrics and Electric Insulation, 17* (2010), 4, 10.1109/tdei.2010. 5539689

[17]   Vujisić, M., *et al.*, A Statistical Analysis of Measurement Results Obtained from Nonlinear Physical Laws, *Appl. Matemat. Modelling, 35* (2011) , July, pp. 3128-3135

[18]   Bowmaker, J. K., Dartnall, H. J. A., Visual Pigments of Rods and Cones in a Human Retina, *J. Physiol., 298* (1980), pp. 501-511

[19]   Naseri, A., Patel, N. P., Vision Loss as a Complication of Gamma Knife Radio Surgery for Trigeminal Neuralgia, *Br. J. Ophthalmol. 88* (2004), 9, pp. 1225-1226

[20]   Dunjić, Z. B., Infection and Risk Factors for retinopathy Prematurity; Incidenca ROP in IGA KCS, 2006

[21]   Živković, M., Longitudinal Follow Up of Growth and Development of Children from Most Severe Cases of RH(D) Alloimmune Pregnancies After Application of intrauterine Intravascular Transfusion, Ph.D. Thesis, Faculty of Medicine, University of Belgrade, 2012

[22]   Oros, A., Premature Retinopathy (in Serbian), Andrejević Foundatin, Belgrade, 2003

[23]   Abramson, D. H., Schefler, A. C., Transpupillary Thermotherapy as Initial Treatment for Small Intraocular Retinoblastoma, Technique and Predict of Success, *Ophtalmology, 111* (2004), 5, pp. 984-991

[24]   Langston, D. H., Manual of Ocular Diagnosis and Therapy, Ed. Boston, Littel, Brown and Comp., 1996, pp. 159-167

[25]   ***, Conference, Premature Retinopathy and Blindness Preservation at Neonatal Born, 2007

[26]   Harley, R. D., *et al.*, Eds. Harley's Paediatric Ophthalmology, Lippincourt, Wiliams and Ewilkins, Md., 2005

[27]   Fankhauser, F., Kawasniewska, S., Laser in Ophthalmology, Eds. Kugler, The Hague, 2003

[28]   Biglan, A. W., *et al.*, Retinopathy of Prematurity, Amsterdam, Ugler, 1995

[29]   Lorenz, B., Moore, A. T., Paediatric Ophthalmology, Neuro-Ophthalmology, Genetics, Berlin, Springer, 2006

[30]   ***, Cryotherapy for Retinopathy of Prematurity Cooperative Group, Multicenter Trial of Cryotherapy for Retinopathy of Prematurity Preliminary Results, *Arch Ophthalmol, 106* (1988), 4, pp. 471-479

98

M. M. Živanović, *et al.*: Influence of Electromagnetic and Nuclear Radiation ...
Nuclear Technology & Radiation Protection: Year 2017, Vol. 32, No. 1, pp. 91-98

**Моника М. ЖИВКОВИЋ, Милеса Ж. СРЕЋКОВИЋ,
Томислав М. СТОЈИЋ, Бојана М. БОКИЋ**

УТИЦАЈ ЕЛЕКТРОМАГНЕТНОГ И НУКЛЕАРНОГ ЗРАЧЕЊА У МЕДИЦИНИ ЗА ТЕРАПИЈУ И ДИЈАГНОЗУ – ПРОЦЕСИ, ЧИЊЕНИЦЕ И СТАТИСТИЧКА АНАЛИЗА

Савремена медицина (биомедицина) не може да се замисли без дијагностике и терапеутских метода базираних на нуклеарној, ласерској, акустичкој техници и процесима заснованим на њима. Примена ових метода је везана са рачунарском подршком, обрадом сигнала, мерним-контролним техникама, високим степеном аутоматизације и анализом слике. У раду се анализирају савремени проблеми техничке природе који се односе на неонатологију и офталмологију, а заснивају се на дејству нуклеарног зрачења и ласерских снопова. Овде су представљене статистичке обраде резултата из Института за гинекологију и акушерство Клиничког центра Србије, Београд, у вези побољшања вида новорођенчади пренаталног типа са различитим степенима патолошког стања ретинопатије. Упркос добрим резултатима, закључује се да је мултидисциплинарни приступ потребан за боље разумевање улоге ласера и ласерских техника у медицини, као и могућности спрезања. Размотрене су и нове потенцијалне примене ласера од интереса за неонатологију и офталмологију.

Кључне речи: ретинопатија код новорођенчади, неонатологија, ласер, нуклеарно зрачење, оштећење, дозиметрија

Airy beams propagation in optically induced photonic lattices

Bojana Bokić*[a], Falko Diebel[b], Dejan Timotijević[a], Aleksandra Piper[a], Martin Boguslawski[b],
Dragana Jović[a] and Cornelia Denz[b]

[a]Institute of Physics, University of Belgrade, P.O. Box 68, 11001 Belgrade, Serbia;
[b]Institut für Angewandte Physik and Center for Nonlinear Science (CeNoS), Westfälische Wilhelms-Universität Münster, 48149 Münster, Germany

Abstract

We show both experimentally and numerically, control over the acceleration of two-dimensional Airy beam propagating in optically induced photonic lattice. Varying the lattice strength and including various defects we can reach a state, where the acceleration is completely stopped. We find an additional class of discrete lattice beams, localized and defect modes observed with Airy beams propagating in diamond optically induced photonic lattice.

Keywords: accelerating beams, photonic lattices, defects

1. INTRODUCTION

Airy beams are a well-known type of accelerating optical beams [1]. Unlike ordinary optical wave fields, Airy beams show an accelerated transverse intensity distribution which remains invariant along their parabolic trajectories [2]. Originally, Airy beams were introduced as wave functions solving the one-dimensional Schrödinger equation for free particles. Due to the equivalence between the Schrödinger equation in quantum mechanics and the paraxial equation of diffraction in optics these concepts can be transferred to optics. The ballistic-like properties of Airy beams qualify them for various applications ranging from particle trapping along curved paths [3] and self-bending plasma channels [4] to ultrafast self-accelerating pulses [5] and Airy light bullets accelerating in both transverse dimensions and in time [6]. Over the years, two-dimensional Airy beams have been systematically investigated, particularly in the field of optics and atom physics. In terms of experimental realization, optics provides a fertile ground to directly observe and study the properties of such non-spreading waves in detail. One of the features of these beams is their potential for applications in nonlinear optics: nonlinear interaction of light with some material and a study of accelerating beam dynamics inside nonlinear media. Formation of accelerating self-trapped optical beams has been proposed employing the different self-focusing nonlinearities, ranging from Kerr to quadratic nonlinearities, and also using an optically induced refractive-index potential [7, 8].

The key for the realization of all-optical guiding and switching architectures is control of the propagating light with light itself. Propagation dynamics of light is dramatically changed with the presence of photonic lattice. Recently, defect guiding Airy beams in optically induced waveguide arrays is studied [9]. The propagation of such accelerated beams inside a two-dimensional optically induced photonic lattice has not been observed yet.

We analyze theoretically and experimentally how an optically induced photonic lattice affects and modifies acceleration of Airy beams. Various conditions for the propagation and preservation of the Airy beam shape are considered. The acceleration of Airy beams is controlled by varying the lattice strength (refractive index modulation) and by introducing positive and negative single-side defects. We find that a modification of refractive index modulation leads to reduced Airy beam acceleration and formation of discrete lattice beams. However, inclusion of lattice defects changes the beam dynamics completely: with the negative defect Airy beams experience a strong repulsion, while in the presence of positive defect they form localized defect modes.

*bojana@ipb.ac.rs; phone +381 11 3713161; fax +381 113162190

2. THEORETICAL BACKGROUND AND EXPERIMENT

To study the propagation behavior of Airy beams in optical systems with induced photonic lattice, we start with considering the following scaled paraxial equation of diffraction for electric field Ψ

$$i\partial_\zeta \Psi + \frac{1}{2}(\partial_\chi^2 \Psi + \partial_\nu^2 \Psi) + \frac{1}{2}k_0^2 w_0^2 \Delta n^2 (I_{indu})\Psi = 0 \ . \tag{1}$$

Here, $\chi = x/w_0$ and $\nu = y/w_0$ are dimensionless transverse coordinates scaled by the characteristic length w_0. $\zeta = z/kw_0^2$ represents the dimensionless propagation distance with $k = 2\pi n/\lambda$. The photonic lattice enters this equation in terms of an intensity-dependent refractive index modulation Δn^2 (I_{indu}), which represents the optical induction process. This equation is also suitable to cover nonlinear light propagation in the case the inducting intensity becomes a function of field Ψ itself. In this contribution, however, we restrict ourselves to linear effects.

Considering the case for light propagation in homogenous, linear medium, where $\Delta n^2 = 0$ holds, the wave equation (1) can always be separated into two parts, each depending only on one transverse coordinate χ or ν, respectively. Therefore, the solution Ψ is also separated and can be written as a product in the following form: $\Psi(\chi,\nu,\zeta) = \Psi_1(\chi,\zeta)\Psi_2(\nu,\zeta)$. As firstly shown in [1] each part of the wave equation is fulfilled by a non-dispersive Airy solution. Thus, the overall solution of Eq. (1) reads as:

$$\Psi(\chi,\nu,\zeta) = \prod_{X=\{\chi,\nu\}} Ai(X - (\zeta/2)^2)\exp(i(X\zeta/2) - i(\zeta^3/12)) \ . \tag{2}$$

We have to consider truncated solution with finite extent and energy, like $\Psi_\chi(\chi,0) = Ai(\chi)\exp(a_\chi\chi)$, with the positive decay length a_χ, typically $a_\chi \ll 1$. It has been shown, that this kind of solution still solves the wave equation [1] and the distinguished properties of Airy beams are preserved. Although, the transverse intensity pattern is now non-spreading over a limited propagation distance, this easily covers the longitudinal range necessary to observe sufficient transverse displacement of the truncated Airy beams.

Our experimental setup for all measurements is sketched in Fig. 1(a). We use the beam from frequency-doubled, continuous wave laser (Nd:YVO$_4$) emitting at λ = 532 nm. The beam is split into two partial beams, each illuminating a high-resolution, programmable, phase-only spatial light modulator (SLM1, SLM2). The first one (SLM1), in combination with two lens and Fourier mask, is employed for making of nondiffracting induction beam. By using the calculated phase patterns, addressed to spatial light modulators, we modulate the phase and amplitude of incident plane wave and thereby obtain the complex field of desired nondiffracting induction beam. This modulated beam is then sent through the 20 mm long Sr$_{0.60}$Ba$_{0.40}$Nb$_2$O$_6$ (SBN:Ce) photorefractive crystal, externally biased with $E_{ext} \approx 2000$ V/cm, an electric dc field. The induction beam is set to be ordinarily polarized with respect to the crystal's optical axis, to minimize the feedback of the written refractive index structure onto the induction beam itself. Because of the high polarization anisotropy of electro-optic coefficients of SBN:Ce crystal we are able to induce sufficient refractive index modulations to affect the propagation of extraordinarily polarized Airy beam. The Airy beam is made the same way as the nondiffracting induction beam by means of the second modulator (SLM2) and the encoded complex field, calculated in real space with the Eq. (2). To accurately overlay two beams in the crystal, we place a beam splitter directly in front of the SBN crystal. In addition, by illuminating the crystal homogeneously with white light, we can erase modulations of the written refractive index. With an imaging lens and a camera, mounted on a translation stage, we record the intensity distribution in different transverse planes.

The propagation characteristics of 2D Airy beam propagating in a homogeneous medium are shown experimentally in Fig. 1. The intensity distributions at the front and back face of the SBN:Ce crystal are shown in Fig. 1(b) and 1(c), respectively. To experimentally realize the photonic lattice which should control the propagation trajectory of Airy beam we use the technique of optical induction [10, 11]. Figure 1(d) shows the recorded intensity distribution of experimentally realized nondiffracting beam used to optically induce a two-dimensional square lattice. The lattice period $\Lambda = \pi/k_t \approx 25\mu m$ is chosen to match exactly the distance between the main and the first neighboring lobes of Airy beam.
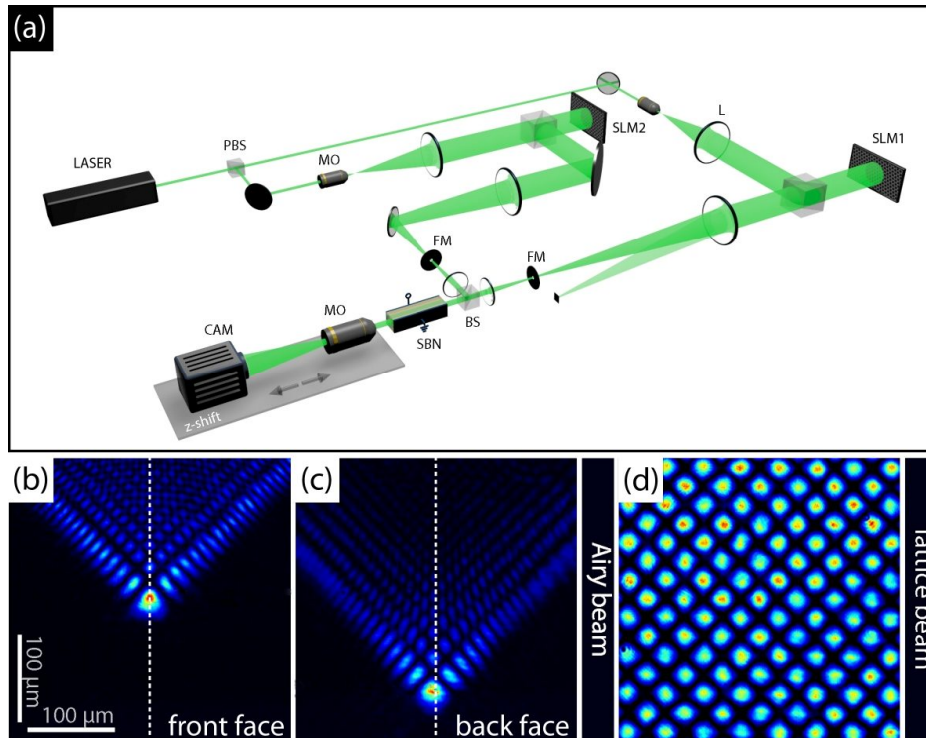
Figure 1. Experimental realization of two-dimensional Airy beams and photonic lattices. (a) Experimental setup. LASER: Nd:YVO$_4$ at λ = 532 nm, (P)BS: (polarizing) beam splitter, FM: Fourier mask, L: lens, MO: microscope objective, SBN: strontium barium niobate crystal, SLM1, SLM2: spatial light modulators. (b) Experimentally recorded intensity distribution of the Airy beam at the front face and (c) intensity distribution at the back face. (d) Lattice intensity distribution of the induced refractive index modulation.

We support our experiments with comprehensive numerical simulations by solving the paraxial wave equation (1), which models the light propagation in media with inhomogeneous refractive index modulations. The process of optical induction into a photorefractive material like SBN is represented by $\Delta n^2(I_{indu})$, which can be calculated in the full anisotropic model with a relaxation method. Since only linear effects are considered, the inducing intensity I_{indu} is solely given by the intensity of nondiffracting beam, $I_{indu}=|E_{ndB}|^2$ (cf. Eq. (3)). Even though the paraxial wave equation stays in the linear regime, it is not solvable analytically and we need to rely on proven beam propagation methods. The propagation equation (1) is solved numerically, using a split-step Fourier method described earlier in [12, 13].

3. CONTROL OF AIRY BEAM SELF-ACCELERATION WITH PHOTONIC LATTICES

Here, we observe the way that optically induced photonic lattice affects the acceleration of two-dimensional Airy beams. We have the self-bending of Airy beams on one side and the waveguiding and discrete diffraction effects of the photonic lattice on the other. By increasing the modulation of refractive index we affect the beam's acceleration and by increasing the lattice strength we affect the slowing down of the beam until we make it stops for a certain value.

In our investigation of propagation behavior of two-dimensional Airy beams in a regular photonic lattice, we are observing the influence of defect lattices as well. We consider single-site defect lattices with positive and negative variable defect strength.

Defect lattices are realized using the nondiffracting zero-order Bessel beam. We are increasing or decreasing the modulation of refractive index thus making a different defect lattices. We use the effective intensity distribution of incoherent superposition of two nondiffracting beams, the lattice beam and the Bessel beam, and make two-dimensional

defect lattice. Since we have incoherent superposition of the two nondiffracting beams we don't need to take care about the phase relation between them and potential unwanted intensity modulation in longitudinal direction. As shown earlier, this multiplexing method is suitable for fabrication of a whole set of different two-dimensional super and defect lattices, including negative defects [14]. For the realization of negative defect we apply the electric dc field, anti-parallel to the optical c-axis and obtain defocusing nonlinearity at the site where the Bessel beam is set to propagate.

Figure 2 illustrates the basic scheme of defect realization. The regular lattice is made by the intensity distribution shown in Fig. 2(a). Afterwards, the Bessel beam (Fig. 2(b)), illuminates the crystal and depending on the direction of applied electric field, the refractive index at one particular site gets increased or decreased. The resulting effective intensity distributions for the positive and negative defect lattices are shown in Fig. 2(c) and Fig. 2(d), respectively. Figures 2(e) and 2(f) show the numerically calculated refractive modulations for both defect lattices.
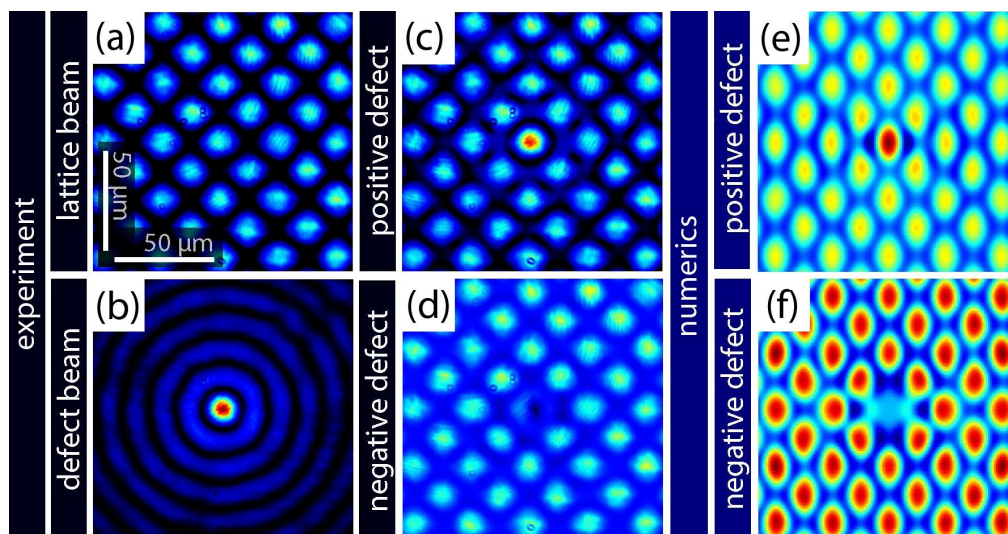

Figure 2. Defect generation in optically induced photonic lattice. (a) Experimental realization of the diamond lattice, (b) the Bessel beam, (c) the positive defect lattice and (d) the negative defect lattice. (e) Numerical realization of the positive and (f) negative lattice defects.

Figure 3 summarizes our numerical results regarding the propagation of Airy beam in regular photonic lattice as well as positive and negative defects. To get a more detailed insight into this propagation dynamics, we monitor the ratio between the power guided in the central waveguide and the total power of Airy beam as a function of the lattice strength and propagation distance. The numerical results for this power ratio are shown in Fig. 2(a) for a regular lattice, (d) negative defect and (g) positive defect. These graphs clearly demonstrates the impact of optically induced photonic lattice and apropriate defects on the formation of discrete structures, as well as suppression of the acceleration and bending of Airy beam. The Airy beam is launched into the induced photonic lattice with the main lobe exactly located at one lattice site. As the refractive index modulation strength grows, the interaction of Airy beam with lattice sites becomes stronger and consequently the bending of Airy beam is decreased. In the case of regular lattice, for higher refractive index modulations Δn, one can observe the localization of beam power to central waveguide at the back face of crystal. Our results clearly show the slowing down of the self-acceleration of Airy beam (Fig. 3(b),(c)). The corresponding intensity profiles at the back face are indicated with the letters at the respective positions. Depending on the different lattice strengths various kinds of discrete structures arises until the lattice finally suppress the acceleration of Airy beam. Most of the energy then stays in the lattice site, where the main lobe of Airy beam was initially launched.

Then we keep all parameters, but change the refractive index modulation Δn to both, positive and negative defects. The Airy beam is positioned with the main lobe exactly located at the defect site. For the different defects we record the intensity profiles of propagated Airy beam at the back face and monitor the percentage of power guided in the central waveguide, as described previously. Figures 3(d) and 3(g) show the numerical results of power ratio for the negative and

positive defect as a function of the propagation distance and refractive index modulation. The negative defect (Fig. 3(d)) significantly reduces the power guided in defect site and finally repels nearly all power, while the positive defect (Fig. 3(g)) strongly enhances the slowing-down and localization process of Airy beam. Corresponding intensity profiles are shown in the right panel of Fig. 3 for two values of Δn for the negative (e), (f) and positive defect (h), (i).
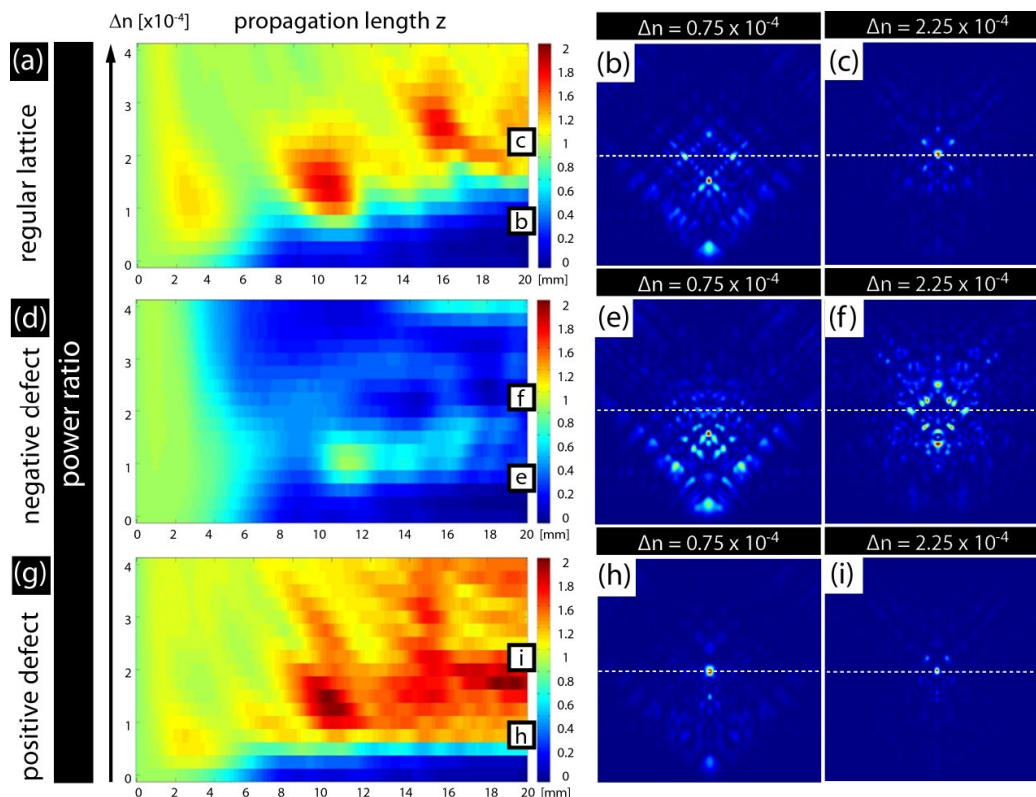

Figure 3. Airy beam propagation in diamond lattice, with and without defects. Dependence of the percentage of Airy beam power in the incident waveguide on refractive index change Δn and propagation length z for a (a) regular lattice, (d) negative defect and (g) positive defect. Numerical results for intensity distributions at the back face for different refractive index change Δn for: (b), (c) regular lattice, (e), (f) negative defect and (h), (i) positive defect.

To experimentally control the index modulation depth we take advantage of the time-dependent build up of induced lattice, which grows monotonously with the writing time. Because in experiments is not possible to record the intensity pattern inside the crystal, we are restricted to the profiles at the back face. In Fig. 4(d) the experimentally measured power ratio at the back face is plotted as a function of the refractive index modulation and defect strength. Therefore, we have repeated the experiments for 11 different defect strengths $S_d = -1 \ldots 1$ and recorded the intensity profile at the back face. The modulus of defect strength S_d is given by the ratio of peak intensities of the discrete and the Bessel nondiffracting beam, while the sign is determined by the direction of applied electric field. These results illustrate the strong dependency of propagation and acceleration properties of Airy beam on the lattice depths, as well as the defect strength. The first and third row contains the experimental results – intensity distributions at the back face for two different values of Δn. The corresponding intensity profiles at the back face are indicated with the letters at the respective positions on graph, and presented in: (a), (e) for negative defect, (b), (f) regular lattice and (c), (g) positive defect. The experimental results fully agree with the theoretical analysis. Comparing the numerical intensity distributions of Airy beam at the back phase (Fig. 3) with corresponding experimental results (Fig. 4), one can see a very good qualitative agreement. Also, comparing the numerical graphs for percentage of Airy beam in incident waveguide for propagation distance of 20 mm with experimental graph in Fig. 4(d), very good agreement is observed for defect strength -1, 0 and +1, which corresponds to negative defect, regular lattice and positive defect, respectively.
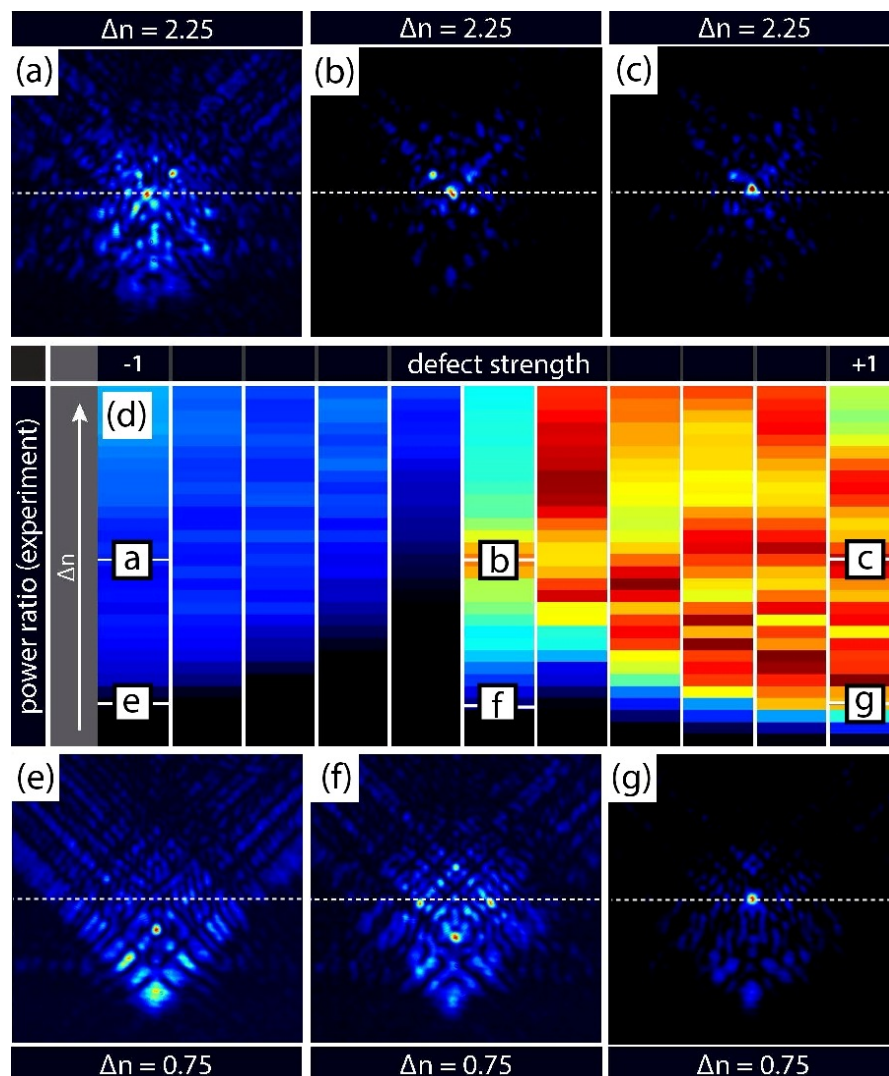
Figure 4. Experimentally observed Airy beam propagation in photonic lattice. (d) Percentage of the Airy beam power propagating in incident waveguide or defect site as a function of refractive index change Δn and defect strength. Exemplary experimental results of Airy beam intensity distribution at the back face for negative defect (a),(e), regular lattice (b),(f) and positive defect(c),(g).

4. CONCLUSIONS

In summary, we have shown, both theoretically and experimentally, that the propagation dynamics of two-dimensional Airy beams could be controlled by optically induced photonic lattices. We demonstrated a way to change the trajectory and shape of finite optical Airy beams. The results depend on the depth of the induced lattice which changes the acceleration and bending of Airy beam. The beam acceleration is slowed down and finally completely stopped for a certain amount of index modulation. Moreover, various single-side defects further affect the beam dynamics as well. By changing the defect strength, as well as the defect type, we can either increase the localization for positive defects, or repel all the power from a defect site, for the negative case. All our presented experimental results fully agree with the supporting numerical simulations.

Acknowledgements

References

[1] Siviloglou, G. A., Broky, J., Dogariu, A. and Christodoulides, D. N.,"Observation of accelerating Airy beams," Phys. Rev. Lett. 99, 213901 (2007).

[2] Siviloglou, G. A., Broky, J., Dogariu, A. and Christodoulides, D. N., "Self-healing properties of optical Airy beams,"Opt. Lett. 33, 207 (2008).

[3] Baumgartl, J., Mazilu, M. and Dholakia, K., „Optically mediated particle clearing using Airy wavepackets," Nat. Photonics 2, 675–678 (2008).

[4] Polynkin, P., Kolesik, M., Moloney, J. V., Siviloglou, G. A. and Christodoulides, D. N.,"Curved plasma channel generation using ultraintense Airy beams,"Science 324, 229–232 (2009).

[5] Chong, A., Renninger, W. H., Christodoulides, D. N. and Wise, F. W.,"Airy–Bessel wave packets as versatile linear light bullets," Nat. Photonics 4, 103–106 (2010).

[6] Abdollahpour, D., Suntsov, S., Papazoglou, D. G. and Tzortzakis, S.,"Spatiotemporal Airy light bullets in the linear and nonlinear regimes," Phys. Rev. Lett. 105, 253901 (2010).

[7] Kaminer, I., Segev, M., and Christodoulides, D. N.,"Self-accelerating self-trapped optical beams," Phys. Rev. Lett. 106, 213903 (2011).

[8] Ye, Z., Liu, S., Lou, C., Zhang, P., Hu, Y., Song, D., Zhao, J. and Chen, Z., "Acceleration control of Airy beams with optically induced refractive-index gradient," Opt. Lett. 36, 3230 (2011).

[9] Lučić, N. M., Bokić, B. M., Grujić, D. Ž., Pantelić, D. V., Jelenković, B. M., Piper, A., Jović, D. M. and Timotijević, D. V., "Defect-guided Airy beams in optically induced waveguide arrays," Physical Review A 88, 063815(2013).

[10] Terhalle, B., Desyatnikov, A. S., Bersch, C., Träger, D., Tang, L., Imbrock, J., Kivshar, Y. S. and Denz, C., "Anisotropic photonic lattices and discrete solitons in photorefractive media," Applied Physics B 86, 399–405 (2006).

[11] Rose, P., Boguslawski, M. and Denz, C., "Nonlinear lattice structures based on families of complex nondiffracting beams," New Journal of Physics 14, 033018 (2012).

[12] Belić, M. R., Leonardy, J., Timotijević, D. and Kaiser, F., "Spatiotemporal effects in double phase conjugation," Journal of the Optical Society of America B 12, 1602 (1995).

[13] Belić, M., Petrović, M., Jović, D., Strinić, A., Arsenović, D., Motzek, K., Kaiser, F., Jander, P., Denz,C., Tlidi, M. and Mandel, P., "Transverse modulational instabilities of counterpropagating solitons in photorefractive crystals," Optics express 12, 708–16 (2004).

[14] Boguslawski, M., Kelberer, A., Rose, P. and Denz, C., "Multiplexing complex two-dimensional photonic superlattices," Optics Express 20, 27331–43 (2012).

Универзитет у Београду
Електротехнички факултет
Број: 17112
Датум: 25.10.2008.

На молбу коју је поднела **Бојана (Миле) Бокић**, а на основу члана 161 Закона о општем управном поступку (Службени лист СРЈ бр. 33/97, 31/01), Електротехнички факултет Универзитета у Београду издаје

УВЕРЕЊЕ

Бојана (Миле) Бокић, рођена 05.07.1981. године, Београд, општина Савски венац, уписана школске 2000/01 у 1. годину, дипломирала је 24.10.2008. (општи успех 7.94, на дипломском испиту 10) Одсек за физичку електронику - смер Наноелектроника, оптоелектроника и ласерска техника Електротехничког факултета и стекла звање дипломираног инжењера електротехнике.

Диплома ће носити број овог уверења.

Уверење се издаје без наплате таксе на основу члана 19 тачка 7 Закона о административним таксама (Службени гласник РС бр. 43/03, 51/03).

Декан
Електротехничког факултета

Проф. др Миодраг Поповић

Универзитет у Београду
Електротехнички факултет
Број индекса: 2008/3173
Број: M20090218
Датум: 01.10.2010.

На основу члана 161 Закона о општем управном поступку ("Службени лист СРЈ", бр. 33/97, 31/2001 и "Службени гласник РС", бр. 30/2010), дозволе за рад број 612-00-588/2008-04 од 17.11.2008. године коју је издало Министарство просвете Републике Србије и службене евиденције, Универзитет у Београду – Електротехнички факултет издаје

УВЕРЕЊЕ

Бојана Бокић

име једног родитеља Миле, ЈМБГ 0507981715109, рођена 05.07.1981. године, Београд, општина Савски Венац, Република Србија, уписана школске 2008/09. године, дана 30.09.2010. године завршила је мастер академске студије на студијском програму Дипломске академске студије Електротехника и рачунарство - модул Биомедицински и еколошки инжењеринг, у трајању од једне године, обима 60 (шездесет) ЕСПБ бодова, са просечном оценом 9,86 (девет и 86/ 100).

На основу наведеног издаје се ово уверење о стеченом високом образовању и академском називу *мастер* на дипломским академским студијама из области Електротехничко и рачунарско инжењерство.

Пун стручни назив који је именована стекла утврдиће Национални савет за високо образовање у року од три месеца од дана ступања на снагу Закона о изменама и допунама Закона о високом образовању ("Службени гласник РС" бр. 44/2010) усклађивањем Правилника о Листи стручних, академских и научних назива ("Службени гласник РС" бр. 30/07,112/08 и 72/09) са овим Законом.

Декан

Проф. др Миодраг Поповић

Преглед научне активности

Бојана Бокић је била ангажована на испитивањима интеракције фемтосекундног ласерског зрачења са материјалима различитог порекла. Фемтосекундни импулс у неким аспектима фундаментално мења механизам интеракције ласера и материјала у поређењу са ласерима дужег импулса. Развој фемтосекундних ласера отворио је читав низ поља за научна истраживања. Већина истраживања се ослања на три јединствене карактеристике ултракратких ласерских импулса: 1) кратак ласерски импулс се може користити за мерење веома брзих процеса; 2) кратак импулс може створити веома неравнотежна стања; 3) фемтосекундни импулси имају веома велики интензитет електричног поља па су нелинеарни ефекти веома изражени.

Била је ангажована и на истраживањима фотонских структура биолошког порекла. Испитивана је спектрална и просторна селективност нанометарских структура на површини крила лептира *Apatura ilia* и *Apatura iris*. Показано је да крило веома интензивно рефлектује светлост у уском спектралном и угаоном интервалу, што даје еволутивну предност овим инсектима. Осим тога, специфичност нанометарских структура на крилу лептира даје путоказ за реализацију спектрално и угаоно селективних филтера. Ово истраживање је разултирало радом који је објављен у водећем међународном часопису.

Бојана Бокић је у оквиру пројекта ОИ 171038 ангажована на експерименту испитивања ефеката фемтосекундног ласерског снопа, таласне дужине из ултраљубичастог дела спектра и фреквенције 76 MHz, на два типа танких филмова на супстрату силицијума – једнослојном танком филму алуминијума, и вишеслојном танком филму који се састоји од пет алуминијум/титанијум бислојева (укупне дебљине 130 nm). Модификација површина мета је урађена сноповима ниских флуенци и различитим временима озрачавања, не прелазећи време од 300 s. Формиране су периодичне површинске наноструктуре, периода око 315 nm и висине 45 nm. Ови експериментални резултати су објављени у водећем међународном часопису.

Бојана Бокић је ангажована и на билатералном пројекту са Немачком, под називом „Пропагација и локализација светлости у системима са комплексним фотоничним решеткама “. У протеклој години радила је на експерименту са Еири зрацима у фотоничним структурама са различитим дефектима као и линеарној и нелинеарној интеракцији више Еири зрака у кристалу стронцијум баријум ниобата.

Главни циљ пројекта био је изучавање пропагације и локализације светлости у фоторефрактивним срединама, и стварања директне везе са процесом процесуирања информација. У Немачкој су експериментално потврђени резултати линеарне и нелинеарне интеракције дводимензионалних Еири снопова, који су претходно добијени теоријски и нумеричким симулацијама у Београду. Испитивана је кохерентна и некохерентна суперпозиција два и четири дводимензионална Еири снопа, када су у фази као и када су у различитим фазама. За разлику од линеарне суперпозиције, нелинеарна интеракција је показала формирање структура налик солитонима, формирање једног „солитона“ када су снопови у фази и формирање два „солитона“ када су снопови у различитим фазама. Након добијених експерименталних резултата, и њиховог поређења са нумеричким резултатима, уследила је обрада резултата као и припрема за публиковање. Написан је научни рад и послат у часопис међународног значаја са веома високим импакт фактором. Током овог пројекта објављена су 3 рада у водећим међународним часописима и два саопштења са међународних скупова.

На основу члана 94. Закона о раду, доносим

Р Е Ш Е Њ Е

о породиљском одсуству

1. Запосленој **Бојани Бокић**, истраживачу сараднику у Институту за физику, отпочело је породиљско одсуство дана **31.01.2015**. године.

2. Породиљско одсуство запосленој одобрава се на основу налаза Дома здравља и трајаће до навршених три месеца од дана порођаја.

3. За време породиљског одсуства запослена има право на накнаду зараде, у складу са законом.

О б р а з л о ж е њ е

Запослена Бојана Бокић ушла је у обавезни заштитни период материнства у трајању од 28 дана пре порођаја почев од 31.01.2015. године, што произилази из налаза надлежног здравственог органа по коме се порођај може очекивати за 28 дана.

За време трајања породиљског одсуства запослена ће имати накнаду зараде утврђену законом.

Директор Института за физику

др Александар Богојевић

На основу члана 94. Закона о раду, доносим

Р Е Ш Е Њ Е

о одсуству са рада ради неге детета

1. Запосленој Бојани Бокић, истраживачу сараднику у Институту за физику, отпочиње одсуство ради неге детета дана **26.05.2015.** године.

2. Одсуство ради неге детета запосленој одобрава се на основу налаза Дома здравља и трајаће до **30.01.2016.** године.

3. За време одсуства ради неге детета запослена има право на накнаду зараде, у складу са законом.

О б р а з л о ж е њ е

Запослена Бојана Бокић по истеку породиљског одсуства, подноси захтев за коришћење одсуства ради неге детета до истека 365 дана од дана отпочињања породиљског одсуства што се овим решењем одобрава.

За време трајања одсуства ради неге детета запослена ће имати накнаду зараде утврђену законом.

Директор Института за физику

др Александар Богојевић